

Thermal modeling of an alkaline electrolyser under variable load

by

Kristian Mera

to obtain the degree of Master of Science at the Delft University of Technology, to be defended publicly on Thursday September 22, 2022 at 03:00 PM.

Student number: 5200539

Project duration: January 1, 2022 – September 22, 2022

Thesis committee: Dr. Ir. Mahinder Ramdin, TU Delft, supervisor

Prof. Dr. Ir. Thijs J. H. Vlugt, TU Delft, supervisor

Dr. Ir. Willem Haverkort TU Delft

Dr. Ahmadreza Rahbari XINTC Global, supervisor

This thesis is confidential and cannot be made public until September 31, 2024.

An electronic version of this thesis is available at http://repository.tudelft.nl/.



Summary

The unprecedented increase in mean ambient temperature due to immoderate CO_2 emissions has shifted the energy policy towards the replacement of fossil fuels with renewable energy sources. Nevertheless, the intermittency of these technologies renders them unsuitable for reliable energy supply. A prominent solution is the utilization of renewable energy to produce green hydrogen that can be stored for later use.

The most environmental-friendly viable method for green hydrogen production is the electrolysis of water. Between the already existing types, alkaline electrolyser is the one with the highest technological maturity and lowest cost of hydrogen production. Despite that, the low energy efficiency, and the energy losses associated with the materials and the geometrical configuration make it difficult to produce hydrogen at competitive prices compared to fossil fuels. The connection with renewables exposes the electrolyser to variable loads that negatively affect the life of materials and the purity of hydrogen since the operating conditions like temperature and current change constantly.

Previous research work, as presented in this report, has shown that the energy losses owing to the electrode kinetics, membrane, and electrolyte resistivity are responsible for higher energy consumption than the thermodynamic minimum. These losses are a strong function of temperature and current density. This research project aims to investigate the performance of the electrolyser under fluctuating working conditions to get an insight into how energy consumption and product purity are affected.

Preface

The exigency of energy production with minimal environmental impact has shifted my interest to prominent technologies with reliable and sustainable operation aspects. For the last ten months, my focus has been on the investigation of hydrogen production with alkaline electrolysis. Thanks to XINTC Global I had the opportunity to discover the world of hydrogen and at the same time contribute to the comprehension and improvement of alkaline electrolysis technology.

Firstly, I would like to express my gratitude to my supervisor Ahmadreza Rahbari from XINTC Global for his immense support during the theoretical investigation of the technology and the execution of the experiments. Secondly, I would like to thank my supervisor from TU Delft Mahinder Ramdin for his support, guidance, and fruitful discussions regarding the technical problems that have arisen. Lastly, special thanks to my supervisor Thijs Vlugt from TU Delft for his recommendations and insights along the course of this work that helped me enrich it and bring it to a high academic level.

The path towards progression and development would not have been realized without the financial and moral support of my parents. Huge gratitude to them!

> Kristian Mera, Delft, September 2022

Contents

Li	st of	Figure	es	vii	
\mathbf{Li}	st of	Table	S	xii	
N	omen	clatur	re	xiii	
1 Shift towards green					
	1.1	Motiv	ation	1	
	1.2	The p	ath to the hydrogen economy	3	
	1.3	XINT	C Global	4	
	1.4	Resear	rch Objectives	5	
2	Elec	trolys	ers - a theoretical analysis	7	
	2.1	Types	of electrolysers	7	
		2.1.1	Alkaline water electrolyser (AWE)	7	
		2.1.2	Proton exchange membrane electrolyser (PEME)	9	
		2.1.3	Solid oxide electrolysis cell (SOEC)	9	
	2.2	Proces	ss flow	10	
	2.3		nodynamics of water electrolysis		
	2.4	Electr	ochemical effects	13	
	2.5	Cell e	nergy losses	15	
		2.5.1	Electrochemical kinetics	15	
		2.5.2	Electrolyte	15	
		2.5.3	Membrane & Electrodes	15	
		2.5.4	Bubbles	16	
		2.5.5	Gas diffusion	16	
		2.5.6	Concentration overvoltage	17	
	2.6	Efficie	ency	17	
	2.7	Polari	zation curves	18	
	2.8	Thern	nal modeling	18	
	2.9	Concl	usions	19	

3	Cell	Mode	eling	21
	3.1	Therm	nodynamic properties	21
		3.1.1	Electrolyte	21
		3.1.2	Reversible potential	23
		3.1.3	Thermoneutral voltage	24
	3.2		ochemical model	25
		3.2.1	Ohmic losses	25
		3.2.2	Activation losses	29
		3.2.3	Efficiency	31
		3.2.4	Molar flow of products	32
	3.3		nal model	33
		3.3.1	Stack	33
		3.3.2	Separators	36
	3.4	Entrop	py balance	38
4	Res	ults		41
-	4.1		imental setup	41
		4.1.1	Pumps and vanes	41
		4.1.2	Sensors	41
		4.1.3	Piping	42
		4.1.4	Gas chromatograph	42
		4.1.5	Gas separators	43
		4.1.6	Stack-Cell	44
	4.2	Polariz	zation curves	45
	4.3	Therm	nal modeling	50
		4.3.1	Theoretical stack performance	50
		4.3.2	Real stack performance	57
_	ъ.			00
5		Caral		66
	5.1	Conclu		66
		5.1.1	Cell level	67
	5.2		nmendations	68
	5.2	necon.	imendations	00
A	pen	dices		70
٨	Stac	·k		70
А	A.1		mass & energy balance	70
	A.1 A.2		entropy balance	72
	A.3		ator mass & energy balance	73
	A.4	_	S	75
	11.7	DOIVEL		10
\mathbf{Bi}	bliog	raphy		76

List of Figures

1.1	in emissions is evident from 1950 and afterward. Data obtained from Refs. [5]	2
1.2	Hydrogen pathways from production to end use. Hydrogen in gas form can be used in many areas like transportation, industry, and domestic consumption while conversion back to electricity is possible through fuel cell technology. Powering the electrolyser with renewable energy leads to hydrogen production with minimal environmental impact. Figure reproduced from Refs. [13].	3
2.1	Illustration of the alkaline electrolysis cell including the anode, cathode, membrane, and the power source. In the cathode, water is split to hydrogen and hydroxides where the later travel through the membrane to the anode to give oxygen and water. Simultaneously, the diaphragm blocks gases from traveling to the other compartment, allowing only OH ⁻ . The power source ensures the electron transfer from the anode to the cathode in order for the reactions to take place. Figure reproduced from Refs. [23].	8
2.2	Process flow diagram of the alkaline electrolyser. The electrolyte is circulated from the separators via pumps and it is cooled with heat exchangers. To avoid concentration gradients, the two streams (anolyte, catholyte) are mixed before being inserted into the stack. The stack outflow is driven back to the separators for the separation of the electrolyte from the gas products that end up in the purification system.	11
2.3	Thermoneutral and reversible voltage as a function of temperature for 35 wt% KOH at ambient pressure. The former increases with temperature due to vapor production and the latter decreases caused by a lower activation energy. The zone above the thermoneutral voltage leads to heat generation while below the reversible voltage no reaction takes place. The area in between is characterized by an endothermic reaction	12
	v	

3.1	Specific conductivity of KOH solution with KOH weight fraction for different temperatures at atmospheric pressure. Specific conductivity is enhanced with temperature and its maximum value is observed for weight fractions between 25% to 35%	22
3.2	Faradaic efficiency of the HYSOLAR-project electrolyser for three different temperatures at ambient pressure. High efficiency is achieved at current densities greater than 50 mA/cm ² . Increasing temperature lowers the faradaic efficiency owing to the gas crossover and the shunt current in the stack that reduce with increasing gas production. Figure reproduced from Refs. [45, 56]	32
3.3	Control volume for the thermal balance. The heat generation inside the stack due to ohmic losses, the heat abduction due to the temperature difference with the environment , and the inflow-outflow of electrolyte and gas products dictate the thermal response of the system	34
3.4	Illustration of the gas separator. The electrolyte-gas mixture coming from the stack, enters the tank to separate into pure electrolyte and gas bubbles. Pure electrolyte recirculates back to the stack while gas is sent to the purification system. Simultaneously, feed water is inserted to replenish the consumed water.	37
4.1	Experimental setup. The power supply unit (PSU) with maximum power of 760 W provides direct current (DC) to the stack. The two impeller-type pumps circulate the electrolyte in the system while the vanes ensure the mixing or separation of the analyte and catholyte. In the oxygen separator tank, analyte is separated from oxygen while in the hydrogen separator tank, catholyte is segregated from hydrogen gas.	42
4.2	Magnetic impeller drive pump. Each pump is 25 W, has a maximum flow rate of 19 L/min, and circulates the anolyte/catholyte from the gas tank to the stack. The pump has a 6.5 cm diameter and 16.5 cm length. \dots	43
4.3	$\rm H_2$ gas separator (left) and $\rm O_2$ gas separator (right). The 32 L $\rm H_2$ gas separator is used for the separation of electrolyte from hydrogen, has a 31 cm diameter, and 40 cm length. Accordingly, the 16 L $\rm O_2$ separator separates the electrolyte from the oxygen, has the same diameter, and its length is 20 cm. Inside the tanks, there are spiral tubes allowing the flow of water in the event of cooling demand.	44
4.4	Single cell with stainless-steel electrode. The bolts are used to fasten the anodic and cathodic chambers. At the bottom plastic tubes, the electrolyte is inserted while at the upper tubes the electrolyte with the product gases leaves the cell. The cell has dimensions of $22~\rm cm~x~19~cm$.	45

4.5	Comparison of polarization curves between experimental data (cell 1) and model for 1 bar and different temperatures. The experimental data are described reasonably well by the model for all the temperatures tested. The non-linear behavior due to the activation losses in low current densities, and the linear one owing to the ohmic losses at high densities are observed in the polarization curves.	47
4.6	Comparison of polarization curves between experimental data (cell 2) and model for 1 bar and different temperatures. The experimental data are simulated by the model with less than 1.9% error for all the temperatures tested. The non-linear behavior due to the activation losses in low current densities, and the linear one owing to the ohmic losses at high densities are distinguished in the graph.	48
4.7	Cell 1 voltage as a function of pressure for various current densities at 50 °C. The reversible voltage increases with pressure while the opposite occurs for the losses due to the bubble presence in the electrolyte and electrode. Consequently, an insignificant increase in cell voltage due to pressure is observed	48
4.8	Effect of the cathodic exchange current density on polarization curve for cell 1 at 50 °C and atmospheric pressure. It is clear that the exchange current density heavily affects the cell voltage. Its enhancement by two or four orders of magnitude leads to 10% and 20% voltage reduction, accordingly. This discrepancy is observed irrespective of the current density applied.	49
4.9	Polarization curves of Stainless Steel and Nickel electrode at 50 °C and 1 bar. Nickel electrode demonstrates superior performance by having 17.7% less voltage compared to SS owing to the higher electrochemical activity. This can be seen in (b) and (c). Simultaneously, in both electrodes, membrane B induces less voltage drop as opposed to membrane A as can be seen in (a) and (d). The voltage difference increases with the current density and reaches a maximum value of 11.7% at 160 mA/cm ² . The explanation lies in the electrolyte repelling pores, the thick material, and the higher tortuosity of membrane A	50
4.10	Contribution of each overpotential term to the total voltage for cell 1 at 50 $^{\circ}$ C and 1 bar. The proportion of the reversible voltage to the total reduces with current since its value is constant. Concerning the overvoltages, the activation losses have the highest contribution compared to the ohmic ones in the current density range displayed. Nonetheless, the ohmic losses grow linearly with current where at 10 mA/cm² is almost 0% while at 160 mA/cm² is 15%.	51

4.11	Efficiency and power of cell 1 at 30 °C and 50 °C under atmospheric pressure. The efficiency of the cell at 50 °C is considerably higher by 7.5% compared to 30 °C at 160 mA/cm² due to lower ohmic losses. Regarding the power, a difference of almost 15% is observed. In both cases, the temperature has no significant effect at very low current densities since ohmic losses are negligible and mainly the activation overpotential prevails.	52
4.12	System temperature with time for constant current of $100~\text{mA/cm^2}$ (a) and $200~\text{mA/cm^2}$ (b). At $200~\text{mA/cm^2}$ the heat generation is larger thus leading to $20~\text{°C}$ higher steady state temperature. In both cases, the system has a nearly uniform temperature owing to the high electrolyte flow. It must be noted that in the high current density case the system reaches faster steady conditions due to the increasing thermoneutral voltage with the temperature that leads to faster equalization of the ambient heat losses to the heat generation.	53
4.13	System temperature variation versus time for electrolyte flow of 0.5Lt/min (a) and 25Lt/min (b) at 200mA/cm^2 . At high electrolyte circulation, the cooling of the stack is achieved and the temperature is observed to be uniform across the components of the system. On the contrary, at a low mass flow, the stack temperature is almost 10°C higher than that of the separators.	54
4.14	System temperature variation versus time for ambient air velocity of 0.1 m/s (a) and 1 m/s (b) at 200 mA/cm ² . For a nearly quiescent ambient air, heat losses are driven mainly due to natural convection leading to high stack temperature. On the other hand, at 1m/s air speed, the steady state temperature is 43.5 °C which is more than 10 °C than the 0.1 m/s air velocity case.	54
4.15	System temperature variation versus time for different electrolyte volumes in the system and $200~\text{mA/cm}^2$. It is noticeable that the volume of the electrolyte in the separator tanks does not influence the steady-state temperature of the system. An expected outcome is the longer time that takes for the system to reach this condition as the tank volume increases	55
4.16	System temperature variation at 200 mA/cm ² under 200 W of continuous (a) and 500 W of interval cooling. A continuous low cooling load causes a constant temperature of 50 °C in the stack that takes almost 4 hours to reach equilibrium. Regarding the interval cooling, the system needs a shorter time (45 mins) to achieve the lower temperature bound. After its	
4.17	deactivation, the stack temperature starts to increase again Steady state entropy generation in the stack as a function of current density. The generated entropy increases linearly to the current density since its value doubles when the system shifts from 80 mA/cm ² to 160 mA/cm ² . The combination of increasing heat lesses and the difference between the	56
	The combination of increasing heat losses and the difference between the thermoneutral with the reversible voltage is responsible for that trend.	57

4	.18	Experimental (dotted lines) and simulated (solid lines) heating curves of the stack (a) and the H ₂ separator tank (b). The thermal response of the stack and the separator, shown by the experiment, is almost the same and it is computed accurately by the model. The maximum deviation between	
4	.19	the measurements of test 1 and the simulation does not exceed 1.5 °C Experimental (dotted lines) and simulated (solid lines) heating curves of the stack (a) and the H ₂ separator tank (b). The current starts from 4 A and is increased by 2 A every hours. In both figures, the model underpredicts the temperature of the system. This discrepancy grows with time and after a certain point, it reaches a maximum value of 10.8%. The difference between the temperature gradient observed in the experiment	59
4	.20	(test 2) and the model is high in currents lower than 8 A whereas for higher currents they seem to be parallel	60
		simulation curve after 60 minutes emphasizing the higher heat generation at larger currents. Comparing the experimental and simulated curves, a considerable deviation is detected between the temperature measurements and the model where the discrepancy in the gradient is still observed. An immediate consequence is that the model underpredicts the heat genera-	
4	.21	Experimental (dotted lines) and simulated (solid lines) heating curves of the stack after correction (test 2). It is clearly shown that the implementation of the correction factor reduces the deviation to a maximum value of 5% and manifests the important role of the shunt current in the thermal response of the stack. This time, the lines are practically parallel denoting the reliability of the model if a larger experiment was executed.	63
4	.22	the reliability of the model if a longer experiment was executed. Faradaic, voltaic, and total efficiency of the stack with current density at 30 °C. The faradaic efficiency is relatively low for current densities smaller than 100 mA/cm² and thus the total stack efficiency suffers. On the other hand, the voltaic efficiency starts from really high values and drops with current owing to overvoltage losses. The total efficiency increases with current and reaches a peak at 170 mA/cm² which corresponds to a faradaic efficiency of nearly 100%. For higher currents, it reduces because the shunt current is zero while the ohmic losses grow linearly with the current.	64
A	1 .1	Illustration of the flows entering and exiting the stack. At the inlet, the pure electrolyte is inserted while the electrolyte with hydrogen, oxygen, and vapor leaves the stack. The amount of water consumed in the reaction	
		zone is relative insignificant enabling the use of a steady state molar balance.	70

List of Tables

3.1	Empirical constants for the electrolyte properties	23
3.2	Separator materials for alkaline electrolysers. Oxide membrane materi-	
	als show superior properties owing to lower specific resistance, smaller	
	thickness, and higher operating temperature. Data obtained from Refs.	
	[58]	26
4.1	Geometrical aspects and materials of the cell components. The flow of	
	the electrolyte is chosen to be high to avoid bubble congestion in the	
	interelectrode gap while the material selection is based on the cost and	
	their low electrical resistance according to the literature	46
4.2	Simulation input parameters for the theoretical modeling of the stack	
	behavior. The parameters were chosen according to custom experimental	
	conditions performed in the lab	53
4.3	Experimental conditions during the testing of the stack. The electrolyte	
	flow avoids the overheating of the stack while the ambient temperature	
	is controlled with the help of the A/C unit located in the lab. The PSU	
	ensures the monitoring of the current to the desired values	58
	\sim	

Nomenclature

Abbreviations

AWE Alkaline water electrolyser

CAPEX Capital expenditures

HER Hydrogen evolution reaction

MEA Membrane electrode assembly

OER Oxygen evolution reaction

OPEX Operational expenditures

PE Polyethylene

PEME Proton exchange membrane electrolyser

PSU Power supply unit

SOEC Solid oxide electrolysis cell

SS Stainless-Steel

Symbols

 \dot{m} Mass flow, kg/s

 \dot{n} Molar flow rate, mol/s

 \dot{Q} Heat flow rate, W

 $\dot{S}_{\rm gen}$ – Generated entropy, W/K

 ΔG Gibbs free energy change

 ΔH Enthalpy change

 ΔS Entropy change

- e⁻ Electron
- \overline{h} Specific molar enthalpy, J/mol
- $\overline{h}_{\rm forced}$ Average heat transfer coefficient in forced convection, W/m² K
- $\overline{h}_{\mathrm{natural}}$ Average heat transfer coefficient in natural convection, W/m² K
- $\overline{h}_{\rm stack}$ Average heat transfer coefficient of the stack, W/m² K
- \overline{Nu} Average Nusselt number
- A Electrode area
- $A_{\rm a}$ Anode surface area, cm²
- $a_{\rm ct}$ Catalyst specific area, cm² of catalyst per mg of catalyst
- $A_{\rm c}$ Cathode surface area, cm²
- $A_{\rm f}$ Frequency factor
- A_{stack} Surface area of the stack, m²
- $A_{\rm s}$ Membrane surface area, cm²
- C Surface concentration, mol \cdot cm⁻²
- C_{m} Constant-pressure overall thermal capacity of the single cell, J/K
- $c_{\rm p}$ Specific heat capacity, J/kg K or J/mol K
- $C_{\rm t,sep}$ Constant-pressure overall thermal capacity of the separator, J/K
- $C_{\rm t}$ Constant-pressure overall thermal capacity of the stack, J/K
- D Separator hydraulic diameter, m
- d Electrode-membrane distance, m
- $d_{\rm am}$ Anode-membrane distance, cm
- e Emissivity
- $E_{\rm a}$ Activation energy, J/mol
- F Faraday's constant, 96485 C/mol
- f(T, P) Correction function, V

- f_{ij} Empirical constant
- g Gravity, 9.81 m/s²
- H Electrode height, m
- h Specific enthalpy, J/kg
- I Current, A
- i Current density, A/cm²
- $i_{0,a}$ Anodic exchange current density, A/cm²
- $i_{0,c}$ Cathodic exchange current density, A/cm²
- i_0 Exchange current density, A/cm²
- i_0^{ref} Reference exchange current density, A/cm²
- $i_{\rm lim}$ Limiting exchange current density, 30 A/cm²
- $I_{\rm loss}$ Current loss, A
- $j_{\rm b}$ Backward reaction rate, mol/cm² s
- $j_{\rm f}$ Forward reaction rate, mol/cm² s
- k Reaction rate coefficient, s⁻¹
- $k_{\rm air}$ Thermal conductivity of air, W/m K
- $k_{\rm b}$ Backward reaction rate coefficient, s⁻¹
- $k_{\rm ele}$ Electrolyte conductivity, S/cm
- $k_{\rm f}$ Forward reaction rate coefficient, s⁻¹
- $k_{\rm g}$ Electrolyte conductivity with bubbles, S/cm
- $K_{\rm i}$ Empirical constant
- L Characteristic length, m
- $L_{\rm ct}$ Catalyst loading, mg of catalyst per cm² of electrode area
- $L_{
 m Ni/SS}$ Electrode thickness, cm
- m Molarity, mol/L
- $M_{
 m KOH}$ Molecular mass of KOH, g/mol

n Number of electrons transferred

 $N_{\rm cell}$ Number of cells

 $n_{\rm m}$ Slope in the tortuosity-degree of amorphousness relation

P Pressure, bar or Pa

 $P_{\rm ref}$ Reference pressure, Pa

 $P_{\rm w}$ Vapor pressure of electrolyte, bar or Pa

 $P_{\rm w}^*$ Vapor pressure of pure water, bar or Pa

Pr Prandtl number of air

R Universal gas constant, 8.3144 m³ Pa K⁻¹ mol⁻¹

 R_{KOH} Electrolyte ohmic resistance, Ω

 $R_{\rm m}$ Membrane ohmic resistance, Ω

 $R_{\rm Ni/SS}$ Nickel/SS electrode ohmic resistance, Ω

 $Ra_{\rm D}$ Rayleigh number over a cylinder of diameter D

Ra_L Rayleigh number over a plate of length L

 $Re_{\rm L}$ Reynolds number over a flat plate of length L

S Electrode active surface area, cm²

s Specific entropy, J/kg K or J/mol K

T Temperature, K

t Temperature, °C

 $T_{\rm f}$ Temperature of feed water, K

 $T_{\rm ref}$ Reference temperature, K

 $u_{\rm b}$ Bubble velocity, m/s

 $U_{\rm c}$ Cell voltage, V

 U_{rev} Reversible voltage, V

 $U_{\rm stack}$ Stack voltage, V

 $U_{\mathrm{T,P_0}}^{\mathrm{rev}}$ Reversible voltage at temperature T and atmospheric pressure, V

- $U_{\mathrm{T.P}}^{\mathrm{rev}}$ Reversible voltage at temperature T and pressure P, V
- $U_{\rm t,P}^{\rm tn}$ Thermoneutral voltage at temperature t and pressure P, V
- $U_{\rm tn}$ Thermoneutral voltage, V
- V Volume, m^3
- w Weight fraction of the electrolyte (%)
- $w_{\rm el}$ Width of electrode, m
- z Coefficient of the gas in the water split reaction
- Ox Oxidizing agent
- Red Reducing agent

Greek Symbols

- α Transfer coefficient
- α_{air} Thermal diffusivity of air, m^2/s
- $\alpha_{\rm am}$ Degree of amorphousness, %
- $\alpha_{\rm a}$ Anodic electron transfer coefficient
- $\alpha_{\rm corr}$ Correction coefficient for the heat generation term
- $\alpha_{\rm cr}$ Degree of crystallinity, %
- $\alpha_{\rm c}$ Cathodic electron transfer coefficient
- β Thermal expansion coefficient of air, K^{-1}
- $\delta_{\rm s}$ Membrane thickness, cm
- η Overpotential, V
- η_{cell} Total Efficiency
- $\eta_{\rm F}$ Faradaic efficiency
- $\eta_{\rm U}$ Voltaic efficiency
- γ Pressure dependency coefficient
- $\mu_{\rm ele}$ Dynamic viscosity of electrolyte, Pa · s
- ν Kinematic viscosity of air, m²/s

- $\omega_{\rm s}$ Membrane wettability
- $\overline{\alpha}_{\rm a}$ Average bubble volume fraction in the anode
- $\overline{\alpha}_{c}$ Average bubble volume fraction in the cathode
- Ψ Natural convection parameter
- $\rho_{\rm ele}$ Density of electrolyte, kg/m³
- $\rho_{\rm Ni}$ Resistivity of Ni electrode, Ω cm
- $\rho_{\rm SS}$ Resistivity of SS electrode, Ω cm
- σ Stefan-Boltzmann constant, 5.67· $10^{-8}~{\rm W/m^2~K^{-4}}$
- $\tau_{\rm s}$ Membrane tortuosity
- θ Electrode bubble coverage
- $\varepsilon_{\rm s}$ Membrane porosity (%)

Subscripts

- act Activation
- act- θ Activation due to bubbles
- amb Ambient
- an Anode
- c Cathode
- cons Water consumed
- el Electrode
- ele Electrolyte
- eq Equilibrium
- f Feed water

forced Forced convection

- gas H_2 or O_2 with vapor
- gen Generated heat
- in Inflow

lg Phase change of liquid-gas

liq Liquid and gas inflow/outflow

loss Current loss

m Membrane

mix Mixed electrolyte with gases

mixed Mixed convection

natural Natural convection

out Outflow

ox Oxidation reaction

rd Reduction reaction

reaction-zone Reaction zone heat

sep Separator

shunt Shunt current

stack Stack

v Vapor

water Deionized water

1 | Shift towards green

In this chapter, a brief discussion is made on the eco-friendly energy policy fostered by many governments, including the Netherlands, and the prominent role of green hydrogen. Opportunities and obstacles are also underlined as part of the energy transition. Finally, the focus of this research project is presented.

1.1 Motivation

One of humanity's biggest threats is the increase of the mean atmospheric temperature due to global warming. Intensive industrial operations and everyday human activities have undoubtedly increased greenhouse gases since the Industrial Revolution era [1, 2]. The employment of fossil fuels as a primary energy source led to the unraveling boom of CO₂ emissions to the atmosphere in the last 50 years, as seen in Fig. 1.1. The high concentration of CO₂ hampers the solar radiation from escaping the earth and thus leads to an increase in the ambient temperature [3]. Repercussions such as the rise of seawater level, potable water scarcity, and extreme weather conditions are becoming more and more common in the last decades [2]. An unprecedented event was the plunge of the CO₂ emissions from the power sector in Europe by almost 20% during the COVID pandemic [4]. Incidents like that give hope to humanity that the situation can be reversed if actions are taken straight away.

A turning point to reverse this direction is the Paris agreement (2015) where countries agreed upon holding the increase in the global average temperature to well below 2 °C above pre-industrial levels [6]. The goal of this agreement is the achievement of carbon neutrality till 2050. This commitment demands that the total global energy consumption be based on renewable electricity up to 40% by 2050. This practically means a 10-fold increase in renewable energy production from 1500 GW in 2015 to 15000 GW in 2050 [7].

Renewable energy technologies such as wind turbines and solar panels are ground-breaking due to their remarkable power generation with low impact on the environment [8]. Despite that, a major concern about the massive deployment of renewable energy technologies is their intermittent operation due to fluctuating weather conditions that render them insecure for stable energy supply [9]. Therefore, the operation of renewables with energy storage technologies is imperative. A prominent and sustainable solution to this problem is green hydrogen production through water electrolysis where the elec-

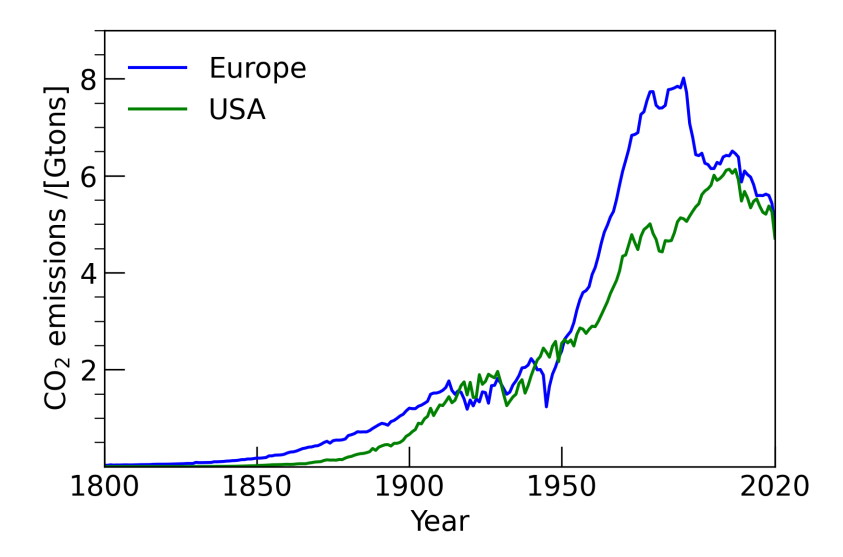


Figure 1.1: CO₂ emissions in Europe and USA from 1800 to 2020. A continuous surge in emissions is evident from 1950 and afterward. Data obtained from Refs. [5].

tricity generated from renewable energy sources is utilized for the formation of hydrogen with the help of electrolysers. The produced hydrogen can be stored in gas tanks and be used in the future when the electricity from renewables is not enough to cover the basic energy demands [9].

In general, there are three main types of hydrogen production: green hydrogen, blue hydrogen, and grey hydrogen [10]. Green hydrogen is a $\rm CO_2$ -free fuel that is produced from renewable energy sources, and the most prevailing technology for its production is water electrolysis. Grey hydrogen is produced from natural gas through methane steam reforming, and it entails a considerable amount of $\rm CO_2$ emissions. Similarly, blue hydrogen follows the same method as grey with the difference that a carbon capture technology is implemented for the reduction of $\rm CO_2$ emissions. Currently, 95% of the world's hydrogen production is grey and it is based on coal and natural gas [7, 10, 11]. Nonetheless, grey and blue hydrogen are not considered viable solutions for a zero-carbon future.

The green hydrogen to be produced is stored and used for the short-term or long-term to satisfy global energy demands by employing it as gas or converting it to other useful products [10], as seen in Fig. 1.2. There is an option to convert it back to electricity with the help of fuel cells but from a cost-effective aspect, gas form is more efficient since gas pipelines can carry more energy (20 GW) compared to electricity cables (2 GW) [12].

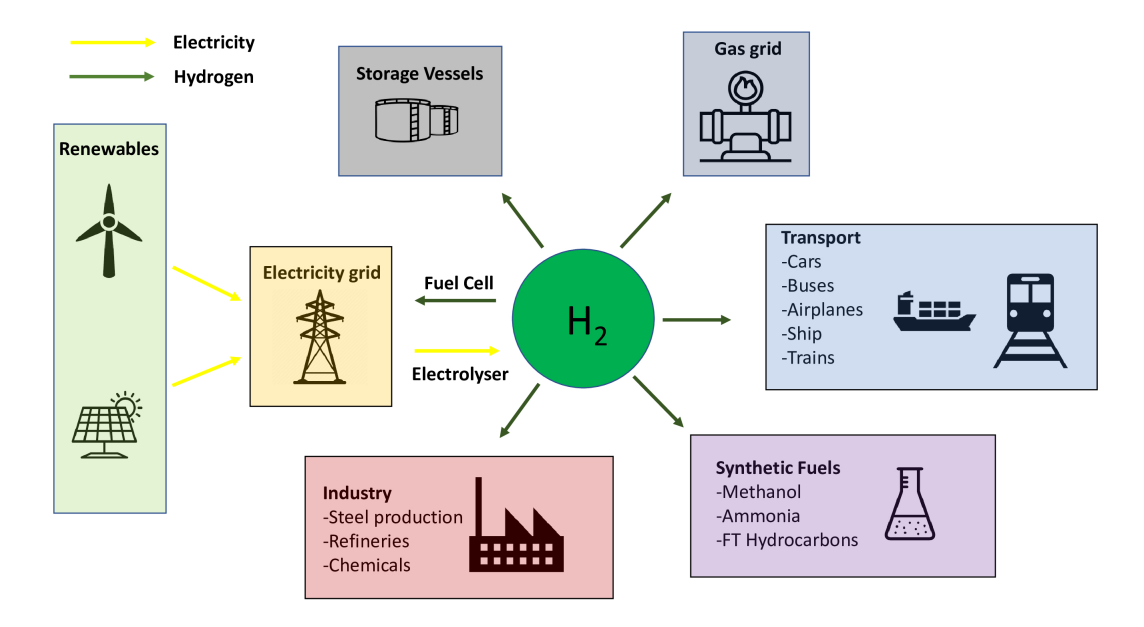


Figure 1.2: Hydrogen pathways from production to end use. Hydrogen in gas form can be used in many areas like transportation, industry, and domestic consumption while conversion back to electricity is possible through fuel cell technology. Powering the electrolyser with renewable energy leads to hydrogen production with minimal environmental impact. Figure reproduced from Refs. [13].

1.2 The path to the hydrogen economy

The term hydrogen economy manifests the replacement of fossil fuels with hydrogen in all the major sectors that are not able to use electricity for their everyday operations, such as steel factories and heavy-duty transport [14]. Most countries consider this strategy indispensable for the transition to a climate-neutral future. Nevertheless, its success is halted by many barriers not only from the economic aspect but also technological.

First and foremost, the higher production costs of green hydrogen compared to grey renders the idea financially unattractive for large-scale applications. The average market price of green hydrogen is $4\text{-}6 \in /\text{kg}$ where factors such as electricity price and operating hours of the electrolyser play a crucial role in price determination. On the other hand, the average market price of grey hydrogen is around $2 \in /\text{kg}$ and is dictated by the price of the natural gas which in most cases is low-cost [7, 10]. The absence of hydrogen refueling stations, specifically 470 worldwide, and the premature gas pipeline network for hydrogen transportation that is only 5000 km indicates that the infrastructure is not sufficient for this transition. Finally, energy losses associated with the operation of the electrolyser are close to 30% without considering the additional losses that occur due to transportation and final use [10].

The Netherlands, committed to a more sustainable future, has forged its national strategy for the achievement of the hydrogen economy. One of the main pillars in their

agenda is the construction of hydrogen pipelines and the use of already existing natural gas pipelines for the accommodation of hydrogen transport all over Europe. In addition, the connection of hydrogen to offshore wind energy in conjunction with the improvement of the electricity grid will substantially upgrade the production capabilities and reliability of the system. Lastly, subsidies for research and development are indispensable for reducing the cost of green hydrogen production, and for that reason, the government plans to fund projects up to $\in 15$ million. With that being said, the national policy focuses on making green hydrogen the primary energy source and aims in turning the country into an energy hub [15].

Adriaan van Troostwijk and Johan Deiman in 1789 were the first to decompose water into hydrogen and oxygen by applying electricity from an electrostatic generator [16]. Thenceforth, many projects worldwide have taken place to produce hydrogen on a large scale. One of them is by Norsk Hydro in 1928 (Norway) where electrolysers utilized available hydropower to produce hydrogen. The plant's total capacity was 27900 Nm³ of hydrogen (165 MW) and the main purpose was the production of ammonia for fertilizing products.

In the Netherlands, the pilot plant 'PosHYdon' (2021) in the North Sea has a capacity of 1 MW and uses wind energy to operate an electrolyser installed on an offshore platform [17, 18]. The seawater, after desalination, is fed to the electrolyser for hydrogen production. In the future, numerous green hydrogen projects are planned to be built and one of them is the energy park in Eemshaven (Energiepark Eemshaven-West, 2020-2023), where wind and solar electricity will be directly connected to an electrolyser and a battery. The power capacity of the plant will be initially 10 MW and it is expected to scale up to 100 MW by 2027. Another well promising project is the NortH2 where 3-4 GW of electricity from a wind farm in the North Sea will be converted to hydrogen and it is expected to be fulfilled in 2030 [18].

1.3 XINTC Global

XINTC Global is a start-up company that is specialized in the manufacturing of alkaline electrolysers and focuses on mid-range power applications (150 kW - 50 MW) [19]. Their strategy is to build standardized and modular alkaline electrolysers together with the balance of plant delivered in a containerized form. The containerized solutions are 'plug and play' with atmospheric hydrogen production. The produced hydrogen can be delivered for pressures up to 30 bar. Atmospheric production of hydrogen allows using inexpensive materials such as plastic and metals that are abundant in nature and lower the capital expenditures of electrolysers (CAPEX). On the other hand, the novel design, the modularity of the product, and the advanced control system aim to minimize the operating expenses during the process (OPEX) and maximize the hydrogen production from renewables.

1.4 Research Objectives

The operation of the electrolyser is considerably affected by the temperature and the pressure. The electricity flow through it is accompanied by heat generation and temperature increase. The electrochemical reactions that take place in conjunction with the start-stop mode due to connection with an intermittent source lead to unsteady state operational conditions. In addition, each electrolyser has different dimensions and materials so the energy losses differ significantly. For that reason, this research aims to investigate how various parameters affect the efficiency, energy consumption and hydrogen production rate of the electrolyser. In specific,

- How do geometrical parameters affect energy losses?
- How does temperature affect energy consumption?
- What impact does the variable current input have on the performance of the electrolyser?
- What useful information can we extract from sensitivity analysis of current, electrode and membrane materials, and ambient conditions?

This project will be executed in cooperation with XINTC Global, and the main purpose is to investigate thoroughly the behavior of the company's electrolyser. For a more realistic approach to the problem, experiments will be performed.

2 | Electrolysers - a theoretical analysis

The basic principle of green hydrogen is the utilization of renewables to power the decomposition of water into hydrogen and oxygen and for that reason, the electrolyser is the focal point in sustainable production. The three main types of electrolysers are discussed, and the process flow of the alkaline type is described. The basic physical principles and sources of energy loss are elucidated for the alkaline electrolyser. Finally, relevant research work from the literature is presented and some useful conclusions are drawn.

2.1 Types of electrolysers

The main types of electrolysers are the alkaline water electrolyser (AWE), the proton exchange membrane electrolyser (PEME), and the solid oxide electrolysis cell (SOEC). The subsequent paragraphs describe their working principle, the materials used, and some main advantages and disadvantages.

2.1.1 Alkaline water electrolyser (AWE)

An alkaline electrolyser is a device that it consists of two electrodes immersed in an electrolyte with a membrane in between them [20]. One of the electrodes operates as an anode while the other as a cathode and are made of metal oxides (LaNiO₃, NiCO₂O₄) due to the high electrochemical activity [21]. Perforated plates or expanded mesh are the usual structures of the electrodes. The electrolyte in the alkaline electrolyser is NaOH or KOH and the concentration is ranging from 25-35 wt%. The flow of electrolyte is in both the anode and cathode regions to ensure pressure equilibrium and concentration homogeneity. In the cathode, water is decomposed in hydrogen and hydroxide ions (OH⁻) where the former leaves the cell as a gas, and the latter travel through the membrane and react in the anode to produce oxygen gas. The production of hydrogen in the cathode is called hydrogen evolution reaction (HER) while the oxygen production in the anode is called oxygen evolution reaction (OER). The purpose of the membrane (diaphragm) is to separate the two product gases (O₂, H₂) and allow the flow of the ions between the two compartments [22]. Fig. 2.1, illustrates the process involved in the

alkaline electrolysis while the reactions that take place are shown below.

Cathode:
$$2H_2O + 2e^- \rightarrow 2OH^- + H_2$$
 (2.1)

Anode:
$$2OH^- \to 0.5O_2 + H_2O + 2e^-$$
 (2.2)

The purpose of the membrane is to prevent a short circuit, be conductive to the OH⁻

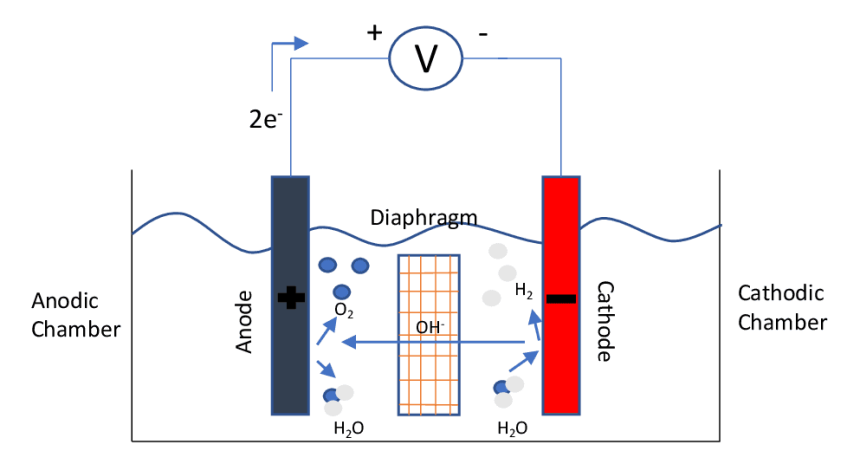


Figure 2.1: Illustration of the alkaline electrolysis cell including the anode, cathode, membrane, and the power source. In the cathode, water is split to hydrogen and hydroxides where the later travel through the membrane to the anode to give oxygen and water. Simultaneously, the diaphragm blocks gases from traveling to the other compartment, allowing only OH⁻. The power source ensures the electron transfer from the anode to the cathode in order for the reactions to take place. Figure reproduced from Refs. [23].

and block the produced gases from going to the other compartment. The first membranes to be used were made from asbestos, but later on, were replaced by Zirconium Oxide (Zirfon) due to its superior conductivity and stability in the operating conditions of the electrolyser [21]. The temperature range of the electrolyzer is between 60-80 °C owing to the high conductivity of the electrolyte, while the pressure does not exceed 30 bar. The current density is between $0.2\text{-}0.4~\text{A/cm}^2$, characterizing it as a low current density device. The main advantages of an alkaline electrolyser are its technological maturity and the low cost of construction that allows its deployment on a large scale. On the other hand, corrosion of the electrodes renders it vulnerable to part-load operations while its slow start-up time makes it difficult to be coupled with renewable energy sources [20].

In the traditional alkaline cell, there is a gap between the electrodes and the membrane that is filled with electrolyte. This type of configuration was found to induce lower efficiency owing to high ionic losses. In a consequent step, a zero-gap electrolyser was built-in which the electrodes are pressed on the membrane surface to minimize the ohmic losses [21]. For large-scale applications, an electrolytic stack that consists of several cells connected in series must be employed for a considerable amount of hydrogen

production. The two main cell designs are monopolar and bipolar. In the monopolar electrolytic stack, the cells are connected in parallel to an energy source while each electrode is positively or negatively charged. In the bipolar design, the cells are connected in series with each other and only the outer electrodes are connected to the source, so the electrodes in the middle are positively charged on one side and negatively on the other [24].

2.1.2 Proton exchange membrane electrolyser (PEME)

In a PEM electrolyser, two electrodes are attached to a thin membrane forming a zero-gap configuration while the acidic electrolyte is contained inside the membrane (Membrane Electrode Assembly, MEA). The materials used for the electrode and the contact elements (i.e., bipolar plates, current collectors) are iridium, titanium, and platinum due to their high durability in acidic solutions. As voltage is applied, water is inserted from the anodic side and is oxidized in oxygen gas and protons (H⁺). The protons move through the membrane to the cathode, where they reduce to hydrogen gas. The typically used membrane material is Nafion owing to its high conductivity and small thickness. The operating conditions of the PEM electrolyser involve temperatures between 50-80 °C, pressures up to 50 bar, and current densities reaching 2 A/cm². The reactions that take place in the PEM electrolyser are shown below [20, 21].

Anode:
$$H_2O \rightarrow 2H^+ + 0.5O_2 + 2e^-$$
 (2.3)

Cathode:
$$2H^+ + 2e^- \rightarrow H_2$$
 (2.4)

The benefits of PEM electrolysers are the high current density and the low voltage drop that lead to large amounts of hydrogen production at high efficiency. In addition, the small volume and the fast start-up time make it suitable for connection with a renewable energy source. Nevertheless, the use of expensive materials such as Iridium and Platinum for the components of the electrolyser in combination with the low operating lifetime drives up the production cost and hinders the implementation on a large scale [8, 20].

2.1.3 Solid oxide electrolysis cell (SOEC)

Solid oxide electrolysers are different compared to the previously mentioned ones because they operate under extremely high temperatures (500-800 °C). The materials of the anode and cathode are lanthanum strontium manganate and nickel, respectively. The steam water is reduced in the cathode to form hydrogen gas and oxygen ions. The dense electrolyte made of zirconium oxide doped with Y_2O_3 (yttria) ensures the movement of the oxygen anions that get oxidized in the anode and lead to oxygen production.

The advantage of the solid oxide electrolyser is its high efficiency, close to 100%, on account of the high electrochemical kinetics and the option to use partly waste heat as energy input instead of electricity. Despite that, this type of electrolyser is still in the

research phase and has not yet been commercialized. Problems linked to the durability of the materials and the long start-up times hamper its large-scale production [25].

2.2 Process flow

An alkaline electrolysis system involves a combination of equipment that take part in the production of purified hydrogen gas. The heart of the system is the electrolyser where water is dissociated into oxygen and hydrogen gas. Subsequently, the product gases move on to the oxygen and hydrogen separator in which gas bubbles are separated from the liquid solution. At the same time, the electrolyte flows back to the electrolyser with the help of a pump. The separated gases are subjected to a purification system that entails purification and drying for high purity and low water content. On the other hand, the electrolyte flow from the anode (anolyte) and the cathode (catholyte) is firstly cooled to keep the temperature of the electrolyser constant. The performed electrical work in the electrolyser generates heat and leads to elevated temperatures, hence electrolyte cooling is necessary for keeping the process under control. The reactions (Eq. 2.1 and 2.2) indicate that in the anodic chamber water is produced while in the cathodic it is consumed, thus a concentration difference is expected to occur. Consequently, the anolyte and catholyte, after cooling, should be mixed and then inserted into the cell.

2.3 Thermodynamics of water electrolysis

The main principle of electrolysis is the splitting of water into hydrogen and oxygen, and it is imperative to comprehend the thermodynamics of this process for the calculation of the energy balance. The reaction is as follows

$$H_2O \to H_2 + 0.5O_2$$
 (2.5)

First of all, water electrolysis is a non-spontaneous reaction, consequently, an outer source must provide energy for its dissociation. In this case, Gibbs free energy is positive and denotes the minimum amount of energy to be provided for the reaction to take place. Its value at standard conditions is 237 kJ/mol. The enthalpy change of water splitting is positive and has a value of 285.8 kJ/mol, meaning that the reaction absorbs energy [26]. The relation of Gibbs free energy and enthalpy is shown below.

$$\Delta G = \Delta H - T \Delta S \tag{2.6}$$

Where ΔG is the change in Gibbs free energy of water splitting, ΔH is the enthalpy change of the reaction, T is the temperature, and ΔS is the entropy change. In water electrolysis, it is common to express the input energy in voltage:

$$U_{\text{rev}} = \frac{\Delta G}{nF} \tag{2.7}$$

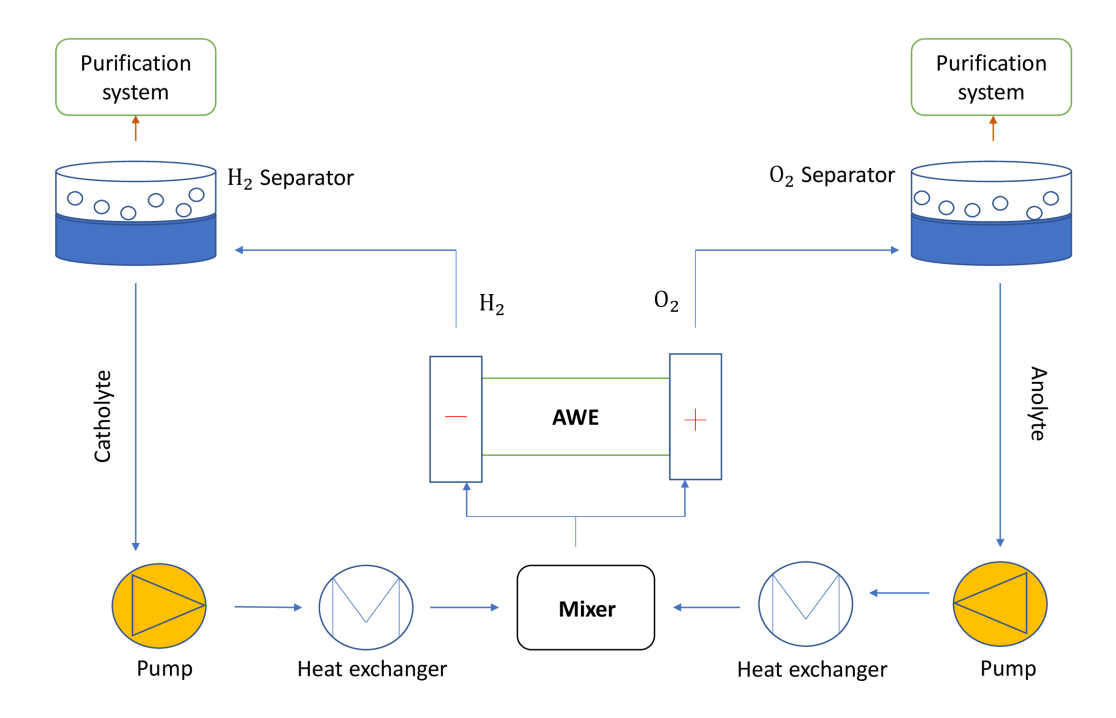


Figure 2.2: Process flow diagram of the alkaline electrolyser. The electrolyte is circulated from the separators via pumps and it is cooled with heat exchangers. To avoid concentration gradients, the two streams (anolyte, catholyte) are mixed before being inserted into the stack. The stack outflow is driven back to the separators for the separation of the electrolyte from the gas products that end up in the purification system.

Where F=96485 C/mol is Faraday's constant, and n=2 is the electrons exchanged during the reaction. At standard conditions, the reversible potential $U_{\text{rev}}=1.23$ V and its value depends on the temperature and pressure [27]. Nevertheless, in the reversible voltage calculation, it is assumed that the cell has a constant temperature, and the heat of evaporation of water, during its conversion to hydrogen and oxygen gas, is not considered [28]. For that reason, thermoneutral voltage is defined as follows

$$U_{\rm tn} = \frac{\Delta H}{nF} \tag{2.8}$$

At standard conditions (25 °C, 1 bar), the thermoneutral potential $U_{\rm tn}=1.48$ V. When the applied voltage is equal to the thermoneutral, then the temperature of the cell remains constant. For smaller values the temperature drops, while for higher voltage heat production starts to occur, thus increasing the cell temperature [27]. The variation of thermoneutral and reversible voltage for 35 wt% KOH at ambient pressure is shown in Fig. 2.3. As the temperature increases, more vapor is produced absorbing heat from the cell, hence higher voltage is needed to keep the temperature constant. Regarding the

reversible voltage, the increasing temperature reduces the Gibbs free energy of reaction due to lower activation energy needed.

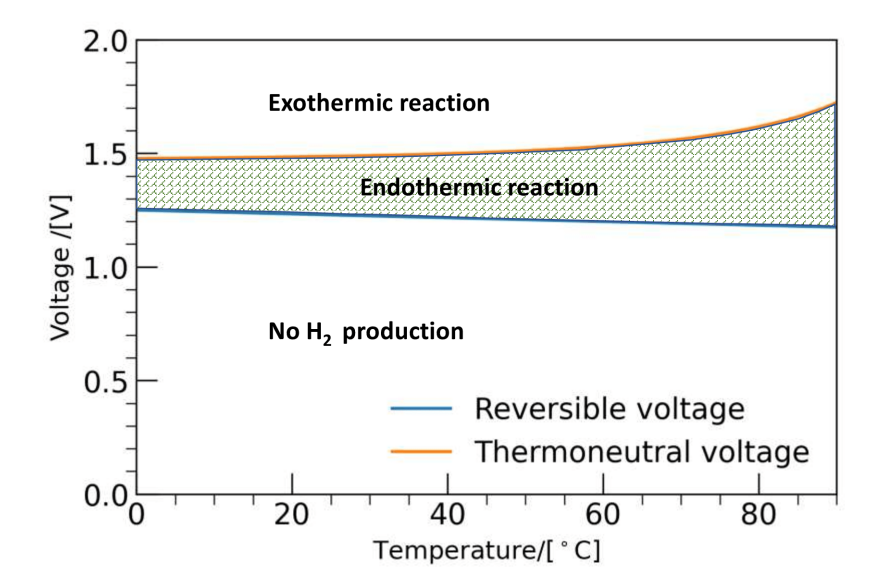


Figure 2.3: Thermoneutral and reversible voltage as a function of temperature for 35 wt% KOH at ambient pressure. The former increases with temperature due to vapor production and the latter decreases caused by a lower activation energy. The zone above the thermoneutral voltage leads to heat generation while below the reversible voltage no reaction takes place. The area in between is characterized by an endothermic reaction.

The variation of the reversible potential is expressed by the Nernst equation with temperature, pressure, and molarity dependence [29].

$$U_{\rm T,P}^{\rm rev} = U_{\rm T,P_0}^{\rm rev} + \frac{RT}{nF} \cdot \ln \left(\frac{(P - P_{\rm w})^{1.5} \cdot P_{\rm w}^*}{P_{\rm w}} \right)$$
 (2.9)

Where $U_{\mathrm{T,P_0}}^{\mathrm{rev}}$ is the reversible potential at temperature T and atmospheric pressure, P is the pressure of the system, P_{w} is the partial pressure of the KOH solution and P_{w}^{*} is the partial pressure of pure vapor. The calculation of the terms involved in the Nernst equation as well as the calculation of the thermoneutral potential as a function of pressure and temperature are investigated by many researchers [30, 31, 32]. In their analysis, the non-ideality of the produced gases is considered by using a modified virial equation of state. Moreover, the water content of the gases is also taken into account since part of the water evaporates and leaves the electrolyser with the other gases as a binary solution (O₂-vapor, H₂-vapor) [31].

2.4 Electrochemical effects

The application of a voltage in the electrolyser induces electrochemical reactions that take place at the interface of the electrode and the electrolyte. The rate of reactions depends on the treatment of the interface, the concentration of the electrolyte, and the activation energy of the reaction [30]. In a redox reaction, near each electrode surface, both a forward and backward reaction take place at the same time but different rates [26]. The difference in these rates is the current generated in the electrolyser. In general,

$$Red \iff Ox + ne^-$$
 (2.10)

The rate of reaction depends on the surface concentration of the reactant and is expressed, for the forward (oxidation) and backward (reduction) reactions, as follows.

$$j_{\rm f} = k_{\rm f} C_{\rm Red} \tag{2.11}$$

and

$$j_{\rm b} = k_{\rm b} C_{\rm Ox} \tag{2.12}$$

According to Faraday's law, the net current density is

$$i = nF(j_{\rm f} - j_{\rm b}) \tag{2.13}$$

Where i is the net current density in A/cm², n is the number of electrons transferred during the reaction, and F = 96485 C/mol is the Faraday's constant. In addition, $j_{\rm f}$ and $j_{\rm b}$ are the forward and backward reaction rates in mol/cm² s, $C_{\rm Ox}$ and $C_{\rm Red}$ are the surface concentrations of the oxidizing and reducing agent in mol/cm² while $k_{\rm f}$ and $k_{\rm b}$ are the forward and backward reaction rate constants, respectively, in s⁻¹. At equilibrium, no net current flows in the electrolyser since the forward reaction rate is equal to the backward reaction rate, and the equilibrium voltage is established between the electrode and the electrolyte. The current at which equilibrium is reached is called exchange current density [26].

Based on the transition state theory [33] the reaction rate coefficient is expressed as

$$k = A_{\rm f} \cdot e^{\frac{-E_{\rm a}}{RT}} = A_{\rm f} \cdot e^{\frac{-\Delta G^{\rm act}}{RT}} \tag{2.14}$$

Where $E_{\rm a}$ denotes the activation energy of the reaction and $A_{\rm f}$ is the frequency factor expressing the number of attempts made to cross the energy barrier. The activation energy is proportional to the Gibbs free energy of the reaction adjusted by the activation overvoltage. This is the extra applied voltage to break the equilibrium of the electrochemical reaction and allow the forward or backward reaction to prevail [34]. Particularly, for oxidation reaction:

$$\Delta G_{\text{ox}}^{\text{act}} = \Delta G_{\text{ox}}^{\text{eq}} - \alpha_{\text{ox}} n F \eta \tag{2.15}$$

and for reduction reaction:

$$\Delta G_{\rm rd}^{\rm act} = \Delta G_{\rm rd}^{\rm eq} + \alpha_{\rm rd} n F \eta \tag{2.16}$$

Where $\Delta G_{\rm rd}^{\rm act}$ and $\Delta G_{\rm ox}^{\rm act}$ are the reduction and oxidation activation energies, $\Delta G_{\rm ox}^{\rm eq}$ and $\Delta G_{\rm rd}^{\rm eq}$ are the equilibrium Gibbs free energy during oxidation and reduction, respectively. The number of transferred electrons is denoted by n while $\alpha_{\rm ox}$ and $\alpha_{\rm rd}$ are the transfer coefficients corresponding to the oxidation and reduction reactions describing a multi-electron process [30]. Lastly, η is the activation overvoltage and expresses the difference between the electrode potential and the reversible potential.

When the rate constant is inserted in the net current, the well-known Butler-Volmer equation is derived. The Butler-Volmer equation describes the relationship between the current density and the overvoltage between the electrode and the electrolyte. If the concentration of KOH at the bulk and the electrode surface are assumed equal [35], and the exchange current density is inserted, then the equation yields that,

$$i = i_0 \left[\exp\left(\frac{\alpha_{\text{ox}} nF\eta}{RT}\right) - \exp\left(\frac{-\alpha_{\text{rd}} nF\eta}{RT}\right) \right]$$
 (2.17)

Where i is the current density, and i_0 is the exchange current density. The exchange current density is the current that flows during equilibrium. The higher its value the lower the energy barrier between the electrode and the electrolyte. High exchange current densities denote that the electrode area is more active and lower activation overpotential is required for the same generated current [26]. In alkaline electrolysis, the exchange current density of HER is orders of magnitude larger than that of OER [26, 36]. The reason for that is the number of electrons that must be transferred to produce one mole of gas as well as the electrocatalyst layer on the surface of the electrode. In the HER two electrons are required to produce one mole of hydrogen while in the OER four electrons are needed, thus the electron transfer process in OER is more complex [27].

In case the overpotential is small $(\eta < \frac{RT}{nF\alpha_{\rm ox/rd}})$ the Butler-Volmer equation can be linearized as follows

$$i = i_0 \frac{nF(\alpha_{\rm ox} + \alpha_{\rm rd})}{RT} \eta \tag{2.18}$$

When the overpotential is high enough such that one of the exponentials contributes less than 1% to the total current, then the Tafel equation is applied [30] and is defined as

$$\eta = 2.3026 \frac{RT}{nF\alpha_{\text{ox/rd}}} \log\left(\frac{i}{i_0}\right) \tag{2.19}$$

The Tafel equation is a logarithmic approximation of the Butler-Volmer equation, and it assumes that the concentration of the electrolyte in the electrode interface is the same as the bulk. Hence, the limiting factor is the slow kinetics that takes place in the electrode and not the diffusion of the electrolyte. It is important to note that the enhancement of the exchange current density leads to lower overvoltage for the same current, and thus lower energy consumption for the same production rate.

2.5 Cell energy losses

Water electrolysis is accompanied by voltage losses that occur due to the different components and processes that are present in the electrolyser, hence the cell voltage should be higher than the reversible for the gas production to take place. The main contributors to the voltage losses are associated with ionic resistances, electrical resistances, gas crossover, diffusion of reactants, and electrochemical kinetics [26].

2.5.1 Electrochemical kinetics

As already mentioned, the reversible voltage induces slow kinetics, thus an additional voltage is necessary to speed up the net reaction and lead to the formation of the products. For that reason, high current densities are applied enabling the calculation of the overpotential by using the linearized Butler-Volmer or the Tafel equation.

2.5.2 Electrolyte

In alkaline water electrolysis, a KOH solution is used, where the OH⁻ ions are the charge carriers between the anode and the cathode. The volume of the electrolyte in the cell is dictated by the gap between the two electrodes and the losses that occur are proportional to the current (ohmic) and the gap distance [22]. Consequently, a large gap induces a large voltage drop, but a considerably small gap (i.e., zero-gap) can lead to extra losses due to two-phase flow effects [37]. The concentration of the KOH solution is frequently selected between 25-35% mass fraction because experiments have shown that in this range, it has the highest conductivity [38]. Furthermore, the conductivity increases linearly with temperature but due to the evaporation of the electrolyte a temperature range of 60-80 °C is selected for atmospheric conditions.

2.5.3 Membrane & Electrodes

As already discussed, the principal role of the membrane is to separate the gas products and allow the flow of ions through the anodic and cathodic chambers. The material and the thickness of the membrane are crucial not only for the above-mentioned reasons but also for ohmic losses, especially for zero-gap configurations where the membrane has the highest portion. Ohmic losses are proportional to the thickness of the membrane and decrease with temperature. In the case of the Zirfon membrane, the custom thickness is 0.5 mm, and its normalized area resistance at 25 °C is approximately 0.2 Ω cm² [39]. On the contrary, electrodes of alkaline electrolysers are made of pure nickel (99.99%) that have high electrical conductivity and their contribution to the ohmic losses is insignificant. Experiments have shown that the resistivity of the electrodes increases with temperature [40].

2.5.4 Bubbles

The flow of current in the electrodes induces the production of dissolved gases. When the concentration of the dissolved products reaches the supersaturation limit, gas bubbles start to form in nucleation sites along the electrode surface [41]. The presence of bubbles in the electrolyser affects energy losses during the operation. Particularly, as the current density increases more bubbles start to nucleate and cover a larger area the electrode. Therefore, part of the surface is electrochemically inactive, and the local current density is increased due to the reduced available surface area. Consequently, based on the Tafel kinetics (Eq. 2.19), overvoltage due to kinetics rises significantly. Moreover, as the bubbles detach from the electrode surface, they start to disperse in the electrolyte. The presence of bubbles in the electrolyte reduces the conductivity by hindering the flow of ions and hence increases electrolyte ohmic losses. Concerning the operating conditions, the research field indicates that the bubble electrode coverage and the bubble volume fraction in the electrolyte reduce with increasing pressure and electrolyte flow [42, 43]. On the other hand, the effect of temperature is not yet clear since some publications claim that it does not play any major role [42], while other research work supports that it enhances the bubble presence in the electrolyser [44].

2.5.5 Gas diffusion

One of the main issues in the operation of the alkaline electrolyser is the hydrogen and oxygen gas crossover. This phenomenon is undesirable because it lowers the hydrogen gas purity and faradaic efficiency posing safety issues and causing the shutdown of the whole process [45]. The hydrogen crossover to the anode is prevailing compared to that of oxygen in the cathode due to the higher diffusivity of the hydrogen in the electrolyte [28]. In general, gas purity is affected by many factors such as temperature, pressure, electrolyte concentration, and mass flow. The mechanisms that contribute to the hydrogen crossover are associated with the dissolved gas in the electrolyte and the crossover of the hydrogen bubbles through the membrane [46]. The membrane must prevent the bubble diffusion to the other compartment because it leads to recombination with oxygen (water formation) and lowers the efficiency of the cell. Additionally, when the dissolved hydrogen is present in the anode, the concentration of hydrogen in the oxygen bubbles increases and leads to reaching the explosion limit in the separator. This is of special importance at low current densities because the amount of oxygen produced is low while the hydrogen crossover remains the same since it does not depend on current density. A consequence of that is the increase in the concentration of hydrogen at the anode. Furthermore, the mixing of the analyte and catholyte is an additional mechanism that increases hydrogen content in the anode. This happens because dissolved hydrogen in the catholyte is recirculated back in the cell after being mixed with the analyte. A common practice to prevent gas crossover is the alternating insertion of the analyte and catholyte into the cell as mixed and unmixed [21].

2.5.6 Concentration overvoltage

At high current densities, the consumption of reactants at the electrode surface is so rapid that the region is depleted. Consequently, a concentration gradient is established between the interface and the bulk electrolyte that leads to the diffusion of the reactants to the electrode surface. When the surface concentration is zero, the reaction rate is limited by the diffusion rate, and the current density is called limiting current density [26, 35]. It is noteworthy that in the case of industrial alkaline electrolysers this does not happen because they operate at a current density lower than 0.6 A/cm^2 , and thus can be neglected in the calculation of the overpotential [47, 48, 49].

2.6 Efficiency

An important aspect of water electrolysis is the efficiency of the electrolyser. High efficiency is essential to make green hydrogen a financially feasible solution for a climate-neutral future. In the literature, many ways are reported based on the reference input power, but the most prevailing definition used by the research community is based on the high heating value of hydrogen. Furthermore, efficiency consists of two parts, namely the voltaic and the faradaic efficiency [24, 28]. In specific,

$$\eta_{\text{cell}} = \eta_{\text{U}} \cdot \eta_{\text{F}} \tag{2.20}$$

Where

$$\eta_{\rm U} = \frac{U_{\rm tn}}{U_{\rm c}} \tag{2.21}$$

and

$$\eta_{\rm F} = 1 - \frac{I_{\rm loss}}{I} \tag{2.22}$$

In the equations above, η_{cell} is the total efficiency of the electrolysis cell, and η_{U} , η_{F} are the voltaic and faradaic efficiency, respectively. Moreover, U_{c} is the total voltage applied to the cell while I_{loss} refers to the amount of current loss.

The main causes for current loss are the hydrogen and oxygen cross permeation and the parasitic current along the inlet/outlet manifolds in a stack. Thus, faradaic efficiency denotes the ratio between the actual and theoretical amount of hydrogen produced during the water electrolysis process. The proportion of current loss decreases with increasing current due to a large amount of gas production [47, 50]. It should be noted that a higher hydrogen production rate demands higher cell voltage due to the increase of the voltage losses. This results in lower voltaic efficiencies of the cell with increasing current. Lastly, high temperatures are proven to be beneficial for efficiency since the ohmic losses decrease and the reaction kinetics are enhanced.

2.7 Polarization curves

The polarization curve indicates the voltage of the electrolyser as a function of the current density for a specific temperature, and it is of paramount importance since it reveals the energy demand for hydrogen production. It is desired that for a specific current density the voltage be as low as possible for minimum energy consumption. A thorough literature survey indicates that there are two main modeling approaches for the alkaline electrolyser, the empirical and the analytical. The empirical models use available experimental data to create parametric equations that describe the voltage and the current density of the electrolyser. This mathematical approach does not consider the geometrical characteristics and the operating conditions of the electrolyser (i.e., electrode gap, temperature, electrolyte concentration). A major improvement is the incorporation of non-linear temperature-dependent terms that predict the performance of the electrolyser with good accuracy. Although mathematical models are easy to use, they require many data sets to derive them while simultaneously being unique for each electrolyser and operating conditions. A change in pressure or electrolyte concentration renders the model inaccurate, and experiments must be repeated. Up to this point, mathematical models have been implemented for the modeling of electrolysers with solar panels and wind turbines [51] as well as several lab-scale electrolysers [24, 52]. The most detailed model in alkaline electrolysis is the Simelint program developed under the Saudi Arabian-German HYSOLAR project, where the model predicts the cell voltage, temperature, and gas purity of the electrolyser for every operating condition [53].

On the contrary, analytical models include equations from the physical domain of electrochemistry, two-phase flow, and thermodynamics. These models can predict the performance of the electrolyser under different temperatures and pressures, while they provide a better insight into the weaknesses of the system. The consideration of effects, such as the electrolyte bubble volume and the gap gives the option to optimize the electrolyser and minimize the energy requirements. Experimental data sets are not necessary and by using general correlations the model can be used for other electrolysers as well. The already existing work on lab-scale electrolysers supports the accuracy of the models and their ability to identify the main sources of energy losses [29, 30, 48, 54].

2.8 Thermal modeling

The role of temperature is crucial in the operation of the alkaline electrolysis and for that reason, it is important to investigate the thermal behavior of the electrolyser. High temperatures are beneficial for the efficiency of the system due to the decrease in ohmic losses, enhancement in the electrode kinetics, and reversible potential reduction. On the other hand, the purity of the products and the lifetime of the materials are diminished. The operation of the electrolyser with renewable energy sources poses a challenge due to the fluctuating current densities that affect the whole performance of the system. A detailed survey shows that there are not many existing models to investigate this aspect

of the problem. The few existing publications assume a lumped capacitance model where the temperature inside the electrolyser is uniform and spatial distributions are ignored. The principal interest is the performance of the electrolyser under DC or AC input [55, 56] and the effect of process conditions like electrolyte flow and power load [47].

2.9 Conclusions

The literature review presented above suggests that a realistic investigation of the alkaline electrolyser necessitates a rigorous approach that encompasses all the losses related to the geometry and the materials used. Furthermore, the confusion about the bubble effect indicates that experimental data are a requisite. For that reason, a mathematical model in Python will be built with equations that emanate from the physical laws of electrochemistry as well as empirical relations from experimental data. The analysis of the electrolyser from a thermodynamic point of view will establish the relationship between the temperature and the efficiency of the process. It is anticipated that the model will provide the necessary insight for identifying the major sources of energy loss and give guidelines for the enhancement of the electrolyser's performance.

3 | Cell Modeling

The modeling of the alkaline electrolyser demands the detailed elucidation of the equations and assumptions implemented for the approach of each aspect of the process. In this chapter, all the necessary steps for the electrochemical modeling will be presented with a focus on the energy losses inside the cell. In addition, the modeling of the system's thermal response is incorporated in the analysis of the chapter.

3.1 Thermodynamic properties

In this section, the electrical and thermal properties of the cell are discussed and all the necessary formulas are displayed.

3.1.1 Electrolyte

The KOH electrolyte is the carrier of the ions in the alkaline cell and its conductivity is important for the efficiency of the process. In atmospheric electrolysis applications, the temperature range is 50-80 °C and the concentration is around 30 wt%. An accurate electrolysis model necessitates the investigation of its thermal and electrical properties as a function of the working conditions.

The concentration of the electrolyte on a molar basis is a function of the solution's density and is expressed by the general equation:

$$m = \frac{w}{100} \cdot \frac{\rho_{\text{ele}}}{M_{\text{KOH}}} \tag{3.1}$$

Where m is the concentration in mol of KOH per liters of solution, w is the weight percentage concentration (%), $\rho_{\rm ele}$ is the electrolyte density in kg/m³, and $M_{\rm KOH}$ =56.105 g/mol is the molecular weight of KOH.

Incorporating the density of the solution as a function of temperature and replacing the molar weight, the equation above is modified to [49]:

$$m = w \frac{(183.1221 - 0.5684T + 984.5679e^{\frac{w}{115.96277}})}{5610.5}$$
(3.2)

Where T is the temperature of the solution in K.

The conductivity of the electrolyte should be as high as possible for the minimization of the losses in the cell. Based on numerous experiments performed in the past, conductivity changes with weight fraction and temperature (see Fig. 3.1). As the temperature increases, the conductivity gets higher while there is optimum molarity, close to 30 wt%, to reach the highest conductivity for a specific temperature.

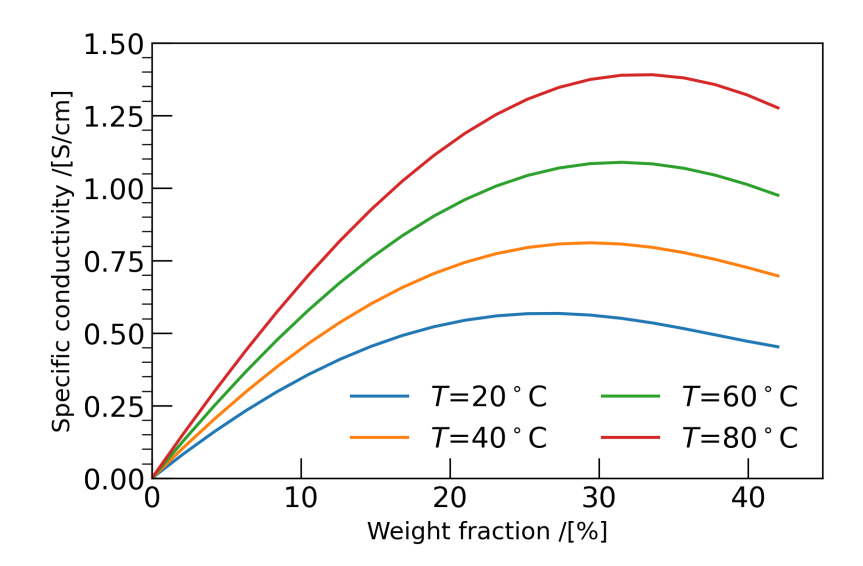


Figure 3.1: Specific conductivity of KOH solution with KOH weight fraction for different temperatures at atmospheric pressure. Specific conductivity is enhanced with temperature and its maximum value is observed for weight fractions between 25% to 35%.

For modeling purposes, it is requisite to use an empirical equation that accurately predicts the conductivity of the electrolyte for different temperatures and concentrations. In our case, the following relation [38] is used:

$$k_{\text{ele}} = K_1 m - K_2 m^2 + K_3 (m \cdot T) + K_4 \left(\frac{m}{T}\right) + K_5 m^3 - K_6 (m^2 \cdot T^2)$$
 (3.3)

Where k_{ele} is the specific conductivity in S/cm, m is the morality in mol/L, K_{i} are empirical constants, and T is the temperature in K.

Inside a common electrolysis cell, the electrolyte takes up most of the volume so it can be understood that the thermal behavior of the cell depends on the thermal and momentum properties of the electrolyte. In particular, the constant-pressure specific heat [57] is expressed as follows:

$$c_{\text{p,ele}} = K_1 + K_2 \cdot \ln(t/100) + \left(K_3 + K_4 \cdot \frac{w}{100} + 8t\right) \cdot \frac{w}{100}$$
 (3.4)

Where $c_{\text{p,ele}}$ is the constant-pressure specific heat in J/kg K, K_i are empirical constants, and t is the temperature in °C.

Furthermore, the density and dynamic viscosity of the electrolyte are described by the empirical relations [57] below:

$$\rho_{\text{ele}} = (K_1 t^2 + K_2 t + K_3) \cdot \exp\left(K_4 \cdot \frac{w}{100}\right) \tag{3.5}$$

$$\mu_{\text{ele}} = K_1(K_2 + t) - K_3 + 10^{(K_4 \cdot \frac{w}{100} + K_5 \cdot t \cdot \frac{w}{100})}$$
(3.6)

Where $\rho_{\rm ele}$ is the density in kg/m³, $\mu_{\rm ele}$ is the dynamic viscosity in Pa·s, w is the mass fraction of KOH (in %), $K_{\rm i}$ are empirical constants, and t is the temperature in °C. Although $\rho_{\rm ele}$ is introduced in Eq. 3.2, it is used only for the calculation of the molarity. For any other purpose, Eq. 3.5 is used. Nonetheless, both equations yield the same results.

The table below summarizes the empirical constants for each equation.

-	K_1	K_2	K_3	K_4	K_5	K_6
$k_{\rm ele}({ m S/cm})$	-2.041	-0.0028	0.005332	207.2	0.001043	-0.0000003
$\mu_{\rm ele}({\rm Pa\cdot s})$	$5.98 \cdot 10^{-1}$	$4.33 \cdot 10$	1.54	1.12	$2.03 \cdot 10^{-3}$	-
$ ho_{ m ele}({ m kg/m^3})$	$-3.25 \cdot 10^{-3}$	$1.11 \cdot 10^{-1}$	$1.00171 \cdot 10^3$	$8.6 \cdot 10^{-1}$	-	-
$c_{\rm polo}({\rm J/kg~K})$	$4.236 \cdot 10^3$	1.075	$-4.831 \cdot 10^3$	8	-	-

Table 3.1: Empirical constants for the electrolyte properties.

3.1.2 Reversible potential

As it is already mentioned in the previous chapter, the thermodynamic minimum energy for the electrolysis of water is a function of temperature and pressure. For the calculation of the total voltage applied to the cell, it is important to know how the reversible potential varies with the process conditions. This will indicate the share of the minimum energy consumption and the losses involved during the process.

The reversible potential at standard pressure (1 bar) is expressed as a function of temperature by the following equation [32]:

$$U_{\text{T.Po}}^{\text{rev}} = 1.50342 - 9.956 \cdot 10^{-4} T + 2.5 \cdot 10^{-7} T^2$$
(3.7)

Where U_{T,P_0}^{rev} is in Volts and T is the temperature in K.

In real applications, the pressure inside the cell can be way higher than the atmospheric, hence it is useful to express the reversible potential as a function of pressure and temperature. An accurate relation found in the literature that takes also into account the non ideality of the product gases is shown below [30].

$$U_{\rm T,P}^{\rm rev} = U_{\rm T,P_0}^{\rm rev} + \frac{RT}{nF} \ln \left((P - P_{\rm w})^{1.5} \frac{P_{\rm w}^*}{P_{\rm w}} \right) + (P - P_{\rm w}) \left(21.661 \cdot 10^{-6} - \frac{5.471 \cdot 10^{-3}}{T} \right) + (P - P_{\rm w})^2 \left(-\frac{6.289 \cdot 10^{-6}}{T} + \frac{0.135 \cdot 10^{-3}}{T^{1.5}} + \frac{2.547 \cdot 10^{-3}}{T^2} - \frac{0.4825}{T^3} \right)$$
(3.8)

Where $U_{\rm T,P}^{\rm rev}$ is in Volts, $R=8.3144~{\rm m}^3$ Pa K⁻¹ mol⁻¹ is the universal gas constant, n is the number of electrons transferred, F=96485 C/mol, $P_{\rm w}$ is the partial pressure of KOH solution, $P_{\rm w}^*$ is the partial pressure of pure water and P is the pressure of the system in bar.

The partial pressure of pure water and KOH solution is expressed as follows [31]:

$$P_{\rm w}^* = T^{-3.4159} \exp\left(37.043 - \frac{6275.7}{T}\right) \tag{3.9}$$

$$P_{\rm w} = T^{-3.498} \exp\left(37.93 - \frac{6426.32}{T}\right) \cdot \exp(0.016214 - 0.13082m + 0.1933m^{0.5}) \quad (3.10)$$

In the equations above, $P_{\rm w}^*$ and $P_{\rm w}$ are in bar, T is the temperature in K and m is the molarity in mol/L.

3.1.3 Thermoneutral voltage

The thermoneutral voltage is the limit above which heat generation inside the cell takes place and the temperature starts to increase. The amount of heat produced is dictated by the difference between the cell voltage and the thermoneutral voltage and its value changes with pressure and temperature. During operation, as the cell temperature starts to increase the amount of generated heat changes as well.

The variation of the thermoneutral voltage with temperature and pressure is described below [30]:

$$U_{\rm t,P}^{\rm tn} = 1.4756 + 2.252 \cdot 10^{-4}t + 1.52 \cdot 10^{-8}t^2 + 1.5 \frac{P_{\rm w}}{nF(P-P_{\rm w})} \cdot (42960 + 40.762t - 0.06682t^2) + f(T,P) \quad (3.11)$$

Where $U_{\rm t,P}^{\rm tn}$ is the thermoneutral voltage in Volts, t is the temperature in °C and f is a correction function that takes into account the difference in voltage between ideal gas assumption and real gas considerations.

For the correction function f, the following equation [30], as a function of pressure and temperature is used:

$$f(T,P) = \left(21.661 \cdot 10^{-6} - \frac{10.941 \cdot 10^{-3}}{T}\right)P + \left(\frac{-18.578 \cdot 10^{-6}}{T} + \frac{0.339 \cdot 10^{-3}}{T^{1.5}} + \frac{7.845 \cdot 10^{-3}}{T^2} - \frac{1.659}{T^3}\right)P^2 \quad (3.12)$$

Where T is the temperature in K and P is the pressure in bar.

3.2 Electrochemical model

For the modeling of the electrochemical effects that take place in the cell and ultimately the derivation of the polarization curve, each component must be modeled separately to account for its contribution to the total energy losses. In this section, a comprehensive description of all the necessary equations for the modeling of the membrane, electrodes, and the electrolyte is presented.

The voltage that has to be applied to the cell should be at least the thermodynamic minimum required in addition to the voltage drop due to energy losses. Therefore,

$$U_{\rm c} = U_{\rm T,P}^{\rm rev} + (\eta_{\rm act}^{\rm an} + \eta_{\rm act-\theta}^{\rm an}) + (\eta_{\rm act}^{\rm c} + \eta_{\rm act-\theta}^{\rm c}) + (R_{\rm m} + R_{\rm Ni/SS} + R_{\rm KOH}) \cdot I$$
 (3.13)

Where U_c is the total cell voltage, $U_{\rm T,P}^{\rm rev}$ is the reversible voltage, $\eta_{\rm act}^{\rm an}$ is the activation overpotential at the anodic surface, $\eta_{\rm act}^{\rm c}$ is the activation overpotential at the cathodic surface, $\eta_{\rm act-\theta}^{\rm an}$ and $\eta_{\rm act-\theta}^{\rm c}$ is the additional activation overpotential in Volts due to bubble coverage of the anode and cathode, respectively. Moreover, $R_{\rm m}$, $R_{\rm Ni/SS}$, and $R_{\rm KOH}$ are the ohmic losses due to the membrane, stainless-steel or Nickel electrode, and electrolyte expressed in Ω . Lastly, I is the current of the cell in Amps.

3.2.1 Ohmic losses

The ohmic losses obey Ohm's law and are responsible for the energy dissipation of the membrane, electrode, and electrolyte.

Membrane As has been already underlined in the previous chapter, the role of the membrane is to separate the products of each compartment and allow the movement of the ions from one side of the cell to the other. The electrical conductivity of the membrane depends on many factors such as porosity, tortuosity, and thickness while the material also plays a significant role in the general properties of the membrane. In the past, asbestos was the main membrane material for alkaline electrolysers, but due to its hazardous properties to human health, its use was stopped. Common materials for the

PEM and AWE electrolysers are the Nafion and Zirfon, respectively, while new materials like oxide of ceramics and polymers are tested to lower the ohmic losses [58]. Tab. 3.2 summarizes various membrane materials and their properties.

Table 3.2: Separator materials for alkaline electrolysers. Oxide membrane materials show superior properties owing to lower specific resistance, smaller thickness, and higher operating temperature. Data obtained from Refs. [58].

Material	Temperature [°C]	Thickness [µm]	Spec. resistance $[\Omega \text{ cm}^2]$
Asbestos/polymer-bound asbestos	<100	2000-5000/200-500	0.74/0.15-0.2
PTFE-bound potassium titanate	120-150	300	0.1-0.15
Polymer-bonded zirconium oxide	< 160	200-500	0.25
Ceramic/oxide nickel materials	<170	25-50	0.07-0.1

For the current model, a general equation is used for the description of the electrical resistance and it can be implemented for different materials depending on their physical characteristics. Such an equation is shown below [59].

$$R_{\rm m} = \frac{1}{k_{\rm ele}} \cdot \frac{\tau_{\rm s}^2 \delta_{\rm s}}{\omega_{\rm s} \varepsilon_{\rm s} A_{\rm s}} \tag{3.14}$$

Where $k_{\rm ele}$ is the conductivity of the electrolyte (Eq. 3.3) in S/cm, $\tau_{\rm s}$ is the tortuosity, $\delta_{\rm s}$ is the thickness in cm, $\omega_{\rm s}$ is the wettability, $\varepsilon_{\rm s}$ is the porosity and $A_{\rm s}$ is the surface of the separator, in cm².

In most cases, the manufacturer provides the porosity and thickness of the membrane. On the contrary, tortuosity and wettability are parameters that demand specific tests for their determination and usually are not performed. Therefore, a theoretical approach can be followed for the calculation of the membrane's tortuosity. In specific, the membrane's degree of crystallinity is correlated to its tortuosity. The degree of crystallinity denotes the fraction of a material's structural order, which strongly affects its properties. A high degree of crystallinity in a polymer indicates more regularly aligned chains. The following equation indicates this correlation [60]:

$$\ln(\tau_{\rm s}) = -n_{\rm m} \cdot \ln(\alpha_{\rm am}) \tag{3.15}$$

Where $n_{\rm m}$ is the slope and $\alpha_{\rm am}$ is the degree of amorphousness. In fact, $\alpha_{\rm am}$ is equal to 1- $\alpha_{\rm cr}$, with $\alpha_{\rm cr}$ denoting the degree of crystallinity.

On the other hand, wettability expresses the ability of the material to maintain contact surface with liquid or, equivalently, the tendency of a liquid to spread on a solid surface. For instance, a hydrophilic material has a large contact area with water resulting in pores totally filled with electrolyte. By contrast, hydrophobic ones lead to pores that are not filled with electrolyte and allow gas to permeate them. Unfortunately, there is not any relation regarding the wettability of membranes since its value depends on many parameters. Nevertheless, for modeling purposes, a reasonable estimation will be given.

Electrolyte The volume of the electrolyte that is dictated by the distance between the electrodes and their height leads to a voltage drop inside the cell. It is apparent that the greater the distance, the larger the losses. New cell configurations are structured in a nearly-zero gap or zero-gap configuration where the voltage losses due to electrolyte are minimized. The voltage drop due to the electrolyte obeys Ohm's law, which means it is linear with the distance between the electrodes. The exact calculation is formulated as shown below [29]:

$$R_{\text{KOH}} = \frac{1}{k_{\text{ele}}} \left(\frac{d_{\text{am}}}{A_{\text{a}}} + \frac{d_{\text{cm}}}{A_{\text{c}}} \right) \tag{3.16}$$

Where R_{KOH} is the resistance of the pure electrolyte (no bubbles) in Ω , k_{ele} is the conductivity of the electrolyte as described in Eq. 3.3, d_{am} and d_{cm} is the distance between anode and cathode from the membrane in cm, respectively. A_{a} and A_{c} is the anodic and cathodic electrolyte area in cm².

Bubbles The gas bubbles that are generated on the surface of the electrodes, detach and scatter inside the electrolyte volume. Therefore, they block the path of ions and increase the voltage drop inside the electrolyte. There are many empirical relations found in the literature that attempt to calculate the conductivity of the electrolyte-bubble mixture, but most of them do not take into account the type of the electrode. The majority represents flat plate electrodes while for perforated ones there is not enough work done. The benefit of utilizing perforated electrodes is the fact that bubbles can escape from the back reducing their volume inside the electrolyte and hence lowering the ohmic losses. The bubble volume fraction in the electrolyte increases with the electrode height and decreases with the gap between the anode and the cathode due to the difficulty of the bubbles to escape from the cell. On the other hand, high electrolyte velocity favors their removal.

On flat plate electrodes, a common approach is to find the average volume fraction of the bubbles by applying a momentum balance between the cathode and the membrane [37]. After proper rearrangements, the following equation is deduced:

$$\overline{\alpha}_{c} = \frac{1}{4} \frac{RT}{P} \frac{IH}{AFdu_{b}} \tag{3.17}$$

For the anode-membrane gap, the average volume fraction is provided as follows:

$$\overline{\alpha}_{\rm a} = \frac{1}{8} \frac{RT}{P} \frac{IH}{AFdu_{\rm b}} \tag{3.18}$$

Where T is the temperature in Kelvin, P is the pressure in Pascals, and I is the current in Amps. In addition, H is the height of the electrode in m, A is the electrode surface area in m^2 , d is the electrode-membrane distance in m, and u_b is the bubble rising velocity in m/s.

Regarding the bubble rising velocity near the electrode, conditions such as pressure, temperature, current, and bubble diameter have a significant influence. Assuming that

the applicability of the ideal gas law is valid, the faraday's law, which is presented in a subsequent section, is introduced. Simultaneously, the effect of pressure is considered by including a correction factor. Thus, the following equation is derived for a natural buoyancy flow [61].

$$u_{\rm b} = \frac{zI}{nFdw_{\rm el}} \frac{RT}{P} \left(\frac{P}{P - P_{\rm w}} \right) \tag{3.19}$$

Where $u_{\rm b}$ is the bubble rising velocity in m/s, z is the coefficient of the gas in the balanced chemical reaction (Eq. 2.5), $w_{\rm el}$ is the width of the electrode in m, $P_{\rm w}$ is the electrolyte vapour pressure in Pa, and d is the electrode-membrane distance in m. In the present work, a homogeneous flow is assumed. This implies that the electrolyte-bubble mixture has a common velocity equal to the maximum between the natural buoyancy velocity and the electrolyte velocity in the channels.

The presence of bubbles in the electrolyte significantly increases its resistivity because they block the ions to travel from the anode to the cathode. An empirical relation about the conductivity of the bubble-electrolyte mixture is given by Bruggeman [30] and it is formulated as shown below

$$\frac{k_{\rm g}}{k_{\rm ele}} = (1 - \overline{\alpha}_{\rm a/c})^{1.5}$$
 (3.20)

Where $k_{\rm g}$ is the electrical conductivity of the bubbly electrolyte, $k_{\rm ele}$ is the electrical conductivity of the pure one, and $\overline{\alpha}_{\rm a/c}$ is the bubble average volume fraction in the anode or cathode. Hence, each compartment has different electrolyte conductivity. The consideration of the bubbles in the voltage drop calculation necessitates the replacement of $k_{\rm ele}$ in Eq. 3.16 with $k_{\rm g}$. Therefore, the ohmic drop due to electrolyte with bubbles is expressed as follows.

$$R_{\text{KOH}} = \frac{1}{k_{\text{g}}} \left(\frac{d_{\text{am}}}{A_{\text{a}}} + \frac{d_{\text{cm}}}{A_{\text{c}}} \right) \tag{3.21}$$

Electrodes The electrode material selection is crucial for the effectiveness of the reactions and the energy consumption to produce gases. Numerous studies have shown that noble metals like Iridium, Ruthenium, and Platinum as well as their oxides are considered the most effective for the OER and HER due to their high electrochemical activity. Nevertheless, the scarcity and the high cost of these materials lead to the quest for alternatives. Reasonable alternatives are the Nickel and Stainless Steel electrodes which are used as the main material for the alkaline electrolysers.

Contrary to their electrochemical activity, the electrical conductivity of both metals is high and the contribution to the total ohmic losses is negligible. In this work, for the sake of completeness, the resistivity of the electrodes is taken into account and is described by the following experimental equations [40, 62].

$$\rho_{\text{Ni}} = -1.21 \cdot 10^{-6} + 2.29 \cdot 10^{-8} T + 6.1 \cdot 10^{-14} T^3$$
(3.22)

$$\rho_{SS} = 9.843 \cdot 10^{-5} - 1.502 \cdot 10^{-7} T + 3.434 \cdot 10^{-10} T^2$$
(3.23)

Where $\rho_{\text{Ni/SS}}$ is the resistivity in $\Omega \cdot \text{cm}$ and T is the temperature in K. Hence, the ohmic resistance due to each electrode is obtained as follows:

$$R_{\text{Ni/SS}} = \rho_{\text{Ni/SS}} \cdot \left(\frac{L_{\text{Ni/SS}}}{S}\right)$$
 (3.24)

Where $R_{\text{Ni/SS}}$ is the ohmic resistance in Ω , $L_{\text{Ni/SS}}$ is the electrode thickness in cm and S is the active area of the electrode in cm², respectively.

3.2.2 Activation losses

The activation losses are associated with the electrochemical process that takes place at the surface of the electrode.

Electrode activation losses In alkaline electrolysers, the low current densities enable us to assume that the concentration of the electrolyte at the interface is the same as that of the bulk. The overpotential is high enough to neglect one of the exponentials of Eq. 2.17 therefore, the modeling of the activation losses will be approximated with the use of the Tafel equation (Eq. 2.19). The implementation of the Tafel equation necessitates the use of the exchange current density and the transfer coefficient. Their value depends on the electrode material, the temperature, and the type of reaction (OER or HER). For high accuracy, cyclic voltammetry experiments must be performed for the anode and cathode under various temperature conditions. In the literature, few experiments have been performed for different kinds of electrodes to determine the exchange current density and the transfer coefficient [63, 64, 65]. The values reported have a significant discrepancy between them due to experimental conditions such as the surface roughness factor of the electrode and the catalyst loading. Consequently, if individual experiments are not performed for a cell that is of particular interest, then data from the literature have to be used with a high chance to be modified to satisfy the characteristics of the cell under investigation.

The exchange current depends on the activation energy and the temperature of the reaction, and similar to the reaction rate, it is expressed as an Arrhenius-type equation. In addition, surface properties like specific area and loading indicate the active sites that influence the reaction rate. A general form of the exchange current density coefficient is provided by the following equation [26]:

$$i_0 = i_0^{\text{ref}} a_{\text{ct}} L_{\text{ct}} \left(\frac{P}{P_{\text{ref}}} \right)^{\gamma} \exp \left[-\frac{E_{\text{a}}}{RT} \left(1 - \frac{T}{T_{\text{ref}}} \right) \right]$$
(3.25)

Where i_0^{ref} is the exchange current density at reference conditions (298 K, 1 bar) in A/cm², a_{ct} is the catalyst specific area in cm² of catalyst area per mg of catalyst, L_{ct} catalyst loading in mg of catalyst per cm² of electrode area. T is the temperature in K, E_a is the

activation energy in J/mol, γ is the pressure dependency coefficient, and $P_{\rm ref}$, $T_{\rm ref}$ is the reference pressure and temperature in Pa and K, respectively. The product of $a_{\rm ct} \cdot L_{\rm ct}$ is called electrode roughness and indicates the catalyst area in cm² per electrode geometric area in cm². In our case, there is no catalyst used and for that reason the product is equal to 1.

The estimation of the exchange current density coefficient for each electrode is based on experimental data on pure Nickel and is a function of temperature. The relation for each electrode in atmospheric conditions is expressed as follows [65]:

$$i_{0,c} = 1.08 \cdot 10^{-5} \cdot \exp\left[-\frac{50000}{RT}\left(1 - \frac{T}{T_{\text{ref}}}\right)\right]$$
 (3.26)

$$i_{0,a} = 1.21 \cdot 10^{-6} \cdot \exp\left[-\frac{80000}{RT}\left(1 - \frac{T}{T_{\text{ref}}}\right)\right]$$
 (3.27)

Where $i_{0,a}$ is the exchange current density of the anode in A/cm², $i_{0,c}$ is the exchange current density of the cathode in A/cm², T is the temperature in K, and $T_{\text{ref}} = 298$ K is the reference temperature.

The exchange current density of the anode and cathode made of stainless steel (SS) and operating at atmospheric conditions is approximated through the expressions below [66]:

$$i_{0,a} = 1.72 \cdot 10^{-9} \cdot \exp\left[-\frac{50000}{RT}\left(1 - \frac{T}{T_{\text{ref}}}\right)\right]$$
 (3.28)

$$i_{0,c} = 1 \cdot 10^{-8} \cdot \exp\left[-\frac{50000}{RT} \left(1 - \frac{T}{T_{\text{ref}}}\right)\right]$$
 (3.29)

In both materials, the reference exchange current density is obtained after fitting the experimental data acquired in the XINTC Global laboratory.

Many models found in the literature assume that the transfer coefficient of the anode and cathode is equal to 0.5 (symmetry) without considering the temperature effects. In reality, similar to the exchange current density, it depends not only on the temperature but also on the electrode surface properties. For that reason, experimental data have been used to derive an empirical relation for Nickel electrodes. This relation for both electrodes is given below [29].

$$\alpha_{\rm c} = 0.1175 + 0.00095T \tag{3.30}$$

$$\alpha_{\rm a} = 0.0675 + 0.00095T \tag{3.31}$$

In the equations above, α_c and α_a are the transfer coefficients for the cathode and anode respectively, while T is the temperature in K.

On the contrary, the anodic and cathodic transfer coefficients of the stainless-steel electrode fluctuate between 0.4 and 0.5, according to the literature [66, 67].

Bubble activation losses During the operation of the electrolyser, oxygen and hydrogen bubbles start to develop on the surface of the electrodes, and as more products are being generated the bubbles grow in size and cover a larger surface area. After the size becomes large enough, buoyancy drives the bubbles upwards detaching them from the electrode surface. Part of the electrode is rendered inactive due to the bubble coverage leading to a higher voltage drop.

The real current density that is used in the Tafel equation is expressed as follows:

$$i = \frac{I}{A(1-\theta)} \tag{3.32}$$

The electrode bubble coverage, θ , depends on many factors such as temperature, pressure, current density, and surface characteristics. A widely used equation found in the literature is derived from experimental data and is described below [48]:

$$\theta = \left[-97.25 + 182 \left(\frac{T}{T_{\text{ref}}} \right) - 84 \left(\frac{T}{T_{\text{ref}}} \right)^2 \right] \cdot \left(\frac{i}{i_{\text{lim}}} \right)^{0.3} \cdot \left(\frac{P}{P - P_{\text{w}}} \right)$$
(3.33)

Where T is the temperature of the cell in K, $T_{\rm ref}=300K$ is the reference temperature, i is the current density in A/cm², $i_{\rm lim}=30$ A/cm² is the limiting current density [44], P is the pressure of the system in bar, and $P_{\rm w}$ is the vapor pressure of KOH solution, in bar.

3.2.3 Efficiency

The research community is focused on improving the efficiency of the alkaline electrolyser and thus making its wide deployment more profitable. It has been mentioned that the efficiency of the electrolyser is the product of the voltaic and faradaic efficiency (Eq. 2.20), so during the investigation of the system, both parts have to be considered. The connection of the electrolyser with a renewable source leads to cell temperature changes with the current profile, thus altering the efficiency of the system.

Based on Eq. 2.21 and the analysis of the cell losses so far, the voltaic efficiency is higher at elevated temperatures. In addition, Eq. 3.11 and Fig. 2.3 indicate that a temperature increase yields higher voltaic efficiency due to the increase of the thermoneutral voltage. Consequently, for the calculation of the voltaic efficiency Eq. 2.21, Eq. 3.11, and Eq. 3.13 will be implemented.

On the other hand, the faradaic efficiency indicates the current losses due to shunt currents that reduces with temperature. The figure below (Fig. 3.2) is based on experimental data of the HYSOLAR-project electrolyser connected to a solar panel. It is obvious that at low current densities the proportion of losses to the total current is high and the efficiency deteriorates with temperature. The calculation of the faradaic efficiency is deduced from experiments by measuring the mass flow of the products at the exit of the electrolyser and dividing it by the theoretical amount.

In the literature field, it is suggested that the faradaic efficiency is satisfied by the following empirical relation, and it is a function of temperature and current density [56].

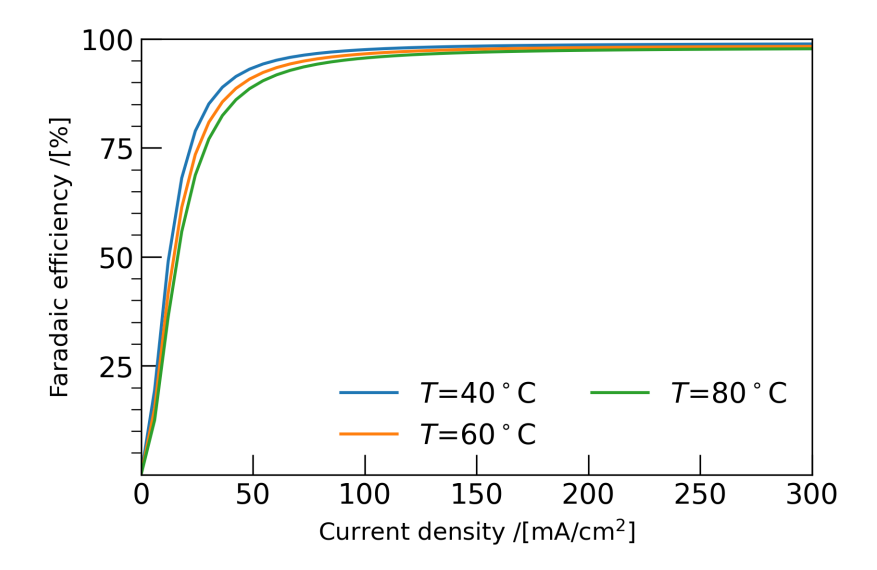


Figure 3.2: Faradaic efficiency of the HYSOLAR-project electrolyser for three different temperatures at ambient pressure. High efficiency is achieved at current densities greater than 50 mA/cm^2 . Increasing temperature lowers the faradaic efficiency owing to the gas crossover and the shunt current in the stack that reduce with increasing gas production. Figure reproduced from Refs. [45, 56].

$$\eta_{\rm F} = \left(\frac{i^2}{f_{11} + f_{12}t + i^2}\right) \cdot (f_{21} + f_{22}t) \tag{3.34}$$

Where i is the current density in mA/cm² and t is the temperature in °C. The empirical constant are f_{11} =50, f_{12} =2.5, f_{21} =1, and f_{22} = -2.5·10⁻⁴

3.2.4 Molar flow of products

One important aspect of the electrolyser is the production capacity for specific energy consumption where the molar flows of hydrogen and oxygen gases are proportional to the current applied to the cell. As already mentioned in the previous section, part of the applied current ends up as parasitic losses and does not lead to useful products. When the operating conditions are close to the boiling point of the electrolyte, a non-negligible amount of water vapor is produced leaving the system in a mixed state with the main products. The production of vapor is not desirable because the system consumes additional energy, and this is the enthalpy of vaporization.

The molar flow rate of the products is given by Faraday's law [26] and is formulated as:

$$\dot{n}_{\rm H_2} = \frac{I}{2F} \cdot \eta_{\rm F} \tag{3.35}$$

$$\dot{n}_{\rm O_2} = \frac{I}{4F} \cdot \eta_{\rm F} \tag{3.36}$$

$$\dot{n}_{\rm H_2O} = \frac{I}{2F} \cdot \eta_{\rm F} \tag{3.37}$$

Where $\dot{n}_{\rm H_2}$, $\dot{n}_{\rm O_2}$, and $\dot{n}_{\rm H_2O}$ are the molar flow rates of hydrogen,oxygen, and water consumed in mol/s and I is the current of the cell in Amps.

The molar flow of water vapor, as described below, depends on the pressure of the system and the molar flow of the product gases.

$$\dot{n}_{\rm v} = \frac{P_{\rm w}}{P - P_{\rm w}} \cdot (\dot{n}_{\rm H_2} + \dot{n}_{\rm O_2}) \tag{3.38}$$

As the temperature increases, the saturation pressure of the electrolyte increases as well. This results in a high water vapor content in the products, hence the rationale is to operate under low temperatures (50-80 °C) or high pressures (5-30 bar).

3.3 Thermal model

In this project, the thermal modeling is approached by a lumped capacitance model where a uniform temperature profile is assumed inside the electrolyser and temperature gradients are ignored [68].

3.3.1 Stack

The assumption of uniform temperature is considered reasonable because the conduction taking place inside the electrolyser is faster compared to convection between it and the environment. It has been already stressed that the operating temperature plays a significant role in the energy consumption of the cell and the efficiency of the system, thus it is important to be investigated for a more holistic approach.

The energy and mass balance applied on a single cell can be easily extended for a stack with N number of cells. Considering the electrolyser as the system under examination (Fig. 3.3), the first law of thermodynamics for reactive systems is applied considering all the inflows, outflows, and heat losses that occur [69].

After simplifications, the stack's thermal balance is formulated as follows (see section A.1):

$$C_{\rm t} \frac{dT_{\rm stack}}{dt} = \dot{Q}_{\rm gen} - \dot{Q}_{\rm liq} - \dot{Q}_{\rm amb} \tag{3.39}$$

• The term C_t represents the constant-pressure overall thermal capacitance of the electrolyser by taking into account the volume and density of all the individual

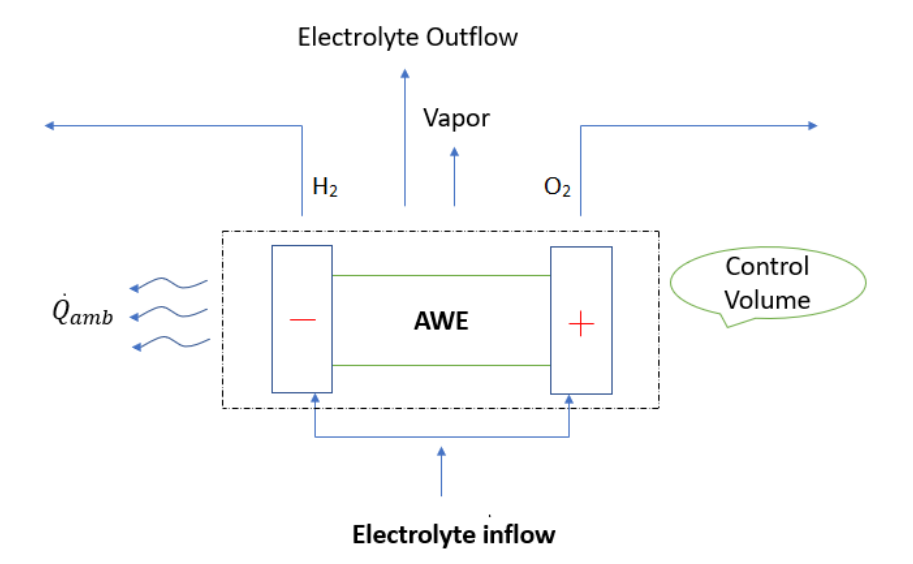


Figure 3.3: Control volume for the thermal balance. The heat generation inside the stack due to ohmic losses, the heat abduction due to the temperature difference with the environment, and the inflow-outflow of electrolyte and gas products dictate the thermal response of the system.

parts of the assembly [47]. Hence, it can be estimated as:

$$C_{\rm t} = \left(\sum_{i} \rho_{\rm i} \cdot c_{\rm p_i} \cdot V_{\rm i}\right) N_{\rm cell} \tag{3.40}$$

Where ρ_i , c_{p_i} and V_i are the density, constant-pressure specific heat capacity, and volume of each element of the cell. In addition, N_{cell} indicates the number of cells inside the electrolyser.

• The term $\dot{Q}_{\rm gen}$ signifies the generation of heat and is the driving force for the temperature changes inside the electrolyser. The equation below is used for the description of the term.

$$\dot{Q}_{\text{gen}} = I(U_{\text{c}} - U_{\text{t.P}}^{\text{tn}}) N_{\text{cell}} \tag{3.41}$$

It is comprehensible that heat generation is affected by the voltage and the temperature change inside the cell since both $U_{\rm t,P}^{\rm tn}$ and $U_{\rm c}$ are a function of temperature.

• The term $\dot{Q}_{\rm liq}$ denotes the energy that enters and leaves the system due to the inflow/outflow of fresh electrolyte and the outflow of gas products. The corresponding expression is shown below:

$$\dot{Q}_{\text{liq}} = \dot{m}_{\text{ele,in}} \cdot c_{\text{p,ele}} (T_{\text{stack}} - T_{\text{in}}) + N_{\text{cell}} \cdot \dot{m}_{\text{v}} h_{\text{lg}}$$
(3.42)

Where $\dot{m}_{\rm ele,in}$ is the mass flow of electrolyte coming into the system, $\dot{m}_{\rm v}$ is the mass flow of vapor leaving the system, $T_{\rm stack}$ is the temperature inside the electrolyser, $T_{\rm in}$ is the temperature of the electrolyte at the inlet of the stack, $h_{\rm lg}$ is the enthalpy of phase change of pure water, and $c_{\rm p,ele}$ is the constant-pressure specific heat capacity of the electrolyte.

• The term $\dot{Q}_{\rm amb}$ represents the heat losses to the environment due to the temperature difference between the surface of the electrolyser and the ambient. The main mechanisms to be considered are convection and radiation, therefore the equation to be used is the following:

$$\dot{Q}_{\rm amb} = \sigma A_{\rm stack} e (T_{\rm stack}^4 - T_{\rm amb}^4) + \overline{h}_{\rm stack} A_{\rm stack} (T_{\rm stack} - T_{\rm amb})$$
(3.43)

Where $\sigma=5.67\cdot 10^{-8}$ W m⁻² K⁻⁴ is the Stefan-Boltzmann constant, $A_{\rm stack}$ is the surface area of the electrolyser in m², e is the emissivity of the outer material of the stack, $\overline{h}_{\rm stack}$ is the average heat transfer coefficient in W/m² K, and $T_{\rm amb}$ is the ambient temperature.

The coefficient $\bar{h}_{\rm stack}$ depends on many factors such as temperature difference, stack shape, and velocity of the ambient air. In most cases, the stack has a cylindrical or rectangular shape that affects the heat losses differently. A rectangular shape can be approximated as an object with two horizontal and four vertical plates. With that being said, the average heat transfer coefficient in natural convection for a vertical plate is given as follows:

$$\overline{h}_{\text{natural}} = \frac{k_{\text{air}}}{L} \left[0.68 + 0.670 (Ra_{\text{L}} \cdot \Psi)^{1/4} \right]$$
(3.44)

Where Rayleigh number, $Ra_{\rm L}$, is defined as:

$$Ra_{\rm L} = \frac{\beta g \Delta T L^3}{\nu \alpha_{\rm air}} \tag{3.45}$$

and the parameter Ψ as

$$\Psi = \left[1 + \left(\frac{0.492}{Pr} \right)^{9/16} \right]^{-16/9} \tag{3.46}$$

In the equations above, L is the characteristic length of the plate, Pr is the Prandtl number and β is the thermal expansion coefficient of air. The parameter g is the gravity, ν and $\alpha_{\rm air}$ are the kinematic viscosity and thermal diffusivity of air, $k_{\rm air}$ is the thermal conductivity of the air, and ΔT is the temperature difference between air and the stack's surface.

For a horizontal plate, the average heat transfer coefficient for natural convection is provided in the following manner:

$$\overline{h}_{\text{natural}} = \frac{k_{\text{air}}}{L} \left(0.14 \cdot Ra_{\text{L}}^{1/3} \right) \tag{3.47}$$

In real applications, the surrounding air of the system may not be quiescent, thus leading to additional heat losses. Therefore, besides natural convection, also forced convection takes place. In such cases, it is reasonable to consider mixed convection for an accurate calculation of the heat transfer coefficient.

The average heat transfer coefficient for a laminar flow over a flat plate is obtained as follows:

$$\overline{h}_{\text{forced}} = (\frac{k_{\text{air}}}{L}) \cdot 0.664 (Re_{\text{L}}^{1/2}) (Pr^{1/3})$$
 (3.48)

Where $Re_{\rm L}$ is the Reynolds number over a flat plate.

Mixed convection for a rectangular electrolyser is approximated as follows [70]:

$$\overline{Nu_{\text{mixed}}}^{7/2} = \overline{Nu_{\text{natural}}}^{7/2} + \overline{Nu_{\text{forced}}}^{7/2}$$
(3.49)

Where $\overline{Nu}_{\text{mixed}}$, $\overline{Nu}_{\text{natural}}$, $\overline{Nu}_{\text{forced}}$ and is the average Nusselt number for mixed, natural, and forced convection.

3.3.2 Separators

An important component of the production system is the hydrogen and oxygen gas separator due to their main objective of separating the gaseous products from the electrolyte. The gaseous products go to the purification system, while the electrolyte is recirculated back to the stack, therefore, the thermal behavior of the separator is significantly affecting the stack's operating conditions. Concomitantly, demineralized feed water is used to refill the electrolyte that is consumed to produce H_2 , O_2 , and vapor.

A lumped capacitance model is applied for the thermal modeling of the separator assuming that the temperature gradients inside it are negligible. In addition, any concentration gradient that may exist in the electrolyte is considered minor and impotent to affect the thermal response.

The control volume under investigation is the separator itself and is depicted in the figure below (Fig. 3.4). The description of the separator's thermal model is formulated on the 1st law of thermodynamics by incorporating the mass balance and introducing simplifications (see section A.3) that yields the same equation as Eq. 3.39. In this case, each term denotes:

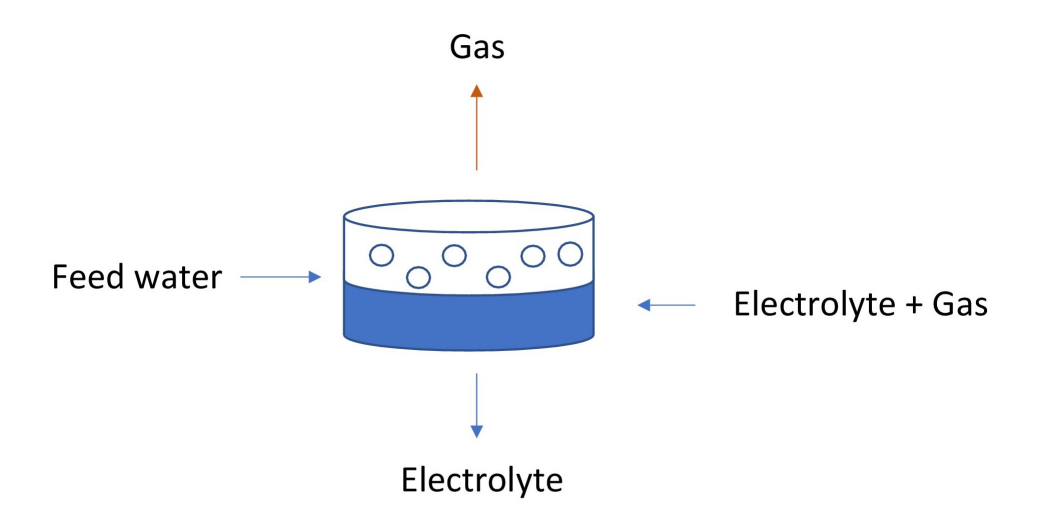


Figure 3.4: Illustration of the gas separator. The electrolyte-gas mixture coming from the stack, enters the tank to separate into pure electrolyte and gas bubbles. Pure electrolyte recirculates back to the stack while gas is sent to the purification system. Simultaneously, feed water is inserted to replenish the consumed water.

- The term $C_{\rm t,sep}$ represents the constant-pressure overall thermal capacity of the separator by taking into account the volume and density of the electrolyte and the gaseous product. The estimation of it is based on Eq. 3.40
- The term $\dot{Q}_{\rm gen}$ is absent in this case since there is no heat generation inside the separators.
- The term \dot{Q}_{liq} denotes the energy that enters and leaves the system due to the inflow/outflow of fresh electrolyte and gas products:

$$\dot{Q}_{\text{liq}} = \dot{m}_{\text{mix}}(g) \cdot c_{\text{p,gas}} \cdot (T_{\text{sep}} - T_{\text{in}}) + \dot{m}_{\text{mix}}(l) \cdot c_{\text{p,ele}} \cdot (T_{\text{sep}} - T_{\text{in}}) + \dot{m}_{\text{f}} \cdot c_{\text{p,water}} \cdot (T_{\text{sep}} - T_{\text{f}})$$

$$(3.50)$$

Where $\dot{m}_{\rm mix}(g)$ is the mass flow of the gaseous product that leaves the stack together with the electrolyte in a mixed form, while $\dot{m}_{\rm mix}(l)$ is the liquid part of this mixture (electrolyte). Both parts enter the control volume at temperature $T_{\rm in}$. The mass flow of the feed water replenishing the consumed water is denoted by $\dot{m}_{\rm f}$ and enters the system at temperature $T_{\rm f}$. Frequently, the feed temperature is set equal to the ambient temperature. Nonetheless, the feed water inflow is included in the energy and mass balance for sake of completeness since our experimental setup has not feed inflow. This will not affect the steady state condition assumed in the mass balance since the mass of water consumed for less than 7 hours of experimental time is lower than 2.5% of the total electrolyte mass in the system. In addition,

 $c_{\rm p,gas}$, $c_{\rm p,ele}$, and $c_{\rm p,water}$ express the constant-pressure specific heat capacity of gas product (H₂ or O₂ with vapor), electrolyte, and demi-water, respectively. $T_{\rm sep}$ is the temperature of the separator.

• An unavoidable part of every energy system are the heat losses to the environment, $\dot{Q}_{\rm amb}$, and in this case, these are represented by the losses through the walls of the separator. The average heat transfer coefficient for a horizontal cylinder is provided by the equation below [70]:

$$\overline{h}_{\text{natural}} = \frac{k_{\text{air}}}{D} \cdot \left(0.36 + \frac{0.518 R a_{\text{D}}^{0.25}}{[1 + (0.559/Pr)^{9/16}]^{4/9}} \right)$$
(3.51)

Where $\overline{h}_{\text{natural}}$ is the average heat transfer coefficient in natural convection, k_{air} is the thermal conductivity of air and D is the diameter of the cylindrical separator.

As stated before, ambient conditions can potentially create a state of mixed convection that must be considered. By using the heat transfer coefficient for forced convection found in the literature [70], the mixed convection heat transfer coefficient is provided by the expression below.

$$(\overline{Nu}_{\text{mixed}} - 0.3)^3 = (\overline{Nu}_{\text{natural}} - 0.3)^3 + (\overline{Nu}_{\text{forced}} - 0.3)^3$$
 (3.52)

Where $\overline{Nu}_{\text{mixed}}$, $\overline{Nu}_{\text{natural}}$, $\overline{Nu}_{\text{forced}}$ and is the average Nusselt number for mixed, natural, and forced convection.

3.4 Entropy balance

The first law of thermodynamics indicates the conservation of energy in a system without providing additional information about the maximum achievable efficiency. With that being said, the second law analysis is imperative for the identification of the irreversibilities involved in the system. In light of a steady-state approach, the second law can be applied only when the stack has reached a constant temperature.

Considering the same control volume for the stack, the entropy balance, after rigorous calculations (see section A.2), is formulated in the following way:

$$0 = \dot{m}_{\rm ele,in} \cdot (s_{\rm ele,in} - s_{\rm ele,out}) - N_{\rm cell} \cdot \dot{m}_{\rm v} \cdot s_{\rm lg} + N_{\rm cell} \cdot I \cdot \frac{U_{\rm T,P}^{\rm rev} - U_{\rm t,P}^{\rm tn}}{T_{\rm stack}} + \dot{S}_{\rm gen} - \frac{\dot{Q}_{\rm amb}}{T_{\rm stack}}$$
(3.53)

Where $s_{\text{ele,in}}$, and $s_{\text{ele,out}}$ are the specific entropy of the electrolyte at the inlet and outlet of the stack, respectively. Additionally, s_{lg} is the specific entropy of water's phase change, while \dot{S}_{gen} is the generated entropy due to the irreversibility of the system. The term T_{stack} refers to the temperature of the stack at the boundary with the environment,

but due to the lumped capacitance hypothesis, this value is equal to the temperature of the stack calculated by the 1st law (see Eq. 3.39).

The calculation of the generated entropy, as shown in the equation above, indicates the current at which the system operates more efficiently considering the mass flows into the system and the energy needed for the reaction to take place. Furthermore, ohmic losses are indirectly included in the heat losses to the environment. In overall, the analysis allows attribution of losses to design and operating parameters.

4 Results

In this chapter, the experimental setup, and the main equipment in the laboratory is presented. In addition, the results of the experiments, regarding the electrochemical and thermal testing of the stack, are demonstrated and discussed for each case scenario.

4.1 Experimental setup

The production of hydrogen involves not only the electrolysis stack, which is the heart of the system, but also the gas separators, pumps, gas chromatograph, sensors, and valves that are necessary for a safe operation. A broad view of the lab can be seen in the figure below (Fig. 4.1). In the subsequent paragraphs, each component is briefly analyzed for a more comprehensive description of the process.

4.1.1 Pumps and vanes

The role of the pump is to circulate the electrolyte in the system at the desired rate and at the same time cool the stack, thus avoiding overheating. The current lab includes two magnetic impeller drive pumps with a polysulfone impeller casing and a stainless-steel head. Having 6.5 cm diameter and 16.5 cm length, the maximum flow rate is 19 L/min, and the nominal power is 25 W. The two pumps displace the electrolyte from each gas separator to the inlet of the stack's anode and cathode. Regarding the vanes, their role is to keep separated or allow the mixing of anolyte and catholyte before they are inserted to the stack. They operate electronically and their opening can be dictated in precise.

4.1.2 Sensors

The durability of the membrane prohibits the operation of the stack at temperatures above 70 °C. With that being said, sensors at the inlet/outlet of the stack as well as inside the separators are used to record the temperature every second. When the temperature exceeds the safety limit, the cooling circuit is activated. The temperature sensor is a Pt1000 probe, a Platinum resistance thermometer with a measuring principle based on the change of electrical resistance due to the temperature change. The sensor is characterized by a working range of 0 °C to 150 °C and an accuracy of \pm 0.2 °C.

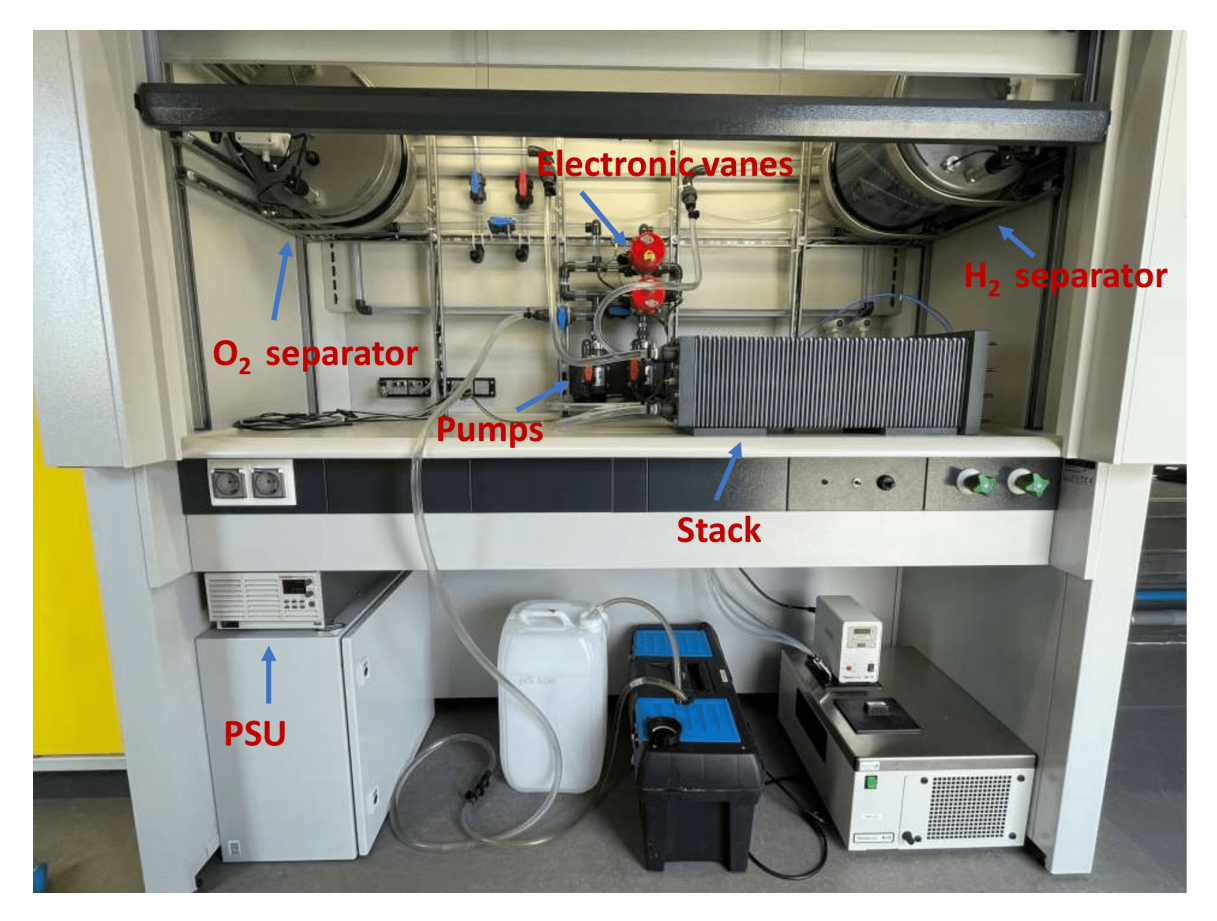


Figure 4.1: Experimental setup. The power supply unit (PSU) with maximum power of 760 W provides direct current (DC) to the stack. The two impeller-type pumps circulate the electrolyte in the system while the vanes ensure the mixing or separation of the analyte and catholyte. In the oxygen separator tank, analyte is separated from oxygen while in the hydrogen separator tank, catholyte is segregated from hydrogen gas.

4.1.3 Piping

The pipes are necessary for the transportation of the electrolyte-gas mixture from the stack to the gas separators and the return of the electrolyte back to the stack. The ones used in the experimental setup are made of PVC with a 17 mm outer diameter and 2 mm wall thickness. The total pipe length in the system is 5 m.

4.1.4 Gas chromatograph

It is known that when hydrogen reacts with oxygen at the right proportions, an explosion takes place. A common cause is the diffusivity of the product gases through the membrane inside the cell that leads to the migration of oxygen and hydrogen to other compartments and later on to the gas separator. When the concentration approaches



Figure 4.2: Magnetic impeller drive pump. Each pump is 25 W, has a maximum flow rate of 19 L/min, and circulates the anolyte/catholyte from the gas tank to the stack. The pump has a 6.5 cm diameter and 16.5 cm length.

the lower explosion limit (LEL), the operation of the system is shut down for safety purposes. Subsequently, the gas chromatograph Thermo Scientific Trace 1300 is installed to monitor the gas concentration by taking samples every 5mins both from the hydrogen and oxygen gas separator and analyzing them. The sample is injected with a syringe into the device while at the same time helium gas is inserted as the gas carrier for faster analysis times. The operating temperatures of the device are 5 °C to 400 °C, pressures up to 100 bar, and a resolution of 0.1 °C.

4.1.5 Gas separators

In the present configuration, the gas separators are PVC horizontal cylinders as can be seen in the figure below (Fig. 4.3). The hydrogen separator has a diameter of 31 cm, length of 40 cm, and volume of 32 L. The oxygen separator tank has a 31 cm of diameter, 20 cm length, and 16 L volume emphasizing the 2:1 ratio of gas production in the stack. Inside the tanks, the spiral tubes are utilized for the circulation of cooling or heating water during the overheating or the startup of the system. The temperature, pressure, and level sensors ensure proper conditions and prevent the flooding or emptying of the tank with electrolyte.

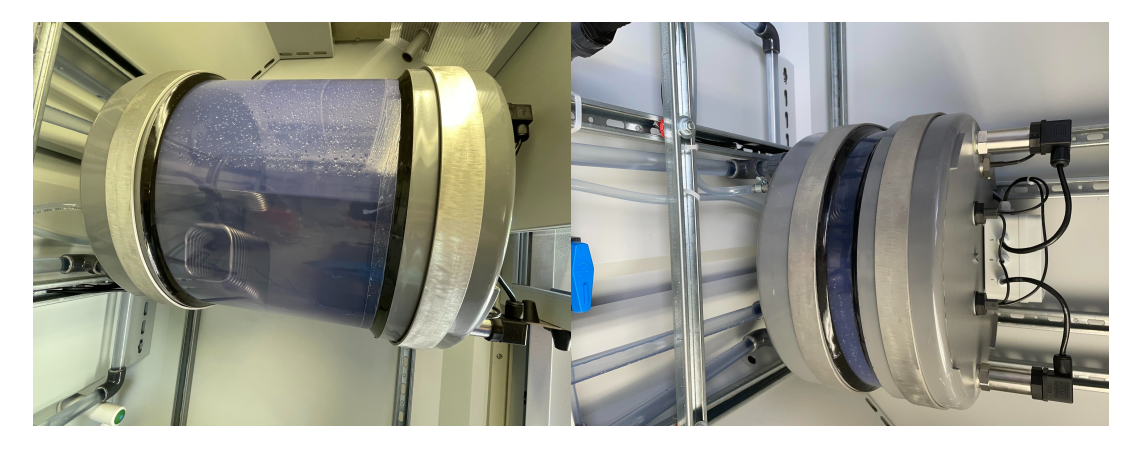


Figure 4.3: H_2 gas separator (left) and O_2 gas separator (right). The 32 L H_2 gas separator is used for the separation of electrolyte from hydrogen, has a 31 cm diameter, and 40 cm length. Accordingly, the 16 L O_2 separator separates the electrolyte from the oxygen, has the same diameter, and its length is 20 cm. Inside the tanks, there are spiral tubes allowing the flow of water in the event of cooling demand.

4.1.6 Stack-Cell

The stack under investigation is made of 21 bipolar cells connected in series with a total length of 23 cm and a cross section of 21 cm x 19 cm and each cell consists of stainless-steel electrodes. Between the electrodes and the membrane is the KOH (35 wt%) electrolyte which is decomposed in hydrogen and oxygen. On a stack level, there are two inlet and two outlet ports. Each inlet and outlet corresponds to the analyte and catholyte while the flow is distributed in parallel between the cells.



Figure 4.4: Single cell with stainless-steel electrode. The bolts are used to fasten the anodic and cathodic chambers. At the bottom plastic tubes, the electrolyte is inserted while at the upper tubes the electrolyte with the product gases leaves the cell. The cell has dimensions of 22 cm x 19 cm.

4.2 Polarization curves

An important aspect of electrolyser modeling is the polarization curve that expresses the energy consumption of the stack. As previously mentioned, the stack of the lab consists of 21 individual cells that are connected in series. To accurately measure the polarization curve of the stack and avoid the presence of shunt current, which is often observed in stacks with more than 21 cells [50], an identical single cell is built. The measurements were performed for 30 °C, 40 °C, and 50 °C after varying the current from 26.6 mA/cm² (2 A) to 160 mA/cm² (12 A). The results recorded by the instruments were used to calibrate the model in Python. The same procedure was followed for a Nickel electrode cell on grounds of comparison. The characteristics of both cells are shown in the table below (Tab. 4.1). Proper anode and cathode exchange current density had to be fitted such that the error between the voltage dictated by the experimental data and the one predicted by the literature to be plausible and reliable [63, 64, 65, 66]. The figures below illustrate the behavior of the single cell under different temperatures, pressures, and geometrical variations.

It can be observed from Fig. 4.5 that the curves reveal a good agreement between the experimental data (cell 1) and the physical model since the maximum error does not exceed 1.7%. The values of ω_s and τ_s found to represent the data satisfactorily are 0.4 and 1.8, respectively. As already mentioned in the previous chapters, high temperatures

Table 4.1: Geometrical aspects and materials of the cell components. The flow of the electrolyte is chosen to be high to avoid bubble congestion in the interelectrode gap while the material selection is based on the cost and their low electrical resistance according to the literature.

Alkaline cells			
Specification	Cell 1	Cell 2	
Electrode material	Stainless Steel	Nickel	
Height (cm)	5	5	
Area (cm ²)	75	75	
Spacing (cm)	0.2	0.16	
Membrane material	Material A	Material B	
Membrane thickness (cm)	0.1	0.06	
Electrolyte	KOH (35 wt%)	KOH (35 wt%)	
Electrolyte flow (lt/min)	1	1	

increase the electrolyte conductivity and enhance kinetics, thus leading to less voltage generated. At low current density, a non-linear behavior is observed due to activation losses in the electrodes while at high current density activation losses reach a constant value because of their logarithmic nature. At the same time, the linear ohmic losses on account of the components such as membrane and electrolyte, prevail. In general, the model can predict the voltage of the cell for a specific current and capture the behavior for different operating conditions.

Regarding cell 2, the comparison of the experimental data and the simulation are shown in Fig. 4.6. It is clear that the model describes adequately the data with less than 1.9% deviation. In this case, the values of ω_s and τ_s are 0.9 and 1.41, respectively. Once more, the low current region is distinguished by the non-linear behavior where the activation losses have the highest portion of the overvoltages. On the other hand, as the current increases, the activation losses reach a maximum value and the ohmic losses start to prevail rendering a linear profile to the polarization curve.

Concerning the sensitivity of cell 1 voltage to the pressure, the physical model (Fig. 4.7) indicates that as the pressure increases the voltage increases insignificantly. This can be explained by two counter-effects taking place inside the cell. On the one hand, an increase in the pressure rises the reversible voltage which is a major part of the total voltage. On the contrary, high pressures are beneficial for reducing the size of the bubbles on the electrode surface and in the bulk of the electrolyte, hence reducing the activation and ohmic losses.

It is well known that materials with high electrochemical activity are preferable on account of their low activation losses and enhanced overall efficiency. An important indicator of the material's activity is the exchange current density. Fig. 4.8 reveals the sensitivity of cell 1 to the electrode materials and underlines the fact that the cell's efficiency is tremendously influenced. It can be observed that an increase of the cathodic

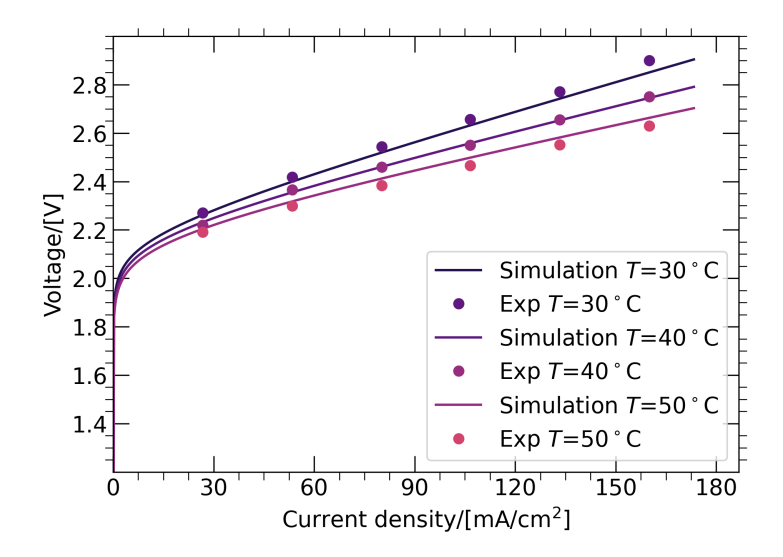


Figure 4.5: Comparison of polarization curves between experimental data (cell 1) and model for 1 bar and different temperatures. The experimental data are described reasonably well by the model for all the temperatures tested. The nonlinear behavior due to the activation losses in low current densities, and the linear one owing to the ohmic losses at high densities are observed in the polarization curves.

exchange current density by two and four orders of magnitude diminishes the voltage by approximately 10% and 20%, respectively. In general, high exchange current densities lead to a low cell voltage. The elevated temperature is an additional parameter that enhances kinetics and positively affects the exchange current density.

It has already been stressed that the electrode's material is important in the total energy consumption during hydrogen production. Nowadays, inexpensive materials with low activation losses are preferred to make the cost of green hydrogen production competitive with that of grey. Such material is Nickel and for that reason, a Nickel electrode cell is built with the aim of comparing it with Stainless-Steel. Although the cells have different structures, the model can predict their behavior under different specifications such as spacing and membrane material. Fig. 4.9 illustrates the polarization curves for Stainless-Steel and Nickel electrodes at 50°C, 1 bar, and different membrane material selections. In Fig. 4.9(b) and Fig. 4.9(c), the voltage of cell 2 is on average 17.7% less than that of cell 1. The explanation lies in the higher exchange current density of Nickel which reduces the activation losses, a large portion of the total voltage losses. In Fig. 4.9(a) and Fig. 4.9(d), it is apparent that membrane A for both Nickel and Stainless-Steel leads to a higher voltage compared to membrane B and this difference grows linearly. The largest difference is observed at 160 mA/cm² where membrane A induces on average 11.7% higher voltage for both electrodes. A reason for that is the larger thickness, the low wettability and higher tortuosity that hinder the movement of charged ions and cause a higher membrane resistance.

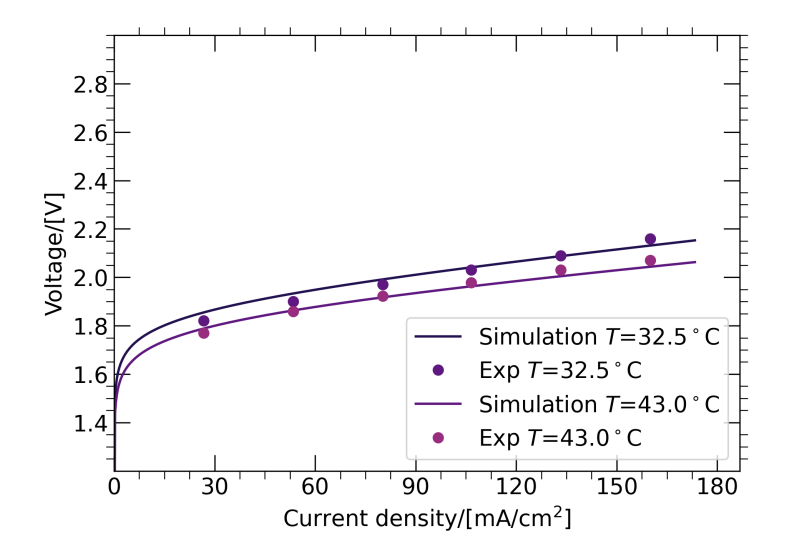


Figure 4.6: Comparison of polarization curves between experimental data (cell 2) and model for 1 bar and different temperatures. The experimental data are simulated by the model with less than 1.9% error for all the temperatures tested. The non-linear behavior due to the activation losses in low current densities, and the linear one owing to the ohmic losses at high densities are distinguished in the graph.

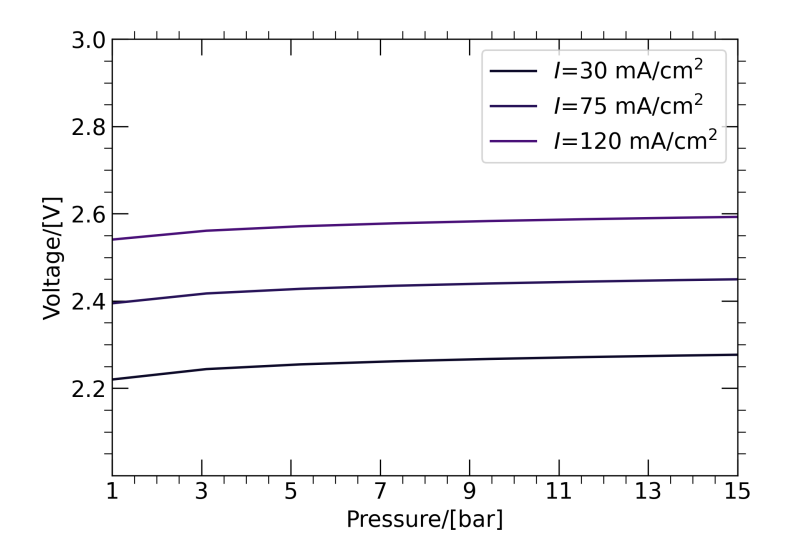


Figure 4.7: Cell 1 voltage as a function of pressure for various current densities at 50 °C. The reversible voltage increases with pressure while the opposite occurs for the losses due to the bubble presence in the electrolyte and electrode. Consequently, an insignificant increase in cell voltage due to pressure is observed.

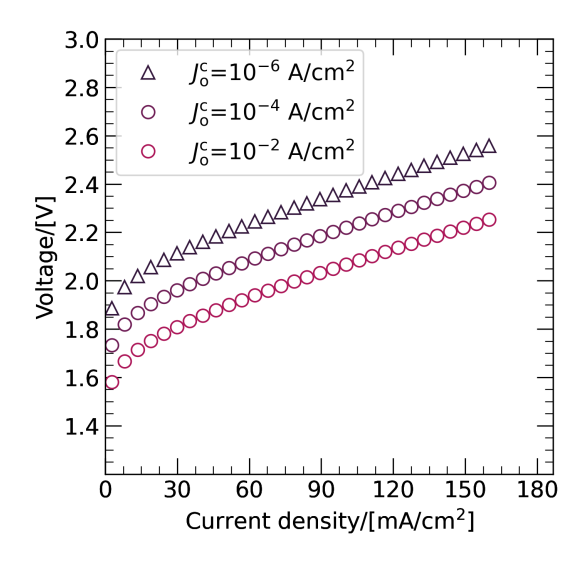


Figure 4.8: Effect of the cathodic exchange current density on polarization curve for cell 1 at 50 °C and atmospheric pressure. It is clear that the exchange current density heavily affects the cell voltage. Its enhancement by two or four orders of magnitude leads to 10% and 20% voltage reduction, accordingly. This discrepancy is observed irrespective of the current density applied.

Fig. 4.10 illustrates the contribution of each source of overpotential to the total voltage of cell 1 at 1 bar and 50 °C. The dominant losses are the activation that take up a significant part of the total energy input with a constant contribution at high current densities owing to the logarithmic nature. Increasing the exchange current density by selecting highly electroactive materials would considerably lower the activation losses. In addition, the ohmic losses grow linearly with current and play a significant role in the total cell voltage, especially at elevated current. Their contribution is maximum at 160 mA/cm² reaching 15% of the total voltage. Normally, small spacing, conductive membranes, and high electrolyte flow have proven to reduce ohmic losses.

The energy consumption and the efficiency of cell 1 are of paramount importance for the evaluation of the system. Fig. 4.11 displays that for 30 °C and 50 °C, where is it evident that efficiency decrease with current and increase with temperature while the opposite occurs for the power. In specific, high temperatures lead to the reduction of the activation and ohmic losses but at the same time reduce the thermoneutral voltage. The benefits of high temperatures in the cell efficiency grow with the current applied where at 27 mA/cm² and 160 mA/cm² the difference between 30 °C and 50 °C is 3% and 7.5%, respectively. On the other hand, the difference in the power is significant for high currents where at 160 mA/cm² this difference is around 14.5%. The explanation lies in the fact that at currents below 67 mA/cm² the cell voltage does not alter considerably with temperature (see Fig. 4.5).

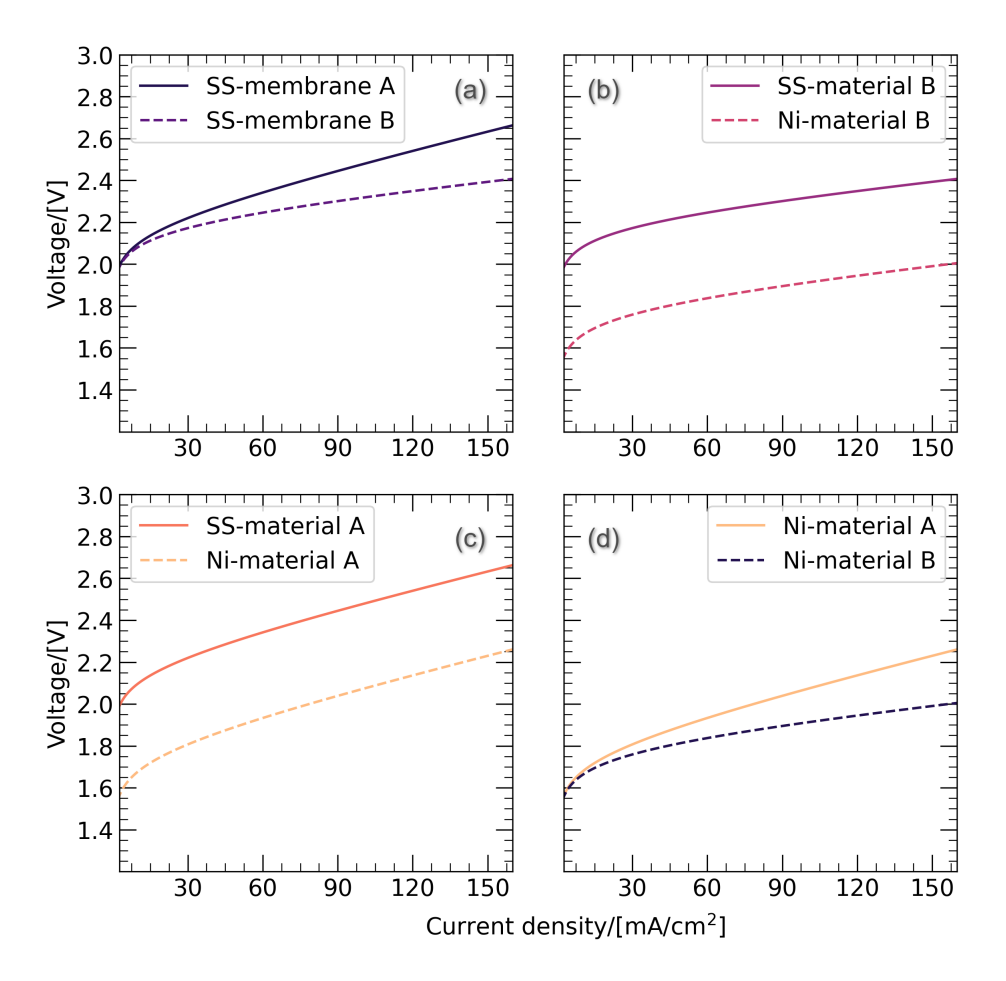


Figure 4.9: Polarization curves of Stainless Steel and Nickel electrode at 50 °C and 1 bar. Nickel electrode demonstrates superior performance by having 17.7% less voltage compared to SS owing to the higher electrochemical activity. This can be seen in (b) and (c). Simultaneously, in both electrodes, membrane B induces less voltage drop as opposed to membrane A as can be seen in (a) and (d). The voltage difference increases with the current density and reaches a maximum value of 11.7% at $160~\text{mA/cm}^2$. The explanation lies in the electrolyte repelling pores, the thick material, and the higher tortuosity of membrane A.

4.3 Thermal modeling

This section is dedicated to the demonstration of the thermal behavior of the stack under various circumstances including structural limitations like bypass current.

4.3.1 Theoretical stack performance

The reaction taking place in the stack is the driving force for the heat generation and the temperature increase of the system. Under normal circumstances, the single

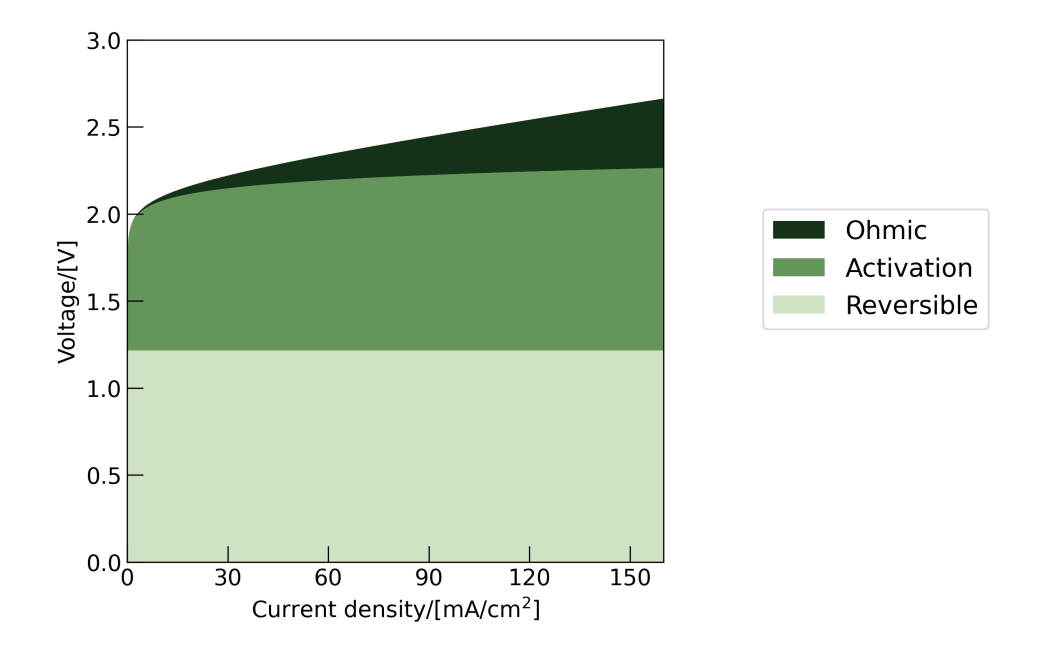


Figure 4.10: Contribution of each overpotential term to the total voltage for cell 1 at 50 °C and 1 bar. The proportion of the reversible voltage to the total reduces with current since its value is constant. Concerning the overvoltages, the activation losses have the highest contribution compared to the ohmic ones in the current density range displayed. Nonetheless, the ohmic losses grow linearly with current where at 10 mA/cm^2 is almost 0% while at 160 mA/cm^2 is 15%.

cell voltage is equal to the voltage of each cell in the stack for the same current density. Applying the operating conditions mentioned in Tab. 4.2 and performing a sensitivity analysis, insightful observations are made.

Fig. 4.12 shows the temperature of the stack and gas separators for 100 mA/cm² (Fig. 4.12(a)) and 200 mA/cm² (Fig. 4.12(b)). It is evident that the higher the current density, the more heat is generated, thus leading to higher temperatures. Specifically, the steady state temperature for 100 mA/cm² and 200 mA/cm² is 38 °C and 58 °C, respectively. The temperature difference between the stack and the gas separators increases from 0.5 °C at 100 mA/cm² to 1 °C at 200 mA/cm² on account of higher heat losses to the environment since both the temperature difference and the heat transfer coefficient is higher. It is noteworthy that at 200 mA/cm² the stack reaches a steady state condition faster compared to 100 mA/cm². The explanation lies in the fact that as the stack temperature grows, the cell voltage reduces while the thermoneutral voltage increases, hence heat production reduces (Eq. 3.41). At elevated temperatures, ambient heat losses are higher, therefore a decreasing heat generation and an increasing heat abduction lead to a rapid steady-state condition.

Another aspect of the system's analysis is the mass flow of the electrolyte. Fig. 4.13 displays the thermal behavior of the system for 0.01 kg/s (or 0.5 Lt/min, Fig. 4.13(a))

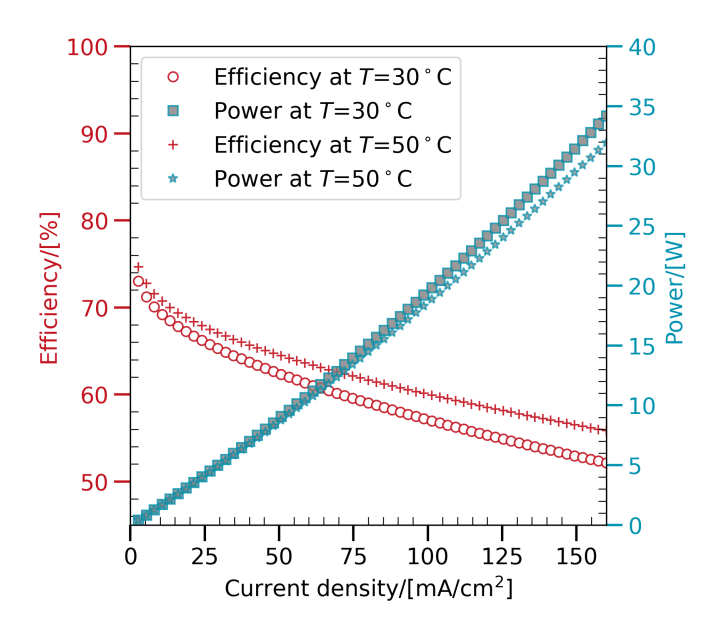


Figure 4.11: Efficiency and power of cell 1 at 30 °C and 50 °C under atmospheric pressure. The efficiency of the cell at 50 °C is considerably higher by 7.5% compared to 30 °C at 160 mA/cm 2 due to lower ohmic losses. Regarding the power, a difference of almost 15% is observed. In both cases, the temperature has no significant effect at very low current densities since ohmic losses are negligible and mainly the activation overpotential prevails.

and 0.5 kg/s (or 25 Lt/min, Fig. 4.13(b)) at 200 mA/cm². When the mass flow is high, heat generation in the stack is immediately circulated in the hydrogen and oxygen tanks retaining a uniform temperature distribution along the system (< 0.5 °C difference). On the other hand, low electrolyte mass flow hinders the cooling of the electrolyte causing a higher stack temperature compared to that of the separator tanks. In the case shown, this difference is more than 8 °C. Regarding the energy consumption of the low electrolyte flow, the stack reaches faster the steady state at a higher temperature which leads to lower voltage. In addition, lower pumping costs increase the efficiency of the system. It can be anticipated that the velocity of the electrolyte due to pumping is significantly low and the higher bubble velocity due to buoyancy will drag the electrolyte upwards increasing its velocity. Therefore, a drift flux model would reproduce more accurate results concerning the real electrolyte mass flow.

Throughout the formulation of the ambient losses of the system in chapter 3, both natural and mixed convection approach were considered. Although natural convection is mainly driven by the temperature difference, forced convection is strongly dependent on the air velocity of the surrounding air. A quiescent air leads to low heat losses that depend mainly on natural convection and result in high system temperature. This response is displayed in Fig. 4.14, where for 0.1 m/s (Fig. 4.14(a)) and 200 mA/cm² the steady-state temperature is 54 °C and is approximately 4 °C degrees lower compared to the

Table 4.2: Simulation input parameters for the theoretical modeling of the stack behavior. The parameters were chosen according to custom experimental conditions performed in the lab.

Parameter	Value	Unit
Electrolyte mass flow	0.108	kg/s
Ambient temperature	20	$^{\circ}\mathrm{C}$
Initial system temperature	20	$^{\circ}\mathrm{C}$
Ambient air speed	≈ 0	m/s
Electrolyte volume in H ₂ tank	13	Liters
Electrolyte volume in O ₂ tank	7	Liters
Operating pressure	1	bar

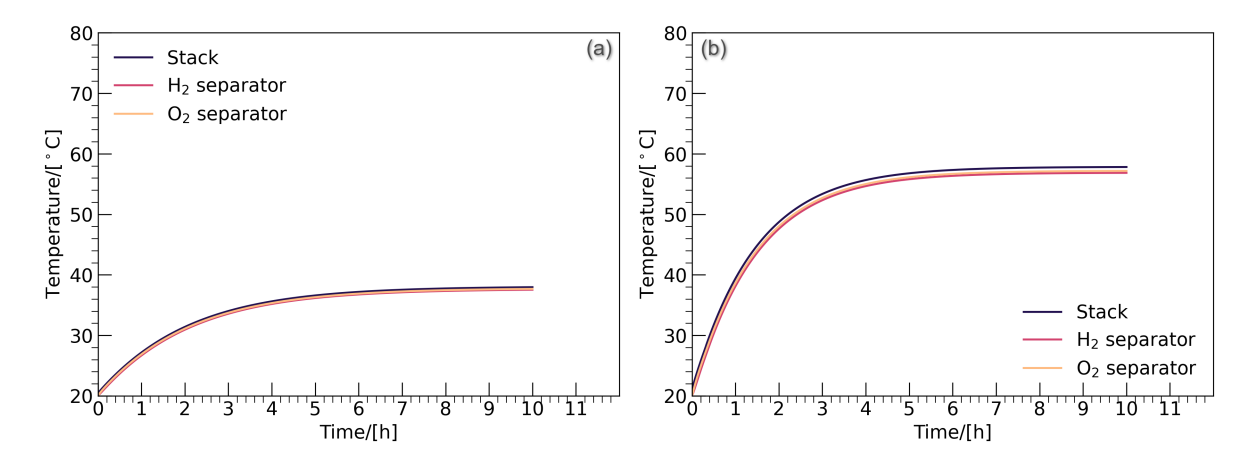


Figure 4.12: System temperature with time for constant current of $100~\text{mA/cm}^2$ (a) and $200~\text{mA/cm}^2$ (b). At $200~\text{mA/cm}^2$ the heat generation is larger thus leading to 20~°C higher steady state temperature. In both cases, the system has a nearly uniform temperature owing to the high electrolyte flow. It must be noted that in the high current density case the system reaches faster steady conditions due to the increasing thermoneutral voltage with the temperature that leads to faster equalization of the ambient heat losses to the heat generation.

case of natural convection (Fig. 4.12(b)). On the other hand, for 1 m/s (Fig. 4.14(b)), forced convection prevails leading to significantly high ambient losses that reduce the temperature to 43.5 °C. The temperature difference between the two extreme cases is more than 10 °C, affecting remarkably the energy consumption of the system. Despite the smaller voltage generated at low heat losses, the cooling circuit has to be activated more frequently, thus increasing expenses. On the contrary, if the cooling system is integrated into a heat pump configuration, then minimal ambient heat loss is preferred.

Fig. 4.15 explores the influence of the stack's temperature by the total electrolyte volume in the separator tanks. Large electrolyte volume increases the time for the

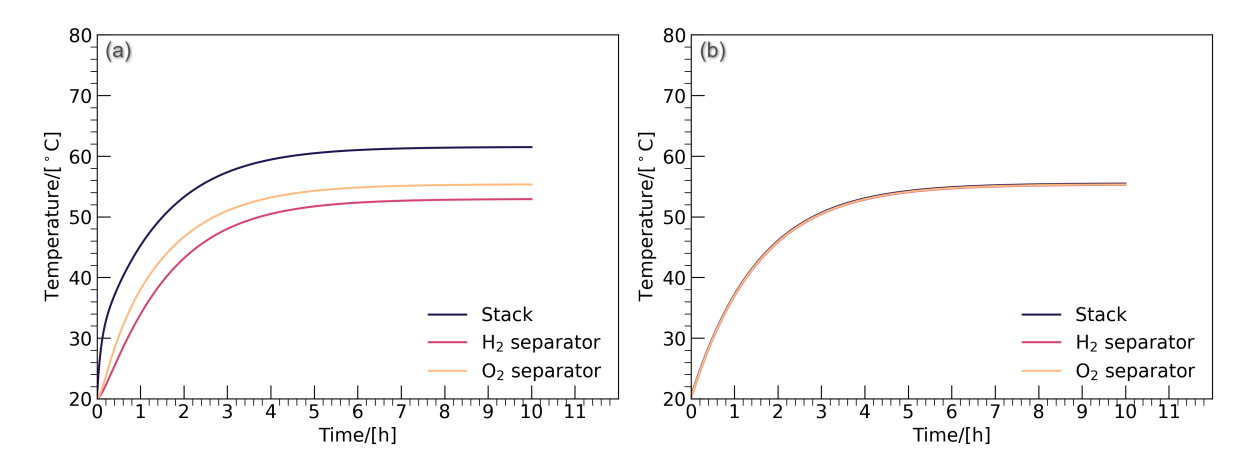


Figure 4.13: System temperature variation versus time for electrolyte flow of 0.5 Lt/min (a) and 25 Lt/min (b) at 200 mA/cm². At high electrolyte circulation, the cooling of the stack is achieved and the temperature is observed to be uniform across the components of the system. On the contrary, at a low mass flow, the stack temperature is almost 10° C higher than that of the separators.

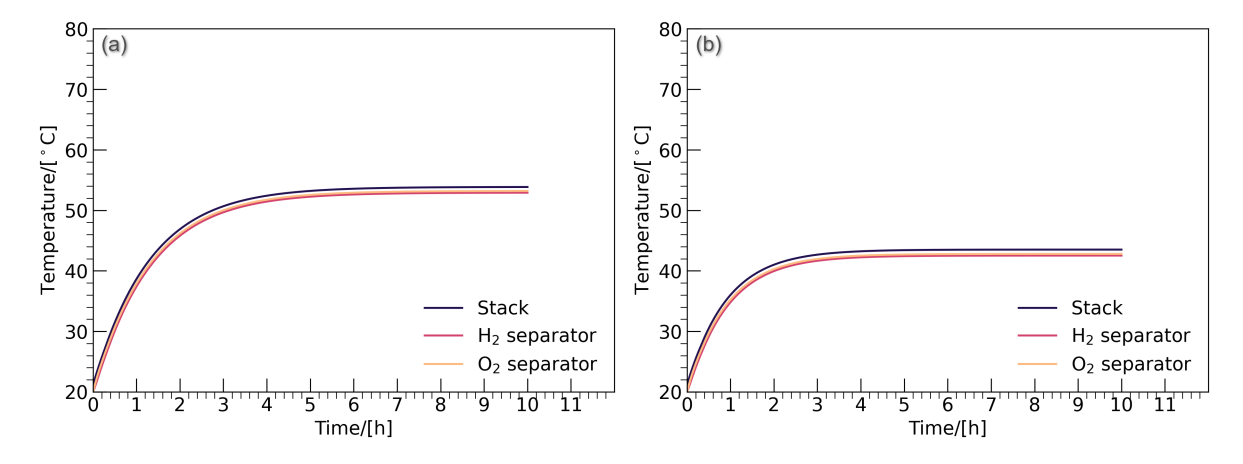


Figure 4.14: System temperature variation versus time for ambient air velocity of 0.1 m/s (a) and 1 m/s (b) at 200 mA/cm². For a nearly quiescent ambient air, heat losses are driven mainly due to natural convection leading to high stack temperature. On the other hand, at 1m/s air speed, the steady state temperature is 43.5 °C which is more than 10 °C than the 0.1 m/s air velocity case.

system to reach steady state conditions while doubling the volume increases the thermal response by approximately one hour. On the other hand, no significant effect on the final temperature of the stack is observed. It is interesting to note that since the size of the separators remains the same, the value of the heat losses is almost the same for each case. Nonetheless, the smaller the electrolyte's volume, the higher the proportion of the heat losses, and hence irreversibility, to the total energy of the system. Furthermore, the

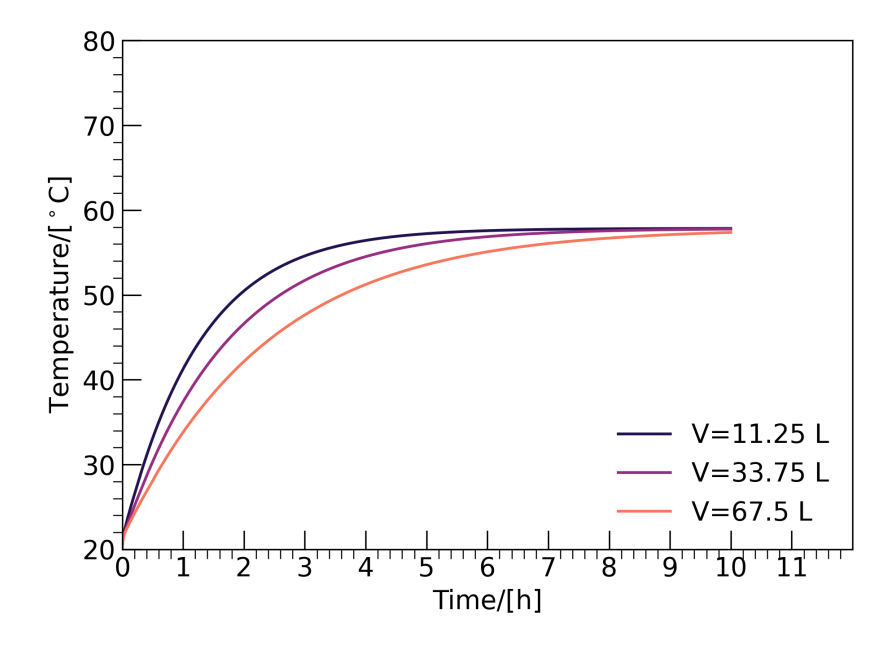


Figure 4.15: System temperature variation versus time for different electrolyte volumes in the system and 200 mA/cm². It is noticeable that the volume of the electrolyte in the separator tanks does not influence the steady-state temperature of the system. An expected outcome is the longer time that takes for the system to reach this condition as the tank volume increases.

system's thermal behavior is prone to ambient conditions that render it unsafe under unsteady operating conditions.

All alkaline electrolyser systems operate until a maximum temperature for protection against membrane failure. In the examined system, the highest operating point is 60 °C, and for that reason, a cooling system (coils) is installed in both gas separator tanks. Fig. 4.16 displays the response of the system under continuous (a) and interval (b) cooling mode at 220 mA/cm². For continuous, when the maximum allowed temperature is reached, 200 W of cooling is applied to keep the system at the constant temperature of 50 °C. After 4 hours the system reaches a steady state which means that the heat generated by the stack equals the heat losses to the environment plus the cooling load. The power of the stack is approximately 1030 W, therefore, almost 20% of this power can be extracted in the form of heat. In large-scale electrolysis systems that operate under constant temperature and higher currents, the cooling load is significantly high that can be used in heat pumps or district heating. For the interval mode, Fig. 4.16 (b), 500 W cooling is applied until the system's temperature reaches 50 °C which is accomplished after 45 minutes. Although the cooling coils are in the gas separators, the high electrolyte flow enables the stack to cool quickly and eliminate temperature differences among the components of the system.

The second law analysis is a necessary tool to evaluate the irreversibility of the system

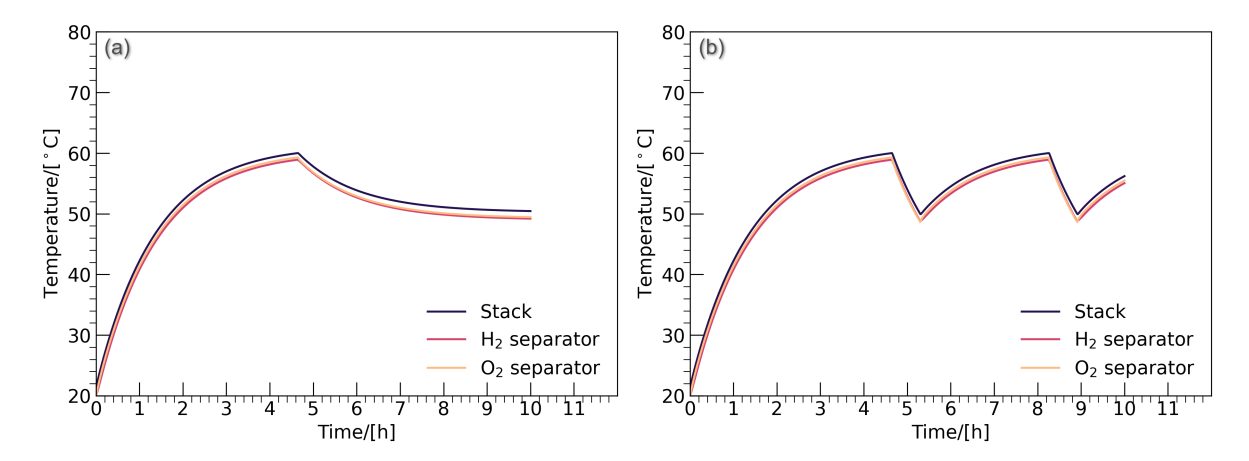


Figure 4.16: System temperature variation at 200 mA/cm² under 200 W of continuous (a) and 500 W of interval cooling. A continuous low cooling load causes a constant temperature of 50 °C in the stack that takes almost 4 hours to reach equilibrium. Regarding the interval cooling, the system needs a shorter time (45 mins) to achieve the lower temperature bound. After its deactivation, the stack temperature starts to increase again.

under given conditions and provide guidelines for an efficient operation. Fig. 4.17 presents the entropy generated in the stack with the applied current. The relatively linear trend suggests that the high current densities come with the price of large losses mainly due to ohmic resistances. Doubling the current from 80 mA/cm² to 160 mA/cm² gives rise to entropy generation from 0.45 W/K to 1 W/K, slightly higher than twofold. The increase in current density leads to a higher steady-state temperature which increases the difference between the reversible and the thermoneutral voltage resulting in an almost constant slope. Another key factor is the ambient heat losses that grow with the current owing to the larger temperature differences between the stack and the environment. On the other hand, the convective term does not significantly affect the entropy generation since the temperature of the stack and the gas separators is the same. A clear message from the figure would be the operation at a low current density for minimum losses. Nonetheless, the faradaic efficiency of the electrolyser must be considered in case shunt currents are present, especially in the low current region. Consequently, based on the faradaic efficiencies of commercial electrolysers, a range of $100 - 130 \text{ mA/cm}^2$ would be a rational choice.

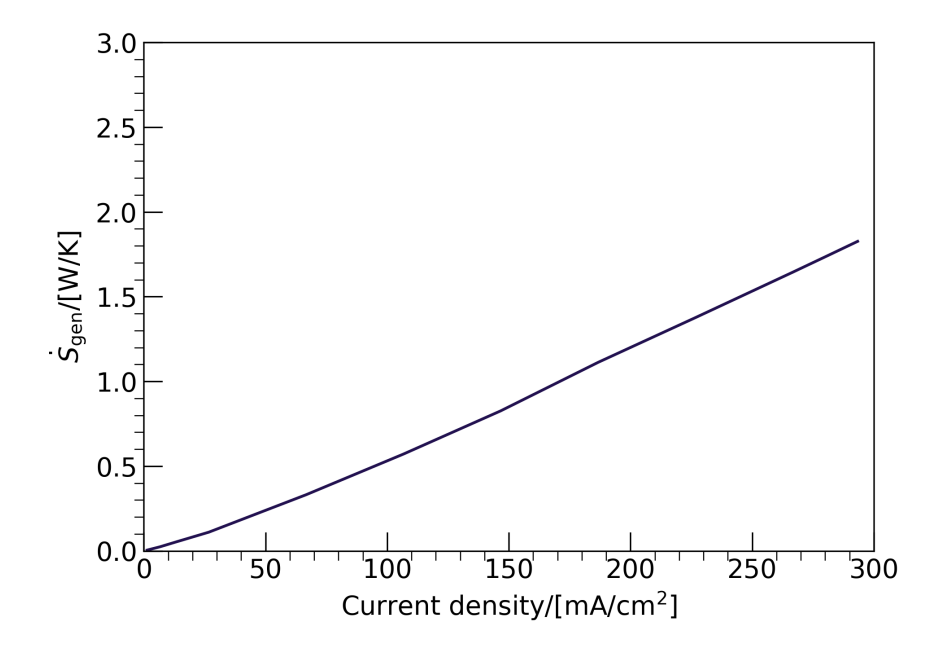


Figure 4.17: Steady state entropy generation in the stack as a function of current density. The generated entropy increases linearly to the current density since its value doubles when the system shifts from $80~\text{mA/cm}^2$ to $160~\text{mA/cm}^2$. The combination of increasing heat losses and the difference between the thermoneutral with the reversible voltage is responsible for that trend.

4.3.2 Real stack performance

In bipolar stacks, the presence of bypass current is significant, and it leads to less voltage and less hydrogen production. The origin of bypass current is the low electrical resistance of the electrolyte in the channels and manifolds giving the current viable paths to escape from the main zone of reaction. Therefore, part of the current is not utilized for the dissociation of water resulting in lower efficiency and lower voltage. The shunt current (or bypass current) in bipolar electrolysers is well documented in the literature where the main focus has been the prediction and minimization of it [50, 71, 72]. The operation of the stack is considerably different than that of the single cell due to the different flow rates and patterns of electrolyte inside the stack. The handmade nature of the products introduces inevitable differences in the design that may notably affect the batch-to-batch behavior. Therefore, the theoretical model can no longer be regarded as an accurate approach, and individual experiments for the stack performance have to be executed.

A successful thermal model necessitates the prediction of the stack's voltage at every temperature and current for the calculation of the generated heat. A series of experiments (Tab. 4.3) were performed for investigating the thermal behavior of the system. The current, voltage, and temperature measurements throughout the procedure enabled the determination of an empirical correlation of the voltage as a function of current and

temperature (Eq. 4.1).

$$U_{\text{stack}} = 40.59 + 13.31 \cdot \log(I) - 0.084 \cdot t \tag{4.1}$$

Where I is the current in A, and t is the temperature in $^{\circ}$ C

The mathematical expression that satisfies the experimental results has a 1.5% average and 6% maximum error which is mainly encountered at low current density. It should be mentioned that for low current density levels (< 100 mA/cm²) the voltage increased irrespective of the temperature. Although this behavior is not found in the literature before, it is suspected that the presence of the shunt currents affects the response of the circuit's resistance. Additionally, the double capacitance layer due to the immediate transition from one current to the other and the harmonics from the PSU alter the voltage of the stack [73]. On the other hand, for high current densities, the voltage reduced with temperature as expected. Consequently, deriving an accurate expression for the voltage is not an easy task because part load and full load operation do not have the same trend with temperature.

Incorporating the empirical equation above in the thermal model, the temperature of the stack can be predicted for various working conditions.

Table 4.3: Experimental conditions during the testing of the stack. The electrolyte flow avoids the overheating of the stack while the ambient temperature is controlled with the help of the A/C unit located in the lab. The PSU ensures the monitoring of the current to the desired values.

Parameter	Test 1	Test 2	Test 3
Electrolyte flow	0.108	0.0954	0.0954
(kg/s)			
Lab temperature	20	20	18
(°C)			
Current (A)	14 A, 0 <t<13 min<="" td=""><td>4 A, 0<t<69 min<="" td=""><td>2 A, 0<t<60 min<="" td=""></t<60></td></t<69></td></t<13>	4 A, 0 <t<69 min<="" td=""><td>2 A, 0<t<60 min<="" td=""></t<60></td></t<69>	2 A, 0 <t<60 min<="" td=""></t<60>
	13 A, 113 <t<397< td=""><td>6A, 69<t<157 min<="" td=""><td>4A, 60<t<120 min<="" td=""></t<120></td></t<157></td></t<397<>	6A, 69 <t<157 min<="" td=""><td>4A, 60<t<120 min<="" td=""></t<120></td></t<157>	4A, 60 <t<120 min<="" td=""></t<120>
	min		
		8 A, 157 < t < 201 min	
		10 A, 201 < t < 244	
		min	
		12 A, 244 <t<319< td=""><td></td></t<319<>	
		$\mid \min$	
Electrolyte in H ₂	13	13	13
tank (lt)			
Electrolyte in O_2	7	7	7
tank (lt)			
Operating pres-	1	1	1
sure (bar)	3.7	3.7	
Insulation	No	No	Glass wool roll and
			polyethylene (PE) in-
			sulation pipes

Fig. 4.18 displays the temperature of the stack (a) and H_2 separator (b) recorded by the thermocouples. The current is regulated at 14 A for the first 13 mins and later on

lowered to 13 A due to the incapability of the PSU to cope with this power. The total duration of the experiment was 6 hours, and the lab temperature was 20 °C, maintained constant throughout the process (Tab. 4.3, Test 1). It is noticeable that the temperature keeps increasing owing to the heat generated from the ohmic losses. After 6 hours, it reaches a steady state at 46 °C for the stack and 45 °C for the separator, signifying the equilibrium between heat production and ambient losses. The uniform energy distribution of the system is visible from the minute temperature difference between the stack and the separator, manifesting the aftermath of a high electrolyte mass flow. On the same graph, the temperature profiles computed by the model are presented. It is apparent that the thermal behavior of the system is well predicted, and the deviation does not exceed 1.44 °C (3.1%). The main contributions to that are the sound assumptions regarding the heat losses and the heat production inside the stack.

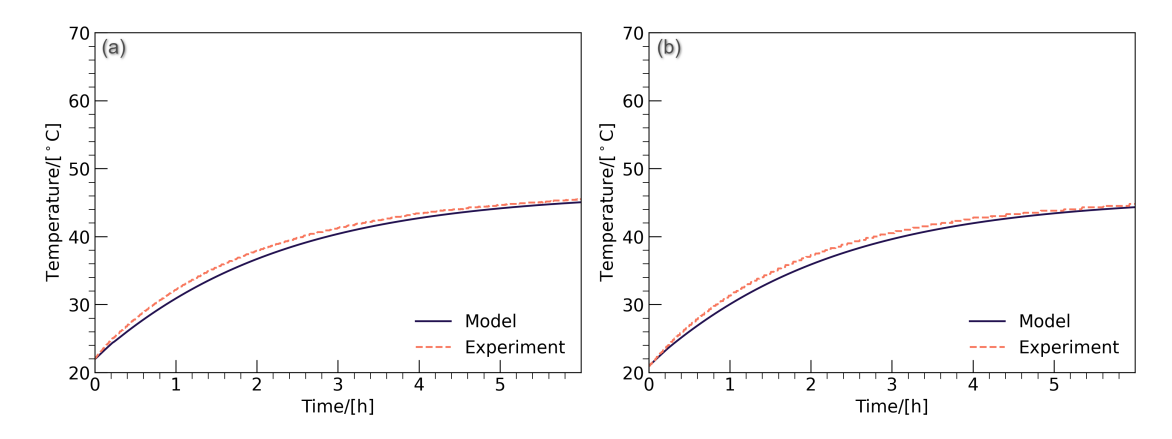


Figure 4.18: Experimental (dotted lines) and simulated (solid lines) heating curves of the stack (a) and the H₂ separator tank (b). The thermal response of the stack and the separator, shown by the experiment, is almost the same and it is computed accurately by the model. The maximum deviation between the measurements of test 1 and the simulation does not exceed 1.5 °C.

Fig. 4.19 shows the temperature profile versus time regarding the stack (a) and the H₂ separator (b). This time, the current starts from 4 A and is increased by 2 A roughly every hour (Tab. 4.3, Test 2). The transition to a higher current is visible each time from the small 'alcove' on the line. The purpose was to observe the system's thermal response at lower currents and compare it to the model. Owing to the constantly changing current, the system terminates at 41.5 °C without reaching steady-state conditions. As far as the model is concerned, it is evident that there is a discrepancy with the experimental data that grows with time and after a certain period, it reaches a maximum deviation of 4.5 °C (10.8%). First thoughts would indicate an overestimation of the heat transfer coefficient or the thermal capacity of the system. Nevertheless, such an argument would contradict the validity of the first experiment since heat transfer depends solely on temperature and air velocity, and is independent of the applied current. By taking a closer look at the stack temperature, the difference in the gradient between the experimental and simulated line

is large in the beginning. In particular, as the current increases, the deviation in gradient becomes smaller, so towards the end of the experiment (I > 10 A), they become parallel. This indicates a significant discrepancy mainly in heat generation and not in heat loss since stack and ambient temperature have less than a 5 °C difference. Consequently, at low currents heat generation is underpredicted and at high ones is described reasonably well.

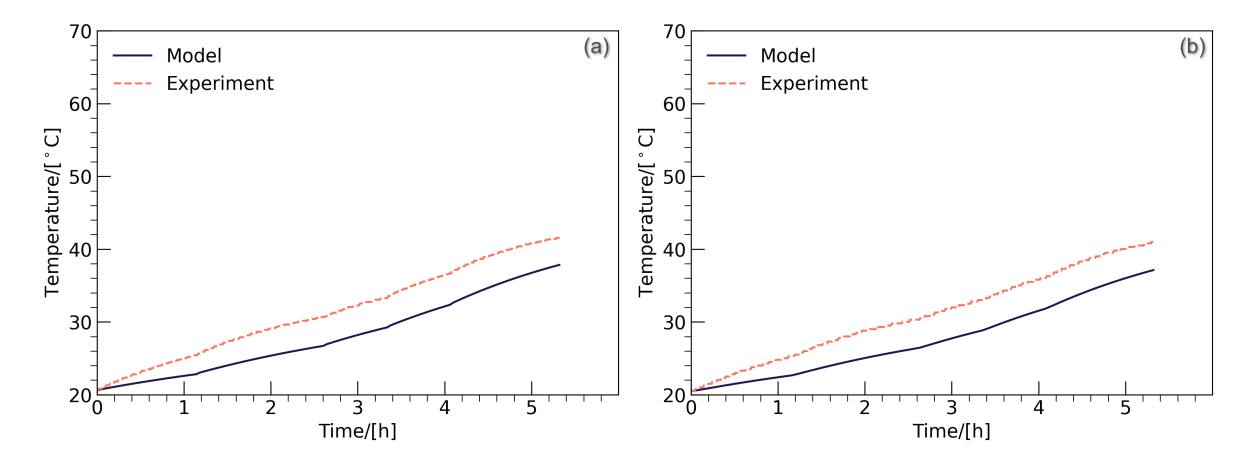


Figure 4.19: Experimental (dotted lines) and simulated (solid lines) heating curves of the stack (a) and the H₂ separator tank (b). The current starts from 4 A and is increased by 2 A every hours. In both figures, the model underpredicts the temperature of the system. This discrepancy grows with time and after a certain point, it reaches a maximum value of 10.8%. The difference between the temperature gradient observed in the experiment (test 2) and the model is high in currents lower than 8 A whereas for higher currents they seem to be parallel.

The explanation lies in the presence of bypass current which is notable at lower than 10 A, leading to a heat generation that is higher than the calculated one (Eq. 3.41). On the other hand, for currents higher than 10 A, bypass current has diminished to such an extent that heat generation is well predicted by the simulation. The following step is to calculate the proportion of bypass current to the total one by taking advantage of the stack's thermal behavior. A first approach would assume that all the cells of the stack have the same voltage and the shunt current path, owing to electrolyte channels and manifold, is treated as one resistance. In each cell, the current flowing is less than that provided by the PSU since part of it escapes the reaction zone. The above mentioned explanation can be formulated as:

$$\dot{Q}_{\rm gen} = \dot{Q}_{\rm reaction-zone} + \dot{Q}_{\rm shunt} \Leftrightarrow \dot{Q}_{\rm gen} = (I_{\rm PSU} - I_{\rm shunt}) \cdot (U_{\rm stack} - N_{\rm cell} \cdot U_{\rm t,P}^{\rm tn}) + I_{\rm shunt} \cdot U_{\rm stack} \quad (4.2)$$

The energy balance formulated in the previous chapter concerned a single cell and was extended for a stack. Nonetheless, a single cell does not suffer from leakage current

and the term I_{shunt} was not taken into account. The purpose is to adjust the model and diminish the deviation observed in Fig. 4.19 while at the same time getting an approximate value of the shunt current in the stack. A simple way to make this link would be the introduction of a correction factor to the heat generation term in Eq. 3.41 In mathematical terms, this yields

$$\alpha_{\text{corr}} \cdot I_{PSU} \cdot (U_{\text{stack}} - N_{\text{cell}} \cdot U_{\text{t,P}}^{\text{tn}}) = (I_{PSU} - I_{\text{shunt}}) \cdot (U_{\text{stack}} - N_{\text{cell}} \cdot U_{\text{t,P}}^{\text{tn}}) + I_{\text{shunt}} \cdot U_{\text{stack}}, \text{ for } \alpha_{\text{corr}} > 1 \quad (4.3)$$

After rearrangements, the equation get the following form.

$$\eta_{\rm F} = 1 - \frac{I_{\rm shunt}}{I_{\rm PSU}} = 1 - \frac{(\alpha_{\rm corr} - 1) \cdot (U_{\rm stack} - N_{\rm cell} \cdot U_{\rm t,P}^{\rm tn})}{N_{\rm cell} \cdot U_{\rm t,P}^{\rm tn}}$$
(4.4)

It can be seen that the faradaic efficiency of the stack can be evaluated according to its thermal response by finding the correction factor for each current. As discussed earlier, a possible miscalculation of the heat transfer coefficient during the first hour of the experiment can be neglected because the difference in ambient and stack temperature is small. Nonetheless, an additional experiment is performed where the stack and separators are insulated with glass wool and the electrolyte pipes with PE (Tab. 4.3, Test 3). Initially, the stack operates at 2 A for the first hour, and then a higher current of 4 A for the second hour is applied. Fig. 4.20 demonstrates the temperature of the stack with time for the two-hour experiment recorded by the sensors while at the same time the model prediction is included. In both curves, the transition from 2 A to 4 A is observed in the increase of temperature slope since a larger current induces larger heat generation. It is apparent once more that the simulation underpredicts the temperature of the stack, thus validating the existence of a shunt current.

An empirical equation for the faradaic efficiency can be derived by finding the correction factors of Fig. 4.20 for 2 A and 4 A. The shape of this curve (Fig. 3.2) necessitates one more current at the maximum value (100% faradaic efficiency) for its determination. For that reason, a plausible assumption would be a 100% efficiency at 14 A, bearing in mind the examination of Fig. 4.18.

In fully functional hydrogen production setups, gas flow meters are installed downstream of the cathode and anode of the stack. This allows the direct measurement of the products' mass flow at any moment while at the same time dividing it by the theoretical amount yields the faradaic efficiency. Nonetheless, the presence of vapour or diffused gas in the stream alters the accuracy of the gauge, hence an accurate measuring spot is downstream of the purification system. In the current experimental setup, the gas flow meters were not yet installed leading to the quest for a quicker and cheaper method of quantifying the faradaic efficiency. Taking advantage of the system's thermal response, a reasonable evaluation of it can be deduced.

The estimation of the correction factors through the 2 A, 4 A, and 14 A enables the implementation of a fifth-order polynomial fitting curve for the prediction of all the

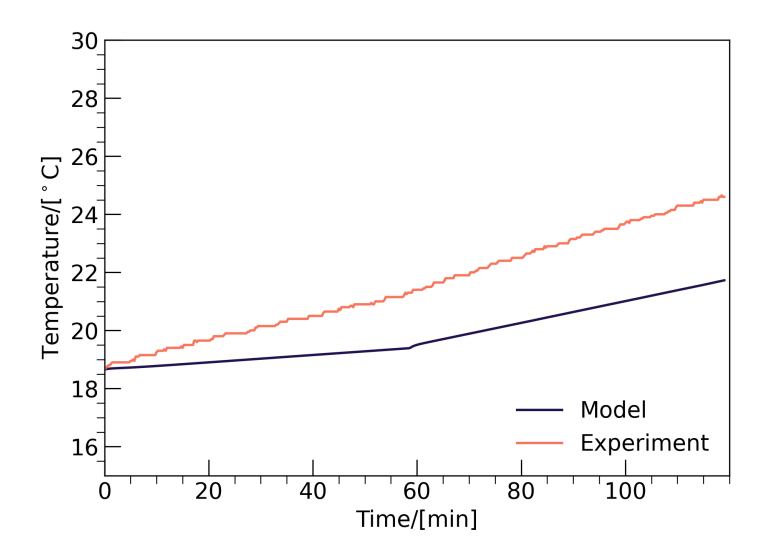


Figure 4.20: Experimental (dotted lines) and simulated (solid lines) heating curves of the stack for the insulated system (test 3). For the first hour, 2 A current is applied to the stack and later it on switched to 4 A. This transition can be also distinguished from the change in the temperature slope of the simulation curve after 60 minutes emphasizing the higher heat generation at larger currents. Comparing the experimental and simulated curves, a considerable deviation is detected between the temperature measurements and the model where the discrepancy in the gradient is still observed. An immediate consequence is that the model underpredicts the heat generation in the stack.

intermediate values. It should be noted that the faradaic efficiency is also a function of temperature ([74]), hence for each current, an average value of the correction factor is chosen. The equation derived is presented below.

$$\eta_{\rm F} = 2.56 \cdot 10^{-7} \cdot I^5 + 2.5 \cdot 10^{-6} \cdot I^4 - 18.5 \cdot 10^{-5} \cdot I^3 - 3.69 \cdot 10^{-3} \cdot I^2 + 0.13 \cdot I + 0.082$$
 (4.5)

Fig. 4.21 shows the experimental and simulated thermal response of the stack during Test 2 (Tab. 4.3) after the implementation of the faradaic efficiency in the computations. The temperature is well described by the model for every current emphasizing the fact that, indeed, the heat production via bypass current is significant and cannot be neglected. The maximum deviation does not exceed 2 °C (5%). The two lines are almost parallel revealing that if the experiment was executed for a longer period, the deviation would not propagate, and the error would remain the same.

Knowing the faradaic efficiency provides the opportunity to get an insight into the total efficiency which is of paramount importance for the evaluation of the system. Fig. 4.22 displays the faradaic, the voltaic, and the total efficiency with current density at 30 °C. As expected, the faradaic efficiency is low in the low current density range and reaches 100% at values higher than $180~\text{mA/cm}^2$. It should be noted that even at $173.3~\text{mA/cm}^2$

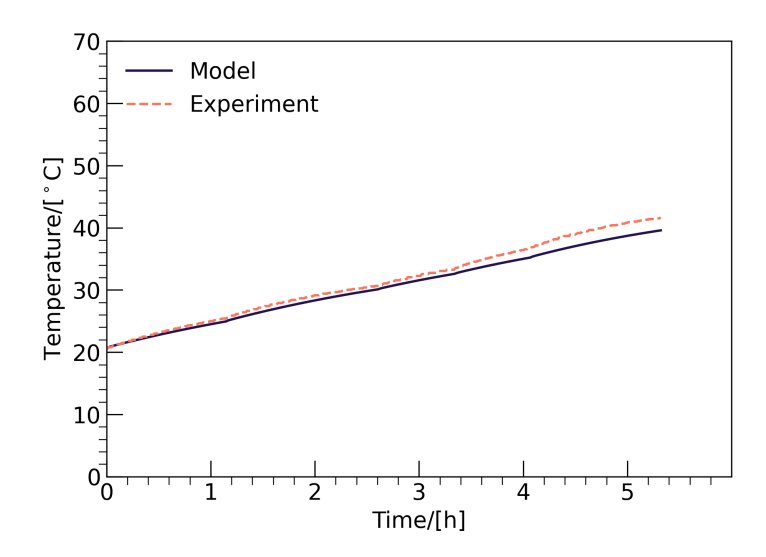


Figure 4.21: Experimental (dotted lines) and simulated (solid lines) heating curves of the stack after correction (test 2). It is clearly shown that the implementation of the correction factor reduces the deviation to a maximum value of 5% and manifests the important role of the shunt current in the thermal response of the stack. This time, the lines are practically parallel denoting the reliability of the model if a longer experiment was executed.

(or 13A) the faradaic efficiency is higher than 99% pointing out that Fig. 4.18 does not require any correction at all. Regarding the voltaic efficiency, it starts from 86% and drops to less than 60% at 340 mA/cm² due to the activation and ohmic losses. The really high value in beginning is justified by the fact that the shunt current induces less voltage in the stack and thus increasing the ratio of the thermoneutral to the stack voltage. On the other hand, the total efficiency reaches a maximum point of 60% around 12.7 A (or 170 mA/cm²) and starts to decline after that on account of the ohmic losses. It should be emphasized that the optimum efficiency is achieved when the product of faradaic and voltaic has the maximum value, since the former increases and the latter decreases with current density. Although a low current density is recommended for minimum overvoltage losses, the shunt current is so notable that undermines the high voltaic efficiency. Therefore, an operating span for optimum production would be from 120 mA/cm² to 180 mA/cm².

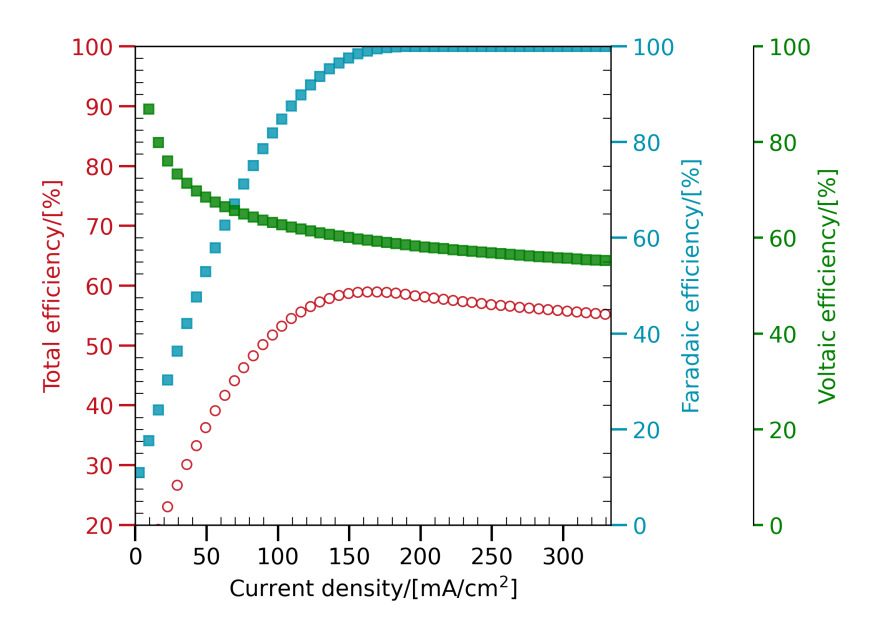


Figure 4.22: Faradaic, voltaic, and total efficiency of the stack with current density at 30 °C. The faradaic efficiency is relatively low for current densities smaller than $100~\text{mA/cm}^2$ and thus the total stack efficiency suffers. On the other hand, the voltaic efficiency starts from really high values and drops with current owing to overvoltage losses. The total efficiency increases with current and reaches a peak at $170~\text{mA/cm}^2$ which corresponds to a faradaic efficiency of nearly 100%. For higher currents, it reduces because the shunt current is zero while the ohmic losses grow linearly with the current.

5 | Discussion

In this chapter, all the salient results of the experiments and modeling are summarized, and the main conclusions are drawn. The experience accumulated through the practical and theoretical study of the alkaline electrolyser allows the inclusion of the necessary recommendations for enhancing the accuracy of the model and improving the efficiency of the stack.

5.1 Conclusions

The experiments and simulations performed on a cell and stack level provide the answers to the research objectives that were posed in the first chapter of this report and give insights into hydrogen production.

5.1.1 Cell level

The comprehension of the necessary knowledge and the formulation of the equations enabled not only the validation of the single cell's experimental data but also the modeling of its behavior under various conditions. The main deductions are explained below.

An analytical model formed on the basic principles of electrochemistry and fluids can accurately predict the polarization curve of a cell for every temperature. This is confirmed by the maximum error of 1.7% and 1.9% between the experimental data of SS and Nickel electrode compared to the simulation. The temperature has a positive effect on the voltage since it reduces considerably the voltage losses, especially in the high current region where ohmic losses prevail. This is also observed in the total power of the cell which is reduced by nearly 15% when the temperature raises from 30 °C to 50 °C. Regarding pressure, the cell voltage slightly increases owing to the rise in the reversible potential.

An important aspect is the selection of materials. It has been seen that membrane B is superior to membrane A by 11.7% at a current density of 160 mA/cm². The high surface tension of the membrane A blocks the electrolyte ions and leads to higher ohmic losses. On top of that, electrode material is of paramount importance for the overall efficiency of the cell since the overpotential losses account for the biggest portion of the total losses. This is also shown in the simulation where a 10% decrease in the voltage is

observed when the exchange current density is enhanced by two orders of magnitude. A real example is the lower voltage of the Ni electrode cell by 17.7% compared to that of SS.

5.1.2 Stack level

The thermal modeling of the stack is developed in terms of the lumped capacitance method. Useful details are provided on the theoretical stack behavior, including the gas separators.

The heat generation is proportional to the current of the stack and is shown that high currents lead to higher equilibrium temperature. This has an important effect on the stack voltage that reduces with temperature. On the other hand, the generated entropy increases due to the higher heat losses, as indicated by the relevant figure. Regarding the energy distribution in the system, a high electrolyte mass flow ensures a uniform temperature while a low one can create differences up to 10 °C between the stack and the separators. Additionally, the size of the separator tanks mainly affects the time it takes for the system to equilibrium. In specific, the larger the volume, the longer it takes.

Cooling is an indispensable feature in hydrogen production for the protection of the membrane and the avoidance of water evaporation. The theoretical model indicates that a stack with nearly quiescent ambient air is 10 °C hotter than that with 1 m/s airspeed. This is of particular importance in systems that are exposed to the outer environment. Along the same lines, the time it takes for the stack to cool depends on the load of the cooling circuit in the separators. In general, the cooling demand of the simulated stack accounted for up to 20% of its total power.

Performing experiments on the stack enabled the identification of discrepancies between the theoretical and real behavior that emanate from the design and the current losses. The comparison of the temperature measurements and the model at high currents yielded a maximum error of 3.1% and signified that the current losses are close to zero. On the contrary, the same comparison for low currents underlined the existence of the bypass losses that enlarge the heat generation. In the previous chapter, a mathematical approach to calculating the faradaic efficiency is elucidated. This is formulated on the thermal behavior of the stack by considering it as a simple electrical circuit and its calibration is done on an insulated stack. The integration of the faradaic efficiency to the thermal balance computations extended the accuracy of the model even at low currents. This is supported by the fact that the maximum deviation between the experiment and the simulation in the low current region did not exceed 5%. The assessment of the system's total efficiency at 30 °C showed that the maximum value is 60% at 170 mA/cm² current density. Before and after that, it drops due to the current and ohmic losses, respectively.

A final remark would be the importance of the model calibration. Parameters like the electrode activity, membrane resistance, and heat transfer coefficient are usually unknown and for that reason must be adjusted to the experimental results. Therefore, experiments are essential for the creation of a trustworthy simulation that can predict the electrolyser's performance under most circumstances.

5.2 Recommendations

The thorough investigation of hydrogen production through water electrolysis gave awareness of the weaknesses not only of the system itself but also of the modeling approach. The knowledge gained so far can be culminated in the following recommendations.

The presence of bubbles in the cell was expressed according to mass balance and empirical equations. Nonetheless, the flow of electrolyte in the tested cell is not uniformly distributed and the surface properties of the electrode differ from that of the literature. Therefore, areas of high and low bubble velocity are created leading to different bubble volume fractions and electrode coverage. A two-phase flow simulation of the cell would provide a more accurate representation of the bubble distribution enabling the estimation of the voltage drop and the bubble-electrolyte velocity in a naturally driven flow. It has been shown that the electrochemical activity of the electrode and the membrane resistivity significantly affect cell efficiency. Dedicated experiments for both parts would avoid their fitting and simultaneously allow the comparison with other materials available in the market.

The benefit of operating at high temperatures implies that the stack should start up with a large current to heat the system. In addition, minimizing ambient losses or even insulating the system will allow the extraction of useful heat energy through a cooling medium. According to the performance of the real stack, mid-range current densities are preferred for long-term operation since low current levels are distinguished by the presence of bypass losses. A consequent step is the elimination of the bypass current by increasing the electrolyte path in the channels that could permit the operation of the stack in lower currents and higher efficiency. Regarding the experimental process, more experiments should be performed for the insulated stack under a greater range of current densities attaining a better calibration of the faradaic efficiency.

A | Stack

A.1 Stack mass & energy balance

The investigation of the thermal behavior of the stack necessitates the implementation of the 1st law of thermodynamics for reaction systems. A rather rigorous derivation of Eq. 3.39 will be presented in the following paragraph.

Firstly, it is important to start with the electrolyte molar balance of the cell. Hence,

$$\frac{dn_{\text{ele}}}{dt} = \dot{n}_{\text{ele,in}} - \dot{n}_{\text{ele,out}} - \dot{n}_{\text{v}} - \dot{n}_{\text{cons}}$$

Where, n_{ele} , $\dot{n}_{\text{ele,in}}$, $\dot{n}_{\text{ele,out}}$, \dot{n}_{v} , and \dot{n}_{cons} are the moles of the water in the stack, the molar flow of water getting into the stack, water going out of the stack, the water turned into vapor, and water consumed during the reaction.

The amount of water produced/consumed in the system is not significant to create unsteady conditions inside the stack. The small current densities to be applied, render it reasonable to assume steady state conditions. Consequently,

$$\dot{n}_{\rm ele,out} = \dot{n}_{\rm ele,in} - \dot{n}_{\rm v} - \dot{n}_{\rm cons} \tag{A.1}$$

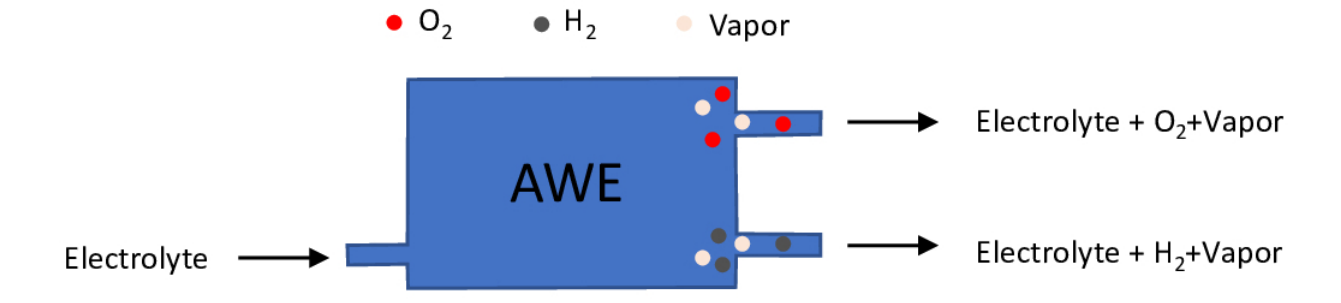


Figure A.1: Illustration of the flows entering and exiting the stack. At the inlet, the pure electrolyte is inserted while the electrolyte with hydrogen, oxygen, and vapor leaves the stack. The amount of water consumed in the reaction zone is relative insignificant enabling the use of a steady state molar balance.

The energy balance for an open system with reaction, is formulated as follows.

$$\begin{split} C_{\mathrm{m}} \frac{dT_{\mathrm{cell}}}{dt} &= \dot{n}_{\mathrm{ele,in}} \cdot \overline{h}_{\mathrm{ele,in}} - \dot{n}_{\mathrm{ele,out}} \cdot \overline{h}_{\mathrm{ele,out}} - \dot{n}_{\mathrm{O}_{2}} \cdot \overline{h}_{\mathrm{O}_{2}} - \dot{n}_{\mathrm{H}_{2}} \cdot \overline{h}_{\mathrm{H}_{2}} - \dot{n}_{\mathrm{v}} \cdot \overline{h}_{\mathrm{v}} \\ + U_{\mathrm{c}} \cdot I - \dot{Q}_{\mathrm{amb}} & \stackrel{\text{Eq. A.1}}{\Longleftrightarrow} C_{\mathrm{m}} \frac{dT_{\mathrm{cell}}}{dt} = \dot{n}_{\mathrm{ele,in}} \cdot \overline{h}_{\mathrm{ele,in}} - (\dot{n}_{\mathrm{ele,in}} - \dot{n}_{\mathrm{v}} - \dot{n}_{\mathrm{cons}}) \cdot \overline{h}_{\mathrm{ele,out}} \\ - \dot{n}_{\mathrm{O}_{2}} \cdot \overline{h}_{\mathrm{O}_{2}} - \dot{n}_{\mathrm{H}_{2}} \cdot \overline{h}_{\mathrm{H}_{2}} - \dot{n}_{\mathrm{v}} \cdot \overline{h}_{\mathrm{v}} + U_{\mathrm{c}} \cdot I - \dot{Q}_{\mathrm{amb}} \end{split}$$

Where $\overline{h}_{\rm ele,in}$, $\overline{h}_{\rm ele,out}$, $\overline{h}_{\rm O_2}$, $\overline{h}_{\rm H_2}$, and $\overline{h}_{\rm v}$ are the specific molar enthalpies of the electrolyte at the inlet, electrolyte at the outlet, oxygen, hydrogen, and water vapor, respectively. The overall heat capacity of the cell is denoted as $C_{\rm m}$. The temperature of the cell is indicated by $T_{\rm cell}$

In addition,

$$U_{\rm c}I = U_{\rm c}I + U_{\rm tn}I - U_{\rm tn}I = I(U_{\rm c} - U_{\rm tn}) + I\frac{\Delta H_{\rm rxn}}{2F}$$

Where $\Delta H_{\rm rxn}$ is the enthalpy of reaction at temperature T. Hence, the term $U_{\rm tn}$ can be replaced according to Eq. 2.8.

Moreover,

$$\dot{n}_{\rm H_2} = 2\dot{n}_{\rm O_2} = \dot{n}_{\rm cons} = \frac{I}{2F}$$
(A.2)

Therefore,

$$\begin{split} C_{\rm m} \frac{dT_{\rm cell}}{dt} &= \dot{n}_{\rm ele,in} \cdot (\overline{h}_{\rm ele,in} - \overline{h}_{\rm ele,out}) + \dot{n}_{\rm cons} \cdot \overline{h}_{\rm ele,out} + \dot{n}_{\rm v} \cdot \overline{h}_{\rm ele,out} - \\ &\dot{n}_{\rm cons} \cdot \overline{h}_{\rm H_2} - \frac{1}{2} \dot{n}_{\rm cons} \cdot \overline{h}_{\rm O_2} - \dot{n}_{\rm v} \cdot \overline{h}_{\rm v} + I(U_{\rm c} - U_{\rm tn}) + \frac{I}{2F} \Delta H_{\rm rxn} \\ &- \dot{Q}_{\rm amb} \Leftrightarrow C_{\rm m} \frac{dT_{\rm cell}}{dt} = \dot{n}_{\rm ele,in} \cdot (\overline{h}_{\rm ele,in} - \overline{h}_{\rm ele,out}) + \dot{n}_{\rm cons} \cdot (\overline{h}_{\rm ele,out} \\ &- \overline{h}_{\rm H_2} - \frac{1}{2} \overline{h}_{\rm O_2}) + I(U_{\rm c} - U_{\rm tn}) + \frac{I}{2F} \Delta H_{\rm rxn} - \dot{Q}_{\rm amb} + \dot{n}_{\rm v} \cdot (\overline{h}_{\rm ele,out} - \overline{h}_{\rm v}) \end{split}$$

But,

$$-\Delta H_{\rm rxn} = \overline{h}_{\rm ele,out} - \overline{h}_{\rm H_2} - \frac{1}{2}\overline{h}_{\rm O_2} \tag{A.3}$$

and

$$\overline{h}_{lg} = \overline{h}_{v} - \overline{h}_{ele,out} \tag{A.4}$$

Where \bar{h}_{lg} is the specific molar enthalpy of water's phase change at the electrolyte's outlet temperature. So, based on Eq. A.2, A.3, and A.4 the energy balance is formulated in the following way.

$$C_{\rm m} \frac{dT_{\rm cell}}{dt} = \dot{n}_{\rm ele,in} \cdot (\overline{h}_{\rm ele,in} - \overline{h}_{\rm ele,out}) + I(U_{\rm c} - U_{\rm tn}) + \frac{I}{2F} \Delta H_{\rm rxn}$$

$$-\frac{I}{2F} \Delta H_{\rm rxn} - \dot{Q}_{\rm amb} + \dot{n}_{\rm v} \cdot (\overline{h}_{\rm ele,out} - \overline{h}_{\rm v}) \Leftrightarrow C_{\rm m} \frac{dT_{\rm cell}}{dt} = \dot{n}_{\rm ele,in} \cdot$$

$$(\overline{h}_{\rm ele,in} - \overline{h}_{\rm ele,out}) + I(U_{\rm c} - U_{\rm tn}) - \dot{Q}_{\rm amb} - \dot{n}_{\rm v} \cdot \overline{h}_{\rm lg}$$

Or,

$$C_{\rm m} \frac{dT_{\rm cell}}{dt} = \dot{n}_{\rm ele,in} \cdot c_{\rm p,ele} \cdot (T_{\rm in} - T_{\rm cell}) + I(U_{\rm c} - U_{\rm tn}) - \dot{n}_{\rm v} \cdot \overline{h}_{\rm lg} - \dot{Q}_{\rm amb}$$

By expressing the molar flows, heat capacity, and specific enthalpy with the corresponding mass ones, taking into account the number of cells in the stack, and considering the change of thermoneutral voltage with temperature, the final equation gets the following form:

$$C_{\rm t} \frac{dT_{\rm stack}}{dt} = \dot{m}_{\rm ele,in} \cdot c_{\rm p,ele} \cdot (T_{\rm in} - T_{\rm stack}) + N_{\rm cell} \cdot I(U_{\rm c} - U_{\rm t,P}^{\rm tn}) - N_{\rm cell} \cdot \dot{m}_{\rm v} \cdot h_{\rm lg} - \dot{Q}_{\rm amb}$$
(A.5)

Where C_t is the overall heat capacity of the stack.

A.2 Stack entropy balance

An equally significant aspect of the analysis is the thermodynamic approach of the stack dictated by the second law. For that reason, this paragraph is dedicated to the derivation of the entropy balance implemented in the main model.

Considering the same control volume as that of the energy balance, the second law analysis in steady-state conditions is formulated as follows:

$$0 = \dot{n}_{\rm ele,in} \cdot s_{\rm ele,in} - \dot{n}_{\rm ele,out} \cdot s_{\rm ele,out} - \dot{n}_{\rm O_2} \cdot s_{\rm O_2} - \dot{n}_{\rm H_2} \cdot s_{\rm H_2} - \dot{n}_{\rm v} \cdot s_{\rm v}$$

$$+ \dot{S}_{\rm gen} - \frac{\dot{Q}_{\rm amb}}{T_{\rm cell}} \stackrel{\rm Eq. A.1}{\Longleftrightarrow} 0 = \dot{n}_{\rm ele,in} \cdot s_{\rm ele,in} - (\dot{n}_{\rm ele,in} - \dot{n}_{\rm v} - \dot{n}_{\rm cons}) \cdot s_{\rm ele,out}$$

$$- \dot{n}_{\rm O_2} \cdot s_{\rm O_2} - \dot{n}_{\rm H_2} \cdot s_{\rm H_2} - \dot{n}_{\rm v} \cdot s_{\rm v} + \dot{S}_{\rm gen} - \frac{\dot{Q}_{\rm amb}}{T_{\rm cell}} \stackrel{\rm Eq. A.2}{\Longleftrightarrow} 0 = \dot{n}_{\rm ele,in} \cdot (s_{\rm ele,in} - s_{\rm ele,out}) + \dot{n}_{\rm v} \cdot (s_{\rm ele,out} - s_{\rm v}) + \dot{n}_{\rm cons} \cdot (s_{\rm ele,out} - s_{\rm H_2} - \frac{1}{2} s_{\rm O_2})$$

$$+ \dot{S}_{\rm gen} - \frac{\dot{Q}_{\rm amb}}{T_{\rm cell}}$$

Where $s_{\text{ele,in}}$, $s_{\text{ele,out}}$, s_{H_2} , s_{O_2} , and s_{v} are the specific molar entropies of the electrolyte at the inlet, electrolyte at the outlet, oxygen, hydrogen, and water vapor, respectively.

On the other hand, $\dot{S}_{\rm gen}$ expresses the generated entropy due to the irreversibility of the process and $T_{\rm cell}$ is the temperature at the boundary of the system and its environment which is equal to the temperature of the cell due to the lumped thermal capacitance model.

$$s_{\rm lg} = s_{\rm v} - s_{\rm ele,out} \tag{A.6}$$

Where s_{lg} is the specific molar entropy of water's phase change.

Moreover,

$$\Delta S_{\text{rxn}} = s_{\text{H}_2} + \frac{1}{2} s_{\text{O}_2} - s_{\text{ele,out}}$$
 (A.7)

Based on Eq. A.6 and A.7, the entropy balance is expressed as follows:

$$0 = \dot{n}_{\rm ele,in} \cdot (s_{\rm ele,in} - s_{\rm ele,out}) - \dot{n}_{\rm v} \cdot s_{\rm lg} + \dot{n}_{\rm cons} \cdot (-\Delta S_{\rm rxn}) + \dot{S}_{\rm gen} - \frac{\dot{Q}_{\rm amb}}{T_{\rm cell}}$$

According to the thermodynamics of water electrolysis (Eq. 2.6, Eq. 2.7, and 2.8) it can be derived that

$$\Delta S = \frac{\Delta H - \Delta G}{T_{\text{cell}}} \Leftrightarrow \Delta S = \frac{2F \cdot (U_{\text{tn}} - U_{\text{rev}})}{T_{\text{cell}}}$$
(A.8)

Hence, substituting Eq. A.8 and A.2, the entropy balance is modified in the following way:

$$0 = \dot{n}_{\rm ele,in} \cdot (s_{\rm ele,in} - s_{\rm ele,out}) - \dot{n}_{\rm v} \cdot s_{\rm lg} + I \cdot \frac{U_{\rm rev} - U_{\rm tn}}{T_{\rm cell}} + \dot{S}_{\rm gen} - \frac{\dot{Q}_{\rm amb}}{T_{\rm cell}}$$

Alternatively, the expression of the entropy balance in mass basis instead of molar, the consideration of all cells in the stack, and taking into account the temperature variation of the reversible and thermoneutral voltage leads to the below mentioned expression.

$$0 = \dot{m}_{\text{ele,in}} \cdot (s_{\text{ele,in}} - s_{\text{ele,out}}) - N_{\text{cell}} \cdot \dot{m}_{\text{v}} \cdot s_{\text{lg}} + N_{\text{cell}} \cdot I \cdot \frac{U_{\text{T,P}}^{\text{rev}} - U_{\text{t,P}}^{\text{tn}}}{T_{\text{stack}}} + \dot{S}_{\text{gen}} - \frac{\dot{Q}_{\text{amb}}}{T_{\text{stack}}}$$
(A.9)

A.3 Separator mass & energy balance

The modeling of the separators is an important aspect of the total system's response. The same approach is followed as the one applied in the stack.

Firstly, the mass balance of each phase inside the separator must be set up by identifying the flow streams that enter and exit the control volume. The small amount of electrolyte converted into the gaseous product as well as its replenishment with feed demi

water rationalizes the assumption of negligible mass change in the separators. In addition, the amount of vapor that condenses inside the separator is neglected. A dynamic model is necessary for the thermal behavior considering the fact that the heat generated in the stack acts on the separator's internal energy.

At the inlet, both electrolyte and gas products are inserted as a mixture while they exit from the outlet as two separate phases. Conversely, the demineralized feed water serves to replenish the consumed water and maintain the concentration of the electrolyte. Hence, the mass balance for the liquid and gas phase is formulated as shown below.

$$\dot{m}_{\rm mix}(g) = \dot{m}_{\rm gas} + \dot{m}_{\rm v} \tag{A.10}$$

$$\dot{m}_{\rm mix}(l) + \dot{m}_{\rm f} = \dot{m}_{\rm out} \tag{A.11}$$

Where $\dot{m}_{\rm mix}(g)$ and $\dot{m}_{\rm mix}(l)$ are the mass flow rates of the gaseous and liquid phase entering the control volume as a mixture. The terms $\dot{m}_{\rm gas}$ and $\dot{m}_{\rm v}$ denote the mass flow rates of H₂ or O₂ and vapor leaving the separator while $\dot{m}_{\rm f}$ is the mass flow of the demineralized water. Moreover, the electrolyte leaving the separator is expressed as $\dot{m}_{\rm out}$

The gaseous products that enter the separator are firstly produced in the stack, consequently, $\dot{m}_{\rm mix}(g)$ is calculated using the Eq. 3.35, 3.36, 3.38. In addition, the water converted into H₂, O₂, and vapor has to be replenished with demi water, thus

$$\dot{m}_{\rm mix}(g) = \dot{m}_{\rm f}$$

Considering the thermal balance of the separator, the 1st law of thermodynamics indicates that:

$$C_{\rm t,sep} \frac{dT_{\rm sep}}{dt} = \dot{m}_{\rm mix}(g) \cdot h_{\rm gas,in} + \dot{m}_{\rm mix}(l) \cdot h_{\rm ele,in} + \dot{m}_{\rm f} \cdot h_{\rm f} - \dot{m}_{\rm gas} \cdot h_{\rm gas,out} - \dot{m}_{\rm out} \cdot h_{\rm ele,out} - \dot{m}_{\rm v} \cdot h_{\rm gas,out} - \dot{Q}_{\rm amb}$$

Where $h_{\rm gas,in}$ and $h_{\rm gas,out}$ is the specific enthalpy of gas products entering and leaving the separator, respectively. In addition, $h_{\rm ele,in}$, $h_{\rm ele,out}$, and $h_{\rm f}$ is the specific enthalpy of the electrolyte entering, leaving, and the feed water entering the system. The temperature of the separator is indicated by $T_{\rm sep}$ and the overall heat capacity of the separator is denoted as $C_{\rm t,sep}$.

By considering the mass balance (Eq. A.11 and A.10) and executing the necessary simplifications, the thermal balance is expressed as follows:

$$C_{\text{t,sep}} \frac{dT_{\text{sep}}}{dt} = \dot{m}_{\text{mix}}(g) \cdot c_{\text{p,gas}} \cdot (T_{\text{in}} - T_{\text{sep}}) + \dot{m}_{\text{mix}}(l) \cdot c_{\text{p,ele}} \cdot (T_{\text{in}} - T_{\text{sep}})$$

$$+ \dot{m}_{\text{f}} \cdot c_{\text{p,water}} \cdot (T_{\text{f}} - T_{\text{sep}}) - \dot{Q}_{\text{amb}}$$
(A.12)

Where $c_{p,gas}$, $c_{p,ele}$, and $c_{p,water}$ is the constant-pressure specific thermal capacity of H_2 or O_2 with vapor, electrolyte, and demi water, respectively. Furthermore, T_{in} is

the inlet temperature of the electrolyte and gas entering the separator, while T_{sep} is the temperature of streams at the outlet as well as that of the control volume. Lastly, T_{f} is the inlet temperature of the feed water and \dot{Q}_{amb} denotes the heat losses to the environment.

A.4 Solvers

The thermal and electrochemical modeling of the stack necessitates the implementation of appropriate solvers that provide the solution to differential equations and the minimization of objective functions. In the following section, all the necessary information and working principles regarding the solvers used are provided

The polarization curve of the cell with Stainless-steel and Nickel electrodes is accomplished after building the algorithm explained in chapter 3 and fitting the free parameters based on the experimental data. It is desired that the modeled polarization curve has a minimum difference compared to the experimental data for every current density and temperature. With that being said,

Minimize Error =
$$\sum_{t=30}^{50} \sum_{I=2}^{12} |U(I,t) - U_{\exp}(I,t)|$$
 (A.13)

The algorithms used for the minimization of the objective function above are the Nelder-Mead and the Differential Evolution. The Nelder-Mead algorithm is a direct search method (no gradient is required) usually applied to non-linear optimization problems. Furthermore, it is a heuristic method that may converge to non-stationary points [75]. The Differential Evolution is a metaheuristic method that does not use the gradient of the objective function but attempts different candidate solutions for the minimization of the problem. Moreover, it is frequently used in multidimensional problems that are not continuous, are noisy, and change with time [76].

Regarding the thermal modeling of the setup, a system of ordinary differential equations (Eq. A.5, A.12) describing the stack's and separators' temperature with time has to be solved simultaneously. For that reason, the Python solver odeint is implemented. The odeint command is based on the algorithm LSODA that includes several explicit (i.e., Euler method, Adams-Bashforth) and implicit methods (i.e., implicit Runge-Kutta, Rosenbrock). The algorithm automatically selects between stiff and non-stiff methods, and it has the advantage of starting with non-stiff ones and after monitoring data, it decides which method to apply [77, 78].

Bibliography

- [1] The European Commission. Causes of climate change.
- [2] Qingchen Chao. Scientific basis of climate change and its response. Global Energy Interconnection, 1:8, 2018.
- [3] Samer Fawzy, Ahmed I. Osman, John Doran, and David W. Rooney. Strategies for mitigation of climate change: a review. *Environmental Chemistry Letters*, 18:2069–2094, November 2020.
- [4] Xuan Phuong Nguyen, Anh Tuan Hoang, Aykut I. Ölçer, and Thanh Tung Huynh. Record decline in global CO₂ emissions prompted by COVID-19 pandemic and its implications on future climate change policies. *Energy Sources, Part A: Recovery, Utilization, and Environmental Effects*, pages 1–4, January 2021.
- [5] CO₂ emissions dataset: Our sources and methods. Available at: https://ourworldindata.org/co2-dataset-sources. Accessed: 2 March 2022.
- [6] UNFCCC. The Paris Agreement, December 2015.
- [7] Joris Proost. Critical assessment of the production scale required for fossil parity of green electrolytic hydrogen. *International Journal of Hydrogen Energy*, 45:17067–17075, July 2020.
- [8] Martín David, Carlos Ocampo-Martínez, and Ricardo Sánchez-Peña. Advances in alkaline water electrolyzers: A review. *Journal of Energy Storage*, 23:392–403, June 2019.
- [9] John Andrews and Bahman Shabani. Where does Hydrogen Fit in a Sustainable Energy Economy? *Procedia Engineering*, 49:15–25, 2012.
- [10] E. Bianco and H. Blanco. Green hydrogen: A guide to policy making. International Renewable Energy Agency. Technical report, November 2020.
- [11] J. Gigler and R. Graafland, C. H. Blokdijk. NL dutch solutions for a hydrogen economy. Netherlands Enterprise Agency. April 2021.
- [12] Sonja van Renssen. The hydrogen solution? Nature Climate Change, 10:799–801, September 2020.

- [13] Christopher J. Quarton, Olfa Tlili, Lara Welder, Christine Mansilla, Herib Blanco, Heidi Heinrichs, Jonathan Leaver, Nouri J. Samsatli, Paul Lucchese, Martin Robinius, and Sheila Samsatli. The curious case of the conflicting roles of hydrogen in global energy scenarios. Sustainable Energy & Fuels, 4:80–95, 2020.
- [14] Emma Han, Olivia Woodward and Charles Forbes. Enabling the European hydrogen economy. Aurora Energy Research. Report, May 2021.
- [15] Ministerie van Economische Zaken en Klimaat. Government Strategy on Hydrogen Publication Government.nl, April 2020. Last Modified: 2020-04-06T11:45 Publisher: Ministerie van Algemene Zaken.
- [16] Tom Smolinka, Henry Bergmann, Juergen Garche, and Mihails Kusnezoff. The history of water electrolysis from its beginnings to the present. In *Electrochemical Power Sources: Fundamentals, Systems, and Applications*, pages 83–164. Elsevier, 2022.
- [17] PosHYdon Webpage | About PosHYdon.
- [18] Peter De Laat. Overview of hydrogen projects in the Netherlands. Topsector Energie. May 2021.
- [19] XINTC Global Webpage.
- [20] Yujing Guo, Gendi Li, Junbo Zhou, and Yong Liu. Comparison between hydrogen production by alkaline water electrolysis and hydrogen production by PEM electrolysis. *IOP Conference Series: Earth and Environmental Science*, 371:042022, December 2019.
- [21] Philipp Haug. Experimental and theoretical investigation of gas purity in alkaline water electrolysis. PhD thesis, Universitätsbibliothek der TU Clausthal, March 2019.
- [22] Nicolas Guillet and Pierre Millet. Alkaline Water Electrolysis. In Agata Godula-Jopek, editor, *Hydrogen Production*, pages 117–166. Wiley-VCH Verlag GmbH & Co. KGaA, Weinheim, Germany, February 2015.
- [23] Jesús Rodríguez and Ernesto Amores. CFD Modeling and Experimental Validation of an Alkaline Water Electrolysis Cell for Hydrogen Production. *Processes*, 8:1634, December 2020.
- [24] O. Ulleberg. Modeling of advanced alkaline electrolyzers: a system simulation approach. *International Journal of Hydrogen Energy*, 28:21–33, January 2003.
- [25] M. Ni, M. Leung, and D. Leung. Technological development of hydrogen production by solid oxide electrolyzer cell (SOEC). *International Journal of Hydrogen Energy*, 33:2337–2354, May 2008.

- [26] Frano Barbir. *PEM fuel cells: theory and practice*. Elsevier/Academic Press, Amsterdam; Boston, 2nd ed edition, 2013.
- [27] Department of Interface Chemistry and Surface Engineering, Max-Planck-Institut für Eisenforschung GmbH, Max-Planck-Strasse 1, 40237 Düsseldorf, Germany and Maximilian Schalenbach. A Perspective on Low-Temperature Water Electrolysis Challenges in Alkaline and Acidic Technology. *International Journal of Electrochemical Science*, pages 1173–1226, February 2018.
- [28] Maximilian Schalenbach, Geert Tjarks, Marcelo Carmo, Wiebke Lueke, Martin Mueller, and Detlef Stolten. Acidic or Alkaline? Towards a New Perspective on the Efficiency of Water Electrolysis. *Journal of The Electrochemical Society*, 163:F3197–F3208, 2016.
- [29] Christian Henao, Kodjo Agbossou, Mhamed Hammoudi, Yves Dubé, and Alben Cardenas. Simulation tool based on a physics model and an electrical analogy for an alkaline electrolyser. *Journal of Power Sources*, 250:58–67, March 2014.
- [30] M. Hammoudi, C. Henao, K. Agbossou, Y. Dubé, and M.L. Doumbia. New multiphysics approach for modelling and design of alkaline electrolyzers. *International Journal of Hydrogen Energy*, 37:13895–13913, October 2012.
- [31] Rodney L. LeRoy, Christopher T. Bowen, and Donald J. LeRoy. The Thermodynamics of Aqueous Water Electrolysis. *Journal of The Electrochemical Society*, 127:1954–1962, September 1980.
- [32] Kazuo Onda, Takahiro Kyakuno, Kikuo Hattori, and Kohei Ito. Prediction of production power for high-pressure hydrogen by high-pressure water electrolysis. *Journal of Power Sources*, 132:64–70, May 2004.
- [33] Keith J. Laidler and M. Christine King. The Development of Transition-State Theory. *Journal of Physical Chemistry*, pages 2657–2664, January 1983.
- [34] Marcelo Carmo and Detlef Stolten. Energy Storage Using Hydrogen Produced From Excess Renewable Electricity. In *Science and Engineering of Hydrogen-Based Energy Technologies*, pages 165–199. Elsevier, 2019.
- [35] Pierre Olivier, Cyril Bourasseau, and Pr. Belkacem Bouamama. Low-temperature electrolysis system modelling: A review. *Renewable and Sustainable Energy Reviews*, 78:280–300, October 2017.
- [36] Xiaoyan Hu, Xuemei Tian, Ying-Wu Lin, and Zhonghua Wang. Nickel foam and stainless steel mesh as electrocatalysts for hydrogen evolution reaction, oxygen evolution reaction and overall water splitting in alkaline media. RSC Advances, 9:31563– 31571, 2019.

- [37] N. Nagai. Existence of optimum space between electrodes on hydrogen production by water electrolysis. *International Journal of Hydrogen Energy*, 28:35–41, January 2003.
- [38] R. Gilliam, J. Graydon, D. Kirk, and S. Thorpe. A review of specific conductivities of potassium hydroxide solutions for various concentrations and temperatures. *International Journal of Hydrogen Energy*, 32:359–364, March 2007.
- [39] Matheus T. de Groot and Albertus W. Vreman. Ohmic resistance in zero gap alkaline electrolysis with a Zirfon diaphragm. *Electrochimica Acta*, 369:137684, February 2021.
- [40] R.W. Powell, R.P. Tye, and M.J. Hickman. The thermal conductivity of nickel. *International Journal of Heat and Mass Transfer*, 8:679–688, May 1965.
- [41] Helmut Vogt, Gerhard Kreysa, Subramanyan Vasudevan, Rolf Wüthrich, Jana D. Abou Ziki, and Raïssa El-Haddad. Electrochemical Reactors. In Wiley-VCH Verlag GmbH & Co. KGaA, editor, *Ullmann's Encyclopedia of Industrial Chemistry*, pages 1–49. Wiley-VCH Verlag GmbH & Co. KGaA, Weinheim, Germany, January 2014.
- [42] L.J.J. Janssen, C.W.M.P. Sillen, E. Barendrecht, and S.J.D. van Stralen. Bubble behaviour during oxygen and hydrogen evolution at transparent electrodes in KOH solution. *Electrochimica Acta*, 29:633–642, May 1984.
- [43] J. Eigeldinger and H. Vogt. The bubble coverage of gas-evolving electrodes in a flowing electrolyte. *Electrochimica Acta*, 45:4449–4456, September 2000.
- [44] H. Vogt and R.J. Balzer. The bubble coverage of gas-evolving electrodes in stagnant electrolytes. *Electrochimica Acta*, 50:2073–2079, March 2005.
- [45] W. Hug, J. Divisek, J. Mergel, W. Seeger, and H. Steeb. Highly efficient advanced alkaline electrolyzer for solar operation. *International Journal of Hydrogen Energy*, 17:699–705, September 1992.
- [46] C.A Schug. Operational characteristics of high-pressure, high-efficiency water-hydrogen-electrolysis. *International Journal of Hydrogen Energy*, 23:1113–1120, December 1998.
- [47] Georgios Sakas, Alejandro Ibáñez-Rioja, Vesa Ruuskanen, Antti Kosonen, Jero Ahola, and Olli Bergmann. Dynamic energy and mass balance model for an industrial alkaline water electrolyzer plant process. *International Journal of Hydrogen Energy*, 47:4328–4345, January 2022.
- [48] Z. Abdin, C.J. Webb, and E.MacA. Gray. Modelling and simulation of an alkaline electrolyser cell. *Energy*, 138:316–331, November 2017.

- [49] Dohyung Jang, Hyun-Seok Cho, and Sanggyu Kang. Numerical modeling and analysis of the effect of pressure on the performance of an alkaline water electrolysis system. *Applied Energy*, 287:116554, April 2021.
- [50] Ravichandra S. Jupudi, Guillermo Zappi, and Richard Bourgeois. Prediction of shunt currents in a bipolar electrolyzer stack by difference calculus. *Journal of Applied Electrochemistry*, 37:921–931, August 2007.
- [51] A. Khalilnejad and G.H. Riahy. A hybrid wind-PV system performance investigation for the purpose of maximum hydrogen production and storage using advanced alkaline electrolyzer. *Energy Conversion and Management*, 80:398–406, April 2014.
- [52] Ernesto Amores, Jesús Rodríguez, and Christian Carreras. Influence of operation parameters in the modeling of alkaline water electrolyzers for hydrogen production. *International Journal of Hydrogen Energy*, 39:13063–13078, August 2014.
- [53] W. Hug, H. Bussmann, and A. Brinner. Intermittent operation and operation modeling of an alkaline electrolyzer. *International Journal of Hydrogen Energy*, 18:973–977, December 1993.
- [54] Jaroslaw Milewski, Giulio Guandalini, and Stefano Campanari. Modeling an alkaline electrolysis cell through reduced-order and loss-estimate approaches. *Journal of Power Sources*, 269:203–211, December 2014.
- [55] P. Dieguez, A. Ursua, P. Sanchis, C. Sopena, E. Guelbenzu, and L. Gandia. Thermal performance of a commercial alkaline water electrolyzer: Experimental study and mathematical modeling. *International Journal of Hydrogen Energy*, 33:7338–7354, December 2008.
- [56] Tohid Adibi, Atta Sojoudi, and Suvash C. Saha. Modeling of thermal performance of a commercial alkaline electrolyzer supplied with various electrical currents. *International Journal of Thermofluids*, 13:100126, February 2022.
- [57] Damien Le Bideau, Philippe Mandin, Mohamed Benbouzid, Myeongsub Kim, and Mathieu Sellier. Review of necessary thermophysical properties and their sensivities with temperature and electrolyte mass fractions for alkaline water electrolysis multiphysics modelling. *International Journal of Hydrogen Energy*, 44:4553–4569, February 2019.
- [58] Asif S. Ansar, Aldo S. Gago, Fatemeh Razmjooei, Regine Reißner, Ziqi Xu, and Kaspar Andreas Friedrich. Alkaline electrolysis—status and prospects. In *Electrochemical Power Sources: Fundamentals, Systems, and Applications*, pages 165–198. Elsevier, 2022.
- [59] Ph. Vermeiren, R. Leysen, H. Beckers, J. P. Moreels, and A. Claes. The influence of manufacturing parameters on the properties of macroporous Zirfon separators. *Journal of Porous Materials*, 15:259–264, June 2008.

- [60] Alfredo Maciel-Cerda, editor. Membranes. Springer International Publishing, 2017.
- [61] L.J.J. Janssen, J.J.M. Geraets, E. Barendrecht, and S.D.J.van Stralen. Ohmic potential drop during alkaline water electrolysis. *Electrochimica Acta*, 27:1207–1218, September 1982.
- [62] Kazushige Ishida and Derek Lister. *In situ* measurement of corrosion of type 316L stainless steel in 553 K pure water via the electrical resistance of a thin wire. *Journal of Nuclear Science and Technology*, 49:1078–1091, November 2012.
- [63] M. Kibria. Electrochemical studies of the nickel electrode for the oxygen evolution reaction. *International Journal of Hydrogen Energy*, 21:179–182, Mar 1996.
- [64] M. F. Kibria, M. Sh. Mridha, and A. H. Khan. Electrochemical studies of a Nickel electrode for the hydrogen evolution reaction. *International Journal of Hydrogen Energy*, 20:435–440, June 1994.
- [65] H. Wendt and V. Plzak. Electrocatalytic and thermal activation of anodic oxygenand cathodic hydrogen-evolution in alkaline water electrolysis. *Electrochimica Acta*, 28:27–34, January 1983.
- [66] T. S. Lee. Hydrogen Over potential on Pure Metals in Alkaline Solution. *Journal of The Electrochemical Society*, 118:1278, 1971.
- [67] R. N. O'Brien and P. Seto. The Mechanism of Hydrogen Evolution at a Stainless Steel Electrode in Basic Solution. *Journal of The Electrochemical Society*, 117:32, 1970.
- [68] Frank P. Incropera and David P. DeWitt. Fundamentals of heat and mass transfer. Wiley, New York, 1996. OCLC: 33403372.
- [69] Michael J. Moran, Howard N. Shapiro, Daisie D. Boettner, and Margaret B. Bailey. Fundamentals of engineering thermodynamics. John Wiley & Sons, 2010.
- [70] Anthony F. Mills and C.F.M Coimbra. *Basic heat and mass transfer*. Temporal Publishing, San Diego, CA, 2015. OCLC: 1146401340.
- [71] Ch. Comninellis, E. Plattner, and P. Bolomey. Estimation of current bypass in a bipolar electrode stack from current-potential curves. *Journal of Applied Electrochemistry*, 21:415–418, May 1991.
- [72] G. Bonvin and Ch. Comninellis. Scale-up of bipolar electrode stack dimensionless numbers for current bypass estimation. *Journal of Applied Electrochemistry*, 24:469–474, June 1994.
- [73] Alfredo Ursúa and Pablo Sanchis. Static-dynamic modelling of the electrical behaviour of a commercial advanced alkaline water electrolyser. *International Journal of Hydrogen Energy*, 37:18598–18614, December 2012.

- [74] Burin Yodwong, Damien Guilbert, Matheepot Phattanasak, Wattana Kaewmanee, Melika Hinaje, and Gianpaolo Vitale. Faraday's Efficiency Modeling of a Proton Exchange Membrane Electrolyzer Based on Experimental Data. *Energies*, 13:4792, September 2020.
- [75] Nelder-Mead method. Available at: https://en.wikipedia.org/w/index.php?title=Nelder%E2%80%93Mead_method&oldid=1081571332. Accessed: 8 July 2022.
- [76] Differential evolution. Available at: https://en.wikipedia.org/w/index.php?title=Differential_evolution&oldid=1094959469. Accessed: 8 July 2022.
- [77] Alan Hindmarsh. ODEPACK Ordinary Differential Equation Solvers, February 2008.
- [78] Mario Mulansky and Karsten Ahnert. Odeint library. *Scholarpedia*, 9:32342, December 2014.